Physik - Department

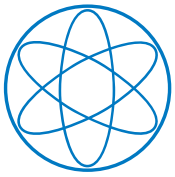

Characterisation of the Muon-Induced Neutron Background with a LiF Cryogenic Detector

Dissertation
von

Alexander Klaus Herbert
Langenkämper

Technische Universität
München

Technische Universität München tum
School of Natural Sciences

Characterisation of the Muon-Induced Neutron Background with a LiF Cryogenic Detector

Alexander Klaus Herbert Langenkämper

Vollständiger Abdruck der von der TUM School of Natural Sciences der Technischen Universität München zur Erlangung eines

Doktors der Naturwissenschaften (Dr. rer. nat.)

genehmigten Dissertation.

Vorsitz:	Prof. Dr. Alejandro Ibarra
Prüfer*innen der Dissertation:	
	1. Prof. Dr. Stefan Schönert
	2. Priv.-Doz. Dr. Bela Majorovits

Die Dissertation wurde am 05.06.2023 bei der Technischen Universität München eingereicht und durch die TUM School of Natural Sciences am 11.09.2023 angenommen.

Abstract

The existence of dark matter (DM) is perhaps the most puzzling and unsolved mystery in modern astroparticle physics. Evidence for its existence has been found on various lengths and time scales. The CRESST (Cryogenic Rare Event Search with Superconducting Thermometers) experiment aims to directly detect DM particles by their elastic scattering from nuclei in $CaWO_4$ single crystals. A particle interaction in the crystal leads to the generation of phonons and scintillation light. The CRESST-III experiment is currently the leading experiment for DM masses below $1.5\,\mathrm{GeV/c^2}$. Neutrons are the ultimate and fundamental background for the CRESST experiment and other low-threshold experiments worldwide since elastic neutron scattering (epithermal to fast neutrons) can mimic a DM signal. In particular, only passive neutron shielding can be used, and active discrimination is impossible.

In this work, a cryogenic neutron monitoring system for measuring the neutron flux within the experimental volume of rare event search experiments was designed, built, and characterized. The detection principle is based on neutron capture at ^{6}Li ($^6\mathrm{Li} + n \rightarrow \alpha + {}^3\mathrm{H} + 4.78\,\mathrm{MeV}$) in a 100 g cylindrical lithium fluoride (LiF) single crystal. To distinguish neutron events from background events, e.g., electron/gamma events, the LiF scintillation light is read out by a special silicon light detector.

For testing the LiF module, a cryogenic characterization facility was set up with a ^{3}He-^{4}He dilution cryostat with a base temperature of 10 mK at the shallow underground laboratory in Garching (UGL). Three new SQUID readout systems were added to the system. In addition, the readout electronics were optimized, and an efficient active muon veto was added to the system.

A four-month measurement campaign was carried out in the cryogenic setup using the realized neutron monitor detector made of LiF. The result shows that it is possible to measure a neutron energy spectrum using the neutron capture events. Two contributions to the neutron flux were found in the UGL facility: the neutrons from the environment and the muon-induced neutrons in the cryogenic facility. With the muon veto, it was possible to distinguish between the two origins, and the muon-induced neutrons could be used as a perfect benchmark scenario for the neutron monitor. The analysis yielded a measured muon-induced neutron rate of 7.54 ± 0.15 n/h. For the first time, an initial neutron energy spectrum in the cryogenic UGL facility was calculated via the energy-dependent capture cross-section.

The initial neutron flux was derived from the measured captured neutron events to obtain a more accurate value and reduce the systematic error. A special simulation was developed to study the neutron reaction in lithium fluoride. Two unfolding methods are presented, the first via matrix

inversion and the second by fitting the simulation to the data. This is the first time that a cryogenically measured spectrum has been deconvolved. The two methods presented allow the determination of the original neutron flux of the neutron signal measured in LiF up to 500 keV. Up to this energy, a total neutron flux of $(17.1^{+7.8}_{-14.1})\,\mathrm{cm}^{-1}\mathrm{h}^{-1}(20\,\mathrm{keV})^{-1}$ (method 1), and $(4.2 \pm 0.8)\,\mathrm{cm}^{-1}\mathrm{h}^{-1}(20\,\mathrm{keV})^{-1}$ (method 2) could be found. It was also possible to perform neutron spectroscopy with a resolution of 20 keV. In the lowest energy range from 0 keV to 20 keV, neutron fluxes of $(10.1^{+4.6}_{-9.8})\,\mathrm{cm}^{-1}\mathrm{h}^{-1}(20\,\mathrm{keV})^{-1}$ and $(7.0 \pm 0.3) \cdot 10^{-1}\,\mathrm{cm}^{-1}\mathrm{h}^{-1}(20\,\mathrm{keV})^{-1}$ for method 1 and method 2 were calculated. Method 1 considers both statistical and systematic errors, with systematic error dominating at the lowest energy bins. Method 2 only accounts for statistical error but may have a similar systematic error range as method 1. The measurement campaign at UGL leads to the first comprehensive study of the neutron background spectrum in a cryogenic setup.

The detector principle developed in this work will be a powerful tool for characterizing the neutron background in-situ in cryogenic direct DM experiments (such as CRESST) and other experiments searching for rare events affected by the neutron background, such as the coherent neutrino nuclear scattering (CEνNS) experiment NUCLEUS. Understanding and monitoring the neutron background can significantly impact rare event search experiments to improve sensitivity.

Zusammenfassung

Die Existenz der Dunklen Materie (DM) ist vielleicht das rätselhafteste und immer noch ungelöste Rätsel der modernen Astroteilchenphysik. Beweise für ihre Existenz wurden auf verschiedenen Längen- und Zeitskalen gefunden. Das CRESST-Experiment (Cryogenic Rare Event Search with Superconducting Thermometers) zielt auf den direkten Nachweis von DM-Teilchen durch deren elastische Streuung an Kernen in $CaWO_4$-Einkristallen ab. Eine Teilchenwechselwirkung im Kristall führt zur Erzeugung von Phononen und Szintillationslicht. Das CRESST-III-Experiment ist derzeit das führende Experiment für DM-Massen unter $1.5\,\mathrm{GeV/c^2}$. Neutronen sind der ultimative und irreduzible Hintergrund für das CRESST-Experiment und andere niedrigschwellige Experimente weltweit, da elastische Neutronenstreuung (epithermische bis schnelle Neutronen) ein DM-Signal imitieren kann. Insbesondere kann nur eine passive Neutronenabschirmung verwendet werden, und eine aktive Unterscheidung ist nicht möglich.

Im Rahmen dieser Arbeit wurde ein kryogenes Neutronenmonitoring-System zur Messung des Neutronenflusses innerhalb des Experimentiervolumens von Experimenten zur Suche seltener Ereignisse entwickelt, gebaut und charakterisiert. Das Detektionsprinzip basiert auf dem Neutroneneinfang an ^{6}Li ($^6\mathrm{Li} + n \rightarrow \alpha + {}^3\mathrm{H} + 4.78\,\mathrm{MeV}$) in einem 100 g zylindrischen Lithium-Fluorid (LiF) Einkristall. Um Neutronenereignisse von Hintergrundereignissen, z. B. Elektronen/Gamma-Ereignissen, zu unterscheiden, wird das LiF-Szintillationslicht von einem speziellen Silizium-Lichtdetektor ausgelesen.

Für den Test des LiF-Moduls wurde eine kryogene Charakterisierungsanlage mit einem ^{3}He-^{4}He-Entmischungskryostaten mit einer Basistemperatur von 10 mK im oberflächennahen Untergrundlabor in Garching (UGL) eingerichtet. Das System wurde um drei neue SQUID-Auslesesysteme erweitert. Darüber hinaus wurde die Ausleseelektronik optimiert und das System um ein effizientes aktives Myonen-Veto ergänzt.

In dem kryogenen Aufbau wurde eine viermonatige Messkampagne mit dem realisierten Neutronenmonitor-Detektor aus LiF durchgeführt. Das Ergebnis zeigt, dass es möglich ist, ein Neutronenenergiespektrum unter Verwendung der Neutroneneinfangereignisse zu messen. Zwei Beiträge zum Neutronenfluss wurden in der UGL-Anlage gefunden: die Neutronen aus der Umgebung und die Myonen-induzierten Neutronen in der kryogenen Anlage selbst. Mit dem Myonen-Veto war es möglich, zwischen beiden Ursprüngen zu unterscheiden, und die Myonen-induzierten Neutronen konnten als perfektes Benchmark-Szenario für den Neutronenmonitor verwendet werden. Die durchgeführte Analyse ergab eine gemessene muon-induzierte Neutronenrate

von $7.54 \pm 0.15\,\mathrm{n/h}$, und zum ersten Mal wurde ein anfängliches Neutronenenergiespektrum in der kryogenen UGL-Anlage über den energieabhängigen Einfangquerschnitt berechnet.
Um einen genaueren Wert zu erhalten und den systematischen Fehler zu verringern, wurde der anfängliche Neutronenfluss aus den gemessenen eingefangenen Neutronen abgeleitet. Eine spezielle Simulation wurde entwickelt und zur Untersuchung der Neutronenreaktion in Lithiumfluorid verwendet. Es werden zwei Entfaltungsmethoden vorgestellt, die erste über eine Matrixinversion und die zweite durch fitten der Simulation an die Daten. Dies ist das erste Mal, dass ein kryogen gemessenes Spektrum entfaltet wurde.
Die beiden vorgestellten Methoden ermöglichen die Bestimmung des ursprünglichen Neutronenflusses des im LiF gemessenen Neutronensignals bis zu 500 keV. Bis zu dieser Energie konnte ein Gesamtneutronenfluss für Methode 1 von $(17.1^{+7.8}_{-14.1})\,\mathrm{cm^{-1}h^{-1}(20\,keV)^{-1}}$, sowie für Methode 2 von $(4.2 \pm 0.8)\,\mathrm{cm^{-1}h^{-1}(20\,keV)^{-1}}$ gefunden werden. Außerdem war es möglich, Neutronenspektroskopie mit einer Auflösung von 20 keV durchzuführen. Im untersten Energiebin $((0-20)\,\mathrm{keV})$ wurden Neutronenflüsse von $(10.1^{+4.6}_{-9.8})\,\mathrm{cm^{-1}h^{-1}(20\,keV)^{-1}}$ und $(7.0 \pm 0.3) \cdot 10^{-1}\,\mathrm{cm^{-1}h^{-1}(20\,keV)^{-1}}$ für Methode 1 beziehungsweise Methode 2 berechnet. Methode 1 berücksichtigt sowohl statistische als auch systematische Fehler, wobei systematische Fehler in den untersten Energiebins dominieren. Methode 2 berücksichtigt nur statistische Fehler, kann aber einen ähnlichen systematischen Fehlerbereich haben wie Methode 1. Die Messkampagne in der UGL führt zur ersten umfassenden Untersuchung des Neutronenhintergrundspektrums in einem kryogenen Aufbau.
Das in dieser Arbeit entwickelte Detektorprinzip wird ein leistungsfähiges Werkzeug zur In-situ-Charakterisierung des Neutronenhintergrunds in kryogenen direkten DM-Experimenten (wie CRESST) und anderen Experimenten zur Suche nach seltenen Ereignissen sein, die durch den Neutronenhintergrund beeinflusst werden, sowie das kohärente Neutrino-Kernstreuung (CEνNS) Experiment NUCLEUS. Das Verständnis und die überwachung des Neutronenhintergrunds können einen großen Einfluss auf Experimente zur Suche nach seltenen Ereignissen haben, um die Empfindlichkeit zu verbessern.

"Persistence is the most powerful force on earth, it can move mountains."

— Albert Einstein

Contents

Chapter 1

Dark Matter - An Unsolved Enigma

For decades the enigma of the nature of Dark Matter has occupied generations of scientists and is still one of the most puzzling questions in modern astroparticle physics. Already in the 19th century, physicists were discussing the unseen matter observed in the universe. Their hypotheses were dark stars, planets, and clouds or dark "nebulae". The kick-off was the observation of persistent anomalies in the motion of Uranus, ending in the discovery of a new planet, Neptun [1][2][3][4][5][6][7]. One of the most famous representatives of the early Dark Matter community is Fritz Zwicky. He suggested the existence of nonluminous matter in the 1930s when he examined the velocities of galaxies in the Coma Cluster, applying the virial theorem for the first time to a cluster to calculate its mass. He concluded that an additional, non-visible amount of matter has to be present to explain the observed velocity distribution. He called this matter "Dark Matter" [8]. During the last 90 years, various new indications for the existence of Dark Matter were found on all cosmological scales. For a more detailed overview of the history of Dark Matter, the reader is referred to [9].
This chapter presents a few indications for the existence of Dark Matter, possible candidates, and possible methods and techniques of its detection. Afterward, the direct Dark Matter search experiment CRESST and its results are explained in more detail. In the end, backgrounds for Dark Matter search experiments are discussed.

1.1 Indications for Dark Matter

Rotation Curves of Spiral Galaxies

Measurements of rotation curves of spiral galaxies yield one of the hints for Dark Matter on galactic scales. Considering Newtonian dynamics on

the rotation system, any stable rotating body around the center must be in equilibrium between the gravitational force and the centrifugal force:

$$\frac{mv_{rot}^2}{r} = \frac{GM(r)m}{r^2} \tag{1.1}$$

Where m is the mass of the observed star, v its velocity, $G = 6.6738(8) \cdot 10^{-11}\ \frac{\mathrm{m}^3}{\mathrm{kg}}$ [10] the gravitational constant and $M(r)$ the galactic mass contained within the radius r. For large distances r, the whole luminescent matter is contained in the bulge, and $M(r) = M = \text{constant}$.

$$v = \sqrt{\frac{MG}{r}} \propto \frac{1}{\sqrt{r}} \tag{1.2}$$

Thus the velocity of objects in the spiral arms should decrease with $\frac{1}{\sqrt{r}}$ at large distances. However, measurements of the 21 cm line of neutral hydrogen clouds have shown a more constant or even an increasing velocity which is shown in figure 1.1. This phenomenon can be explained by an additional Dark Matter halo surrounding the galaxy [11][12][13][14].

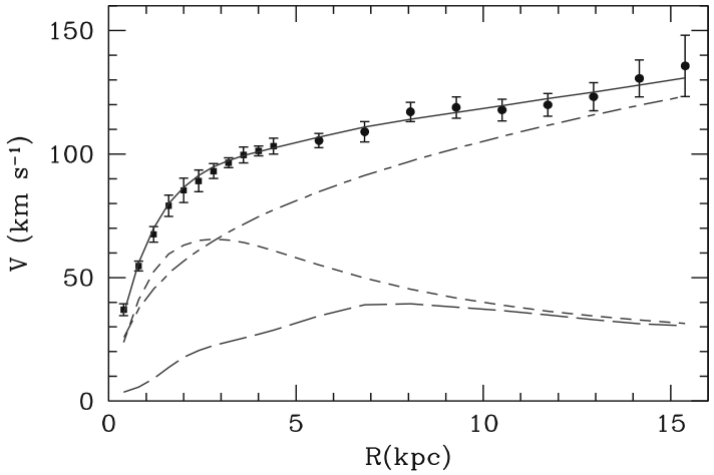

Figure 1.1: M33 rotation curve (points) compared with the best-fit model (continuous line). Also shown is the halo contribution (dashed-dotted line) needed to explain the observations, the stellar disk (short dashed line), and the gas contribution (long dashed line)[11].

Velocities of Galaxies in Galaxy Clusters

The velocity distribution of galaxies and galaxy clusters is another hint of the existence of Dark Matter in the Universe. Fritz Zwicky calculated the

mass of the Coma Cluster system using the virial theorem that relates the average kinetic energy $\bar{\epsilon}_k$ and the average potential energy $\bar{\epsilon}_p$:

$$\bar{\epsilon}_k = -\frac{1}{2}\bar{\epsilon}_p \tag{1.3}$$

Using this formula, he determined the mass from measurements of the velocities of galaxies in the system. He calculated that the amount of matter has to be $\sim$ 400 times the present luminous matter. [8]
Even though measurements of the X-ray spectra of those galaxy clusters have shown the existence of gas clouds that can be $\sim$10 times their luminous mass, they cannot account for the amount of missing mass. Therefore, most of the matter has to be dark.

Bullet Cluster

The Bullet Cluster is one of the strongest hints of Dark Matter. It consists of two galaxy clusters that collide with each other. Figure 1.2 shows both clusters after the collision. The green contour represents the mass distribution of the system, determined via gravitational lensing. The right side represents the X-ray image showing the interaction of gas, which is the clusters' main amount of visible mass. The color coding from blue (cold) to yellow (hot) shows the interaction of the gas between the clusters. The gas is mainly situated in the center, whereas the main amount of mass, determined by gravitational lensing, passes each other without any interaction.
As mentioned, the Bullet Cluster is a strong hint of the existence of Dark Matter. Alternative explanations without Dark Matter, like the theory of Modified Newtonian Dynamics (MOND), in which the main statement is that Newton's laws work very well on smaller scales, like our solar system, but have to be modified on galactic scales, cannot explain those observations [15][16].

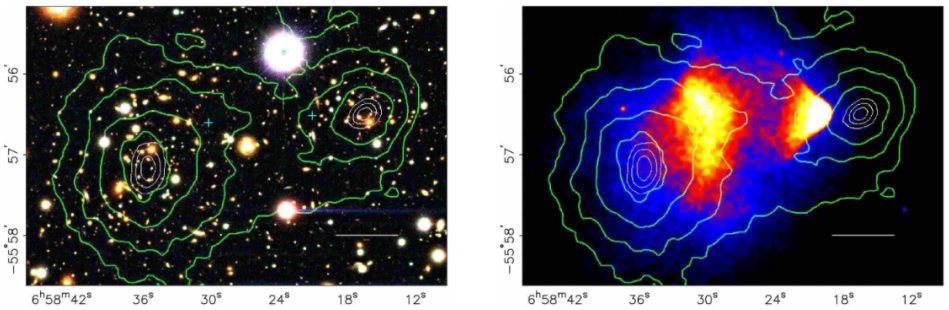

Figure 1.2: The Bullet Cluster. The green contour corresponds to the gravitational potential, which was determined using gravitational lensing. Left: Image of 1E0657 - 558. Right: X-ray image which shows the location of the luminous matter [17].

Cosmic Microwave Background

The fourth indication for Dark Matter is features measured in the Cosmic Microwave Background (CMB). At the very beginning, our Universe was hot and opaque to electromagnetic radiation due to the scattering of the photons by free electrons. About 370000 years after the Big Bang, when the Universe had a temperature near 3000 K, it was cool enough for protons to capture free electrons and recombine them into hydrogen. Radiation and matter decoupled, and the Univers became transparent to light. The CMB is, therefore, the relic of the last scattering process and follows a nearly perfect black body spectrum with today's temperature of $2.7255 \pm 0.0006\,\mathrm{K}$ [18][19].

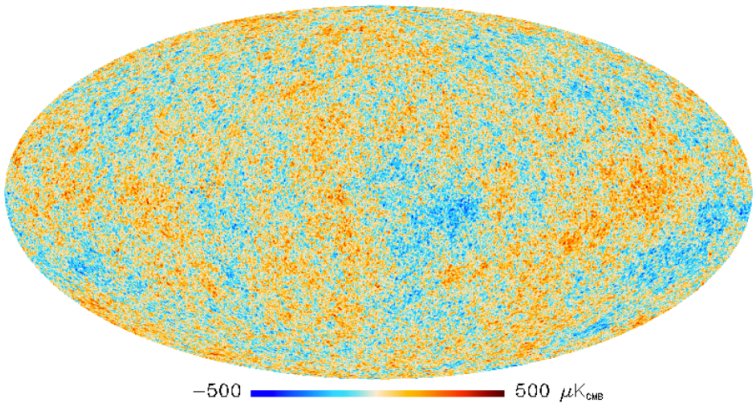

Figure 1.3: Mapping of the CMB temperature fluctuations measured by the PLANCK satellite. The anisotropies are in the order of tens of μK [19].

The measured CMB has little temperature fluctuations or anisotropies. In figure 1.3, a mapping of the CMB anisotropies measured by the PLANCK satellite is shown [19]. The differences in temperature are in the order of tens of μK.
These anisotropies at any point in the sky (θ, ϕ) can be translated in the basis of spherical harmonics.

$$\frac{\Delta T}{T}(\theta, \phi) = \sum_{lm} a_{lm} Y_{lm}(\theta, \phi) \tag{1.4}$$

with a_{lm} coefficients [18] and assume rotational symmetry and Gaussianity with

$$\langle a^{\star}_{lm} a l' m' \rangle = C_l \delta_{l'l} \delta_{m'm} \tag{1.5}$$

leading to a power spectrum seen in figure 1.4. The horizontal axis is logarithmic up to $l = 50$ and then linear. The vertical axis scales with $l(l+1)C_l/2\pi$

[19]. The acoustic peaks deliver information about our Universe's Baryonic Matter, Dark Matter, and Dark Energy content. The first peak determines the curvature of the Universe Ω. In contrast, the second and third peaks determine the reduced baryonic density Ω_b, respectively, giving information about the Dark Matter density. Under the assumption of the correctness of the λCDM model, the Planck collaboration determined a baryonic matter density of $\Omega_b h^2 = 0.02237 \pm 0.00015$ and a Dark Matter density of $\Omega_C h^2 = 0.1200 \pm 0.0012$ [20].

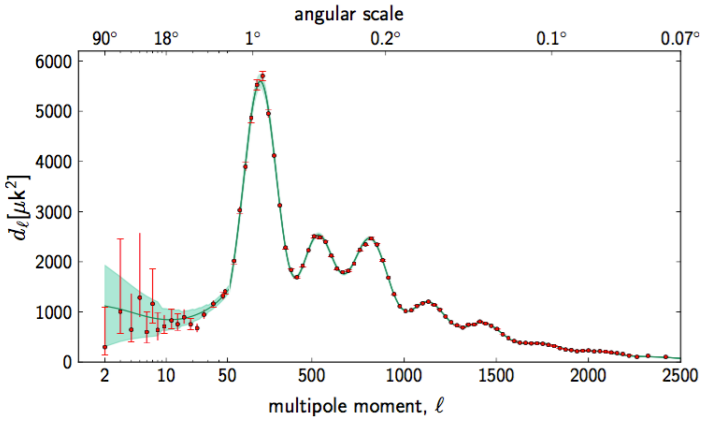

Figure 1.4: Temperature angular power spectrum of the primary CMB from PLANCK, showing a precise measurement of seven acoustic peaks that are well-fitted by a six-parameter λCDM model in the Planck Collaboration XVI 2014. The horizontal axis is logarithmic up to l = 50 and linear beyond. The vertical scale is $l(l+1)C_l/2\pi$ [19].

1.2 Dark Matter Candidates

In the previous section, a list of important hints (and there are many more) for the existence of Dark Matter was presented. It was shown that a large fraction of the matter in the Universe is not related to baryonic matter. Since the nature of Dark Matter is still unknown, the question about its origin and components still need to be answered. Therefore, a detailed study of the properties of Dark Matter and the development of detection techniques is a key point in astroparticle physics. In the following, a not complete list of possible Dark Matter candidates is given.
Over the last decades, manifold candidates for Dark Matter have been suggested, from known Standard Models of particle physics particles to particles from extended models. Dark Matter particles have to fulfill a list of properties. They have to be created in the early universe to be stable or have a long lifetime since the effect of Dark Matter can be seen in the CMB as well as in nowadays structures. Dark Matter can also not be electrically charged be-

cause of the absence of electromagnetic interaction. It has to be mainly "cold" and, therefore, non-relativistic to explain the observed structure formation. And last, Dark Matter has to be non-baryonic because of the observations of the acoustic oscillations of the CMB. A review on Dark Matter candidates can be found in [21] and [22]. In the following, some Dark Matter candidates are described in more detail.

Neutrinos

The neutrino is a Standard Model particle that can be considered Dark Matter. It is not interacting electromagnetically on a weak scale and is, therefore, an excellent natural Dark Matter candidate. Due to the relativistic properties and the very low masses of neutrinos, they can only explain the "hot" Dark Matter universe, which contradicts the observed structure formation. In addition, the upper limit of the neutrino mass is given by $m_\nu < 0.8\,\mathrm{eV/c^2}$ [23] and the limits on the total neutrino relic density lead to the conclusion that the neutrino is not abundant enough to explain the whole Dark Matter content of the Universe [24].

Axions

The axion is a favored and well-established Dark Matter candidate with a mass of $\mathcal{O}(\mu\mathrm{eV/c^2})$. The axion was postulated to resolve the strong CP problem in Quantum Chromodynamics (QCD). According to the Lagrangian of QCD, a violation of the charge-parity-symmetry (CP-symmetry) is possible. However, no experiment involving only the strong interaction observed the CP violation. An explanation can be found by introducing the Peccei-Quinn symmetry and introducing a new particle, the axion. This particle is possibly accessible via its coupling to photons. This effect is called the Primakoff effect [25][26][27].

WIMPs

The WIMP (Weakly Interacting Massive Particle) is a very commonly considered Dark Matter particle candidate predicted by extensions of the Standard Model. The mass range of this particle last from $\sim 10\,\mathrm{GeV/c^2}$ to $1\,\mathrm{TeV/c^2}$. A WIMP has to interact weakly and gravitationally and be electrically neutral. In the early Universe, WIMPs were in thermal equilibrium, which means that their production and annihilation process was in equilibrium. Due to the expansion of the Universe and, therefore, a cooling, a "freeze-out" occurred, leading to a stable relic density of WIMPs. Nevertheless, WIMPs have not been found experimentally yet. For more information about the WIMP as a Dark Matter candidate, see reference [21].

Asymmetric Dark Matter

Light Dark Matter scenarios have become more important in the last years. The Lee-Weinberg bound excludes WIMPs lighter than ~ 2 GeV/c^2 [28] since the relic density would over-close the Universe. Asymmetric Dark Matter is one of several well-motivated alternatives for the WIMP scenario below these masses of ~ 2 GeV/c^2 [29]. The central hypothesis of Asymmetric Dark Matter is that Dark Matter has a matter-anti-matter asymmetry like baryonic matter. Refer to [29, 30] for more information about this theoretical approach.

1.3 Dark Matter Detection

For the detection of Dark Matter particles, three different approaches can be considered. The first is the production of Dark Matter with colliders. Second is the annihilation of Dark Matter particles into Standard Model particles, called indirect detection. And last, direct detection aims to detect the scattering of Dark Matter particles on Standard Model particles. Figure 1.5 shows the different detection channels.

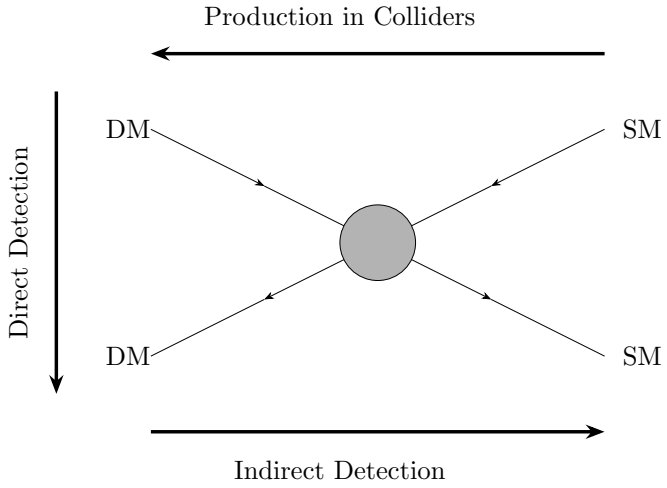

Figure 1.5: Schematic Feynman diagram for the Dark Matter detection channels. Dark Matter (DM) can be produced in colliders via Standard Model particles (SM). The annihilation of DM to SM is called indirect detection. The scattering of DM on SM is called direct detection.

Search with Colliders

In colliders, it is theoretically possible to produce Dark Matter via the annihilation of Standard Model particles. The energy carried away by the created Dark Matter can not be detected. The Dark Matter escapes the experiment. The missing energy and momentum put into the production process of Dark Matter particles can be evaluated. Two experiments searching for this process are ATLAS (A Toroidal LHC Apparatus) [31] and CMS (Compact-Muon-Solenoid) [32] at the LHC at CERN. The LHC is a 26.7 km long ring which accelerates protons. Those protons collide with a center-of-mass energy of 13 TeV. The multilayer detectors ATLAS and CMS aim to detect the produced collision particles to reconstruct the missing energy and, therefore, a potential Dark Matter signal.

Indirect Detection

Indirect searches aim to detect decay- or annihilation products of Dark Matter particles [33]. Typical products are electron-positron pairs, proton-antiproton pairs, gamma rays, and neutrinos. The PAMELA (Payload for Antimatter Matter Exploration and Light-nuclei Astrophysics) satellite [34] is searching for the antiparticle component, which is positrons and antiprotons. The FGST (Fermi Gamma-ray Space Telescope) [35] space telescope is looking for gamma rays.

Direct Detection

The third method is the direct detection of Dark Matter. This detection channel aims to detect a nuclear recoil induced by elastic Dark Matter-nucleon scattering of Dark Matter from the halo in our galaxy with earth-bound detectors. Therefore, Dark Matter particles have to interact not only gravitationally but also via the weak force. A possible signal then depends on the cross-section of the process, the Dark Matter density, and the target size.
One of the biggest challenges for experiments aiming for the direct detection of Dark Matter is a very low expected signal rate of less than 0.1 events/kg/day. Due to this low signal rate, natural radioactivity in the detector components and cosmic radiation (primarily muons) can significantly contribute to the background. Therefore, such experiments are typically located in underground laboratories to ensure a very low muon flux and complete shielding from other cosmic radiation. Furthermore, shielding made of, e.g., copper, lead, and PE (Polyethylene) is used to reduce the ambient background radiation (γ, neutrons, and β).
Depending on the target material, the energy transferred by the nuclear recoil can be detected via three different channels:

- Ionization
- Scintillation
- Heat/Phonons

For experiments interested in nuclear recoils, electron recoils are a significant background when searching for light DM (sub-GeV mass range). Therefore, sufficient background discrimination is mandatory to achieve high sensitivity. One possibility to discriminate background from the signal is to take advantage of two instead of one detection channel. The energy deposition in each channel depends on the kind of interacting particle and allows suppression of the electron/gamma background. In the following, a few examples are given:

1. Phonon-Ionization: Common detector materials for phonon and ionization experiments are semiconductors (e.g., germanium or silicon). The EDELWEISS (Expérience per détecter les WIMPs en site souterrain) [36] in France. The experiments SCDMS (Super Cryogenic Dark Matter Search) [37], CDMSLite (Cryogenic Dark Matter Search Low Ionization Threshold Experiment) [38][39][40] and SuperCDMS Snolab [41] are measuring heat signals induced by nuclear recoils. Simultaneous measurement of the ionization signal by drifting the charges allows these experiments to discriminate electron recoils and surface background from nuclear recoils (signal).

2. Scintillation-Ionization: Typical experiments with scintillation and ionization read-out are liquid noble gas experiments like LUX (Large Underground Xenon experiment) [42], XENON [43][44] and PandaX (Particle and Astrophysical Xenon Detector) [45] using dual-phase time projection chambers. An interaction in the detector leads to a primary scintillation signal detected by photomultipliers and simultaneously a charge which is drifted along an electric field to the interface between liquid and gaseous phase producing secondary scintillation light. Both signals allow a position reconstruction to define a fiducial volume. In combination and the drift time, the two light signals allow particle discrimination. Liquid noble gas experiments can easily scale up their experiment to very high detector masses compared to any other direct dark matter detection technique.

3. Phonon-Scintillation The most common detector materials for experiments using the phonon and scintillation channels are $CaWO_4$, Al_2O_3, NaI, CsI, Li_2MoO_4, and BGO. This combination of detection channels is also called the phonon-light technique and will be described in more detail in section 1.4. Representatives of these detection channels are, e.g., ROSEBUD (Rare Objects SEarch with Bolometers UndergrounD) [46], COSINUS (Cryogenic Observatory for SIgnals seen in Next-generation Underground Searches)

[47] and CRESST (Cryogenic Rare Event Search with Superconducting Thermometer) [48][49].

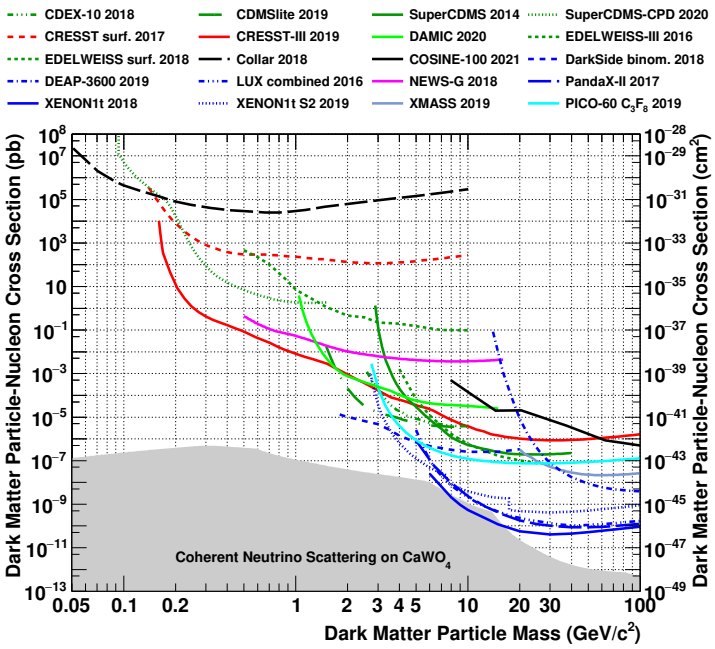

Figure 1.6: Results from different Dark Matter experiments on elastic, spin-independent Dark Matter nucleus scattering. Shown is the cross-section versus Dark Matter particle mass. The result of CRESST-III [48] is depicted in solid red with the most stringent limit between masses of $(0.16 - 1.8)\,\mathrm{GeV/c2}$. The red dotted line corresponds to a surface measurement performed with a gram-scale Al_2O_3 detector [50]. Limits from CDEX [51], CDMSlite [40], DAMIC [52], EDELWEISS [53][54], SuperCDMS [37][55], DEAP-3600 [56], CoGeNT [57], DarkSide [58], LUX [59], Panda-X [60], Xenon1t [61][62], COSINE-100 [63], Collar [64], NEWS-G [65], XMASS [66], and PICO (C_3F_8) [67] are shown. The grey region marks the so-called neutrino floor for $CaWO_4$ [68]. The figure is taken from [69].

Figure 1.6 presents the current landscape of the Dark Matter parameter space (Dark Matter particle-nucleon cross-section σ versus the Dark Matter particle mass m). The dotted and solid lines are the exclusion limits of several direct Dark Matter search experiments. All combinations of σ and m above these lines are excluded (90 % C.L.) by the respective experiments. For Dark Matter masses larger $6\,\mathrm{GeV/c^2}$ XENON1t [44][61][62] has the best limit so far. In the light Dark Matter region, CRESST [48] (below $1.8\,\mathrm{GeV/c^2}$) achieves the best limit. The grey area represents the coherent neutrino-nucleus scattering on $CaWO_4$ [68], dominantly from solar neutrinos.
As described above, the phonon light technique is a possible detection tech-

nique for the direct search for Dark Matter. The basic idea is explained in the following section.

1.4 Scintillating Calorimeters - Phonon Light Technique

Cryogenic calorimeters measure a particle-induced temperature (phonons) increase in an absorber crystal operated at mK temperatures. They consist of an absorber crystal and a thermometer which is thermally coupled to the absorber crystal. After a particle interaction and, therefore, energy deposition

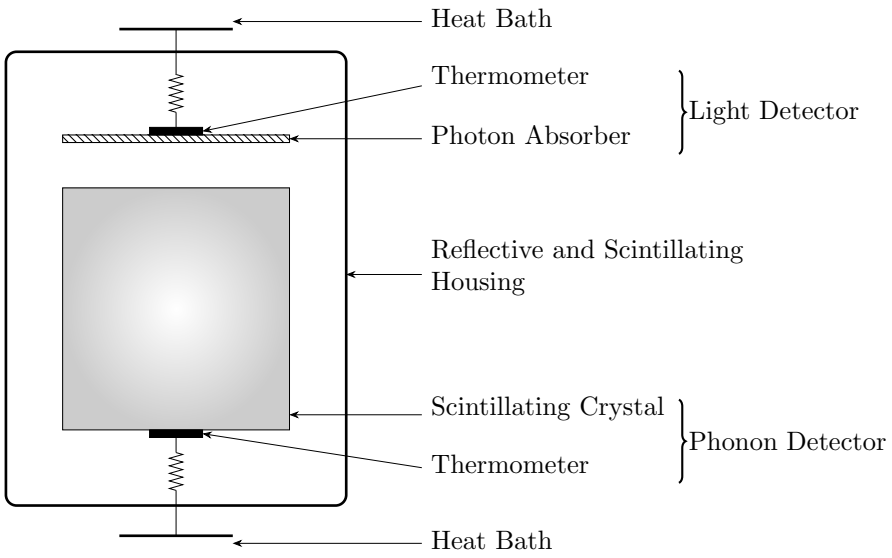

Figure 1.7: Schematic drawing of a cryogenic calorimeter module using the phonon-light technique. The module consists of a phonon and a light detector. The phonon detector is made out of a target crystal connected to a thermometer, whereas the light detector consists of a light absorber semiconductor connected to a second thermometer. Both detectors are operated simultaneously to distinguish different kinds of interacting particles by the creation of additional light in the absorber crystal due to particle interaction. They are mounted in a reflecting and scintillating housing made of highly reflecting polymeric foil to achieve a high light collection efficiency. The additional scintillation ability of the foils is used for discrimination of, e.g., surface α-events.

in the absorber, thermal equilibrium with the heat bath is reestablished via a

weak thermal link between the crystal and heat bath. With a single channel system, particle discrimination is impossible just by the pulse measured.
The phonon light technique is a helpful tool for active background suppression in any cryogenic rare event search experiments and detailed background studies. This technique is based on the simultaneous measurement of a heat signal in a target crystal (as described above) and a light signal due to luminescence light (e.g., scintillation light or Cherenkov light) from the crystal with a separate cryogenic light detector. Figure 1.7 shows a schematic drawing of a detector module using the phonon light technique. The module consists of two separate detectors, a phonon and a light detector. The phonon detector is a scintillating target crystal equipped with a thermometer that is directly connected to the crystal. The cryogenic light detector consists of a semiconductor photon absorber (silicon, silicon-on-sapphire, or germanium) which is thermally coupled to a second thermometer to measure the temperature increase induced by the light absorption. Both thermometers are coupled to the copper housing, which acts as a heat bath. Light and phonon detectors are mounted in a reflecting and scintillating housing made of a highly reflecting polymeric foil to achieve a significant light collection efficiency. The additional scintillation ability of the foils is used for discrimination of, e.g., surface α-events. Hence, the foil is essential to maximize the light collection and to discriminate background from a potential Dark Matter signal.
As mentioned in the previous section, an example of a direct Dark Matter search experiment is the CRESST (Cryogenic Rare Event Search with Superconducting Thermometers) experiment described in more detail in the following section.

1.5 The CRESST-III Experiment

The CRESST experiment [48][70][71] is located in the underground laboratory "Laboratori Nazionali del Gran Sasso" (LNGS) [72] in Italy. CRESST aims at the detection of elastic scattering of Dark Matter particles off target nuclei in scintillating $CaWO_4$ single crystals, which are operated as cryogenic detectors at mK temperatures.
In this section, the module design, as well as the experimental setup, are described.

1.5.1 Experimental Setup

The expected signal rates for direct Dark Matter search experiments are in the order of 0.1 events/kg/day. Therefore, highly efficient background suppression is necessary to identify and discriminate signal events from background events.
To shield the experiment from cosmic radiation CRESST is located 1400 m

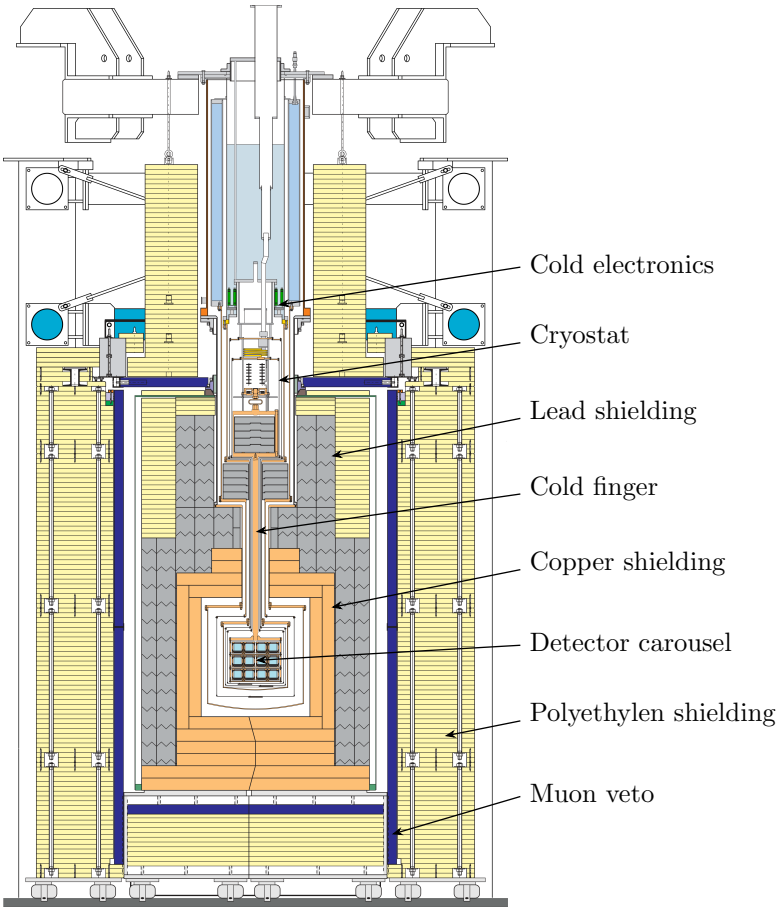

Figure 1.8: Schematic drawing of the CRESST setup with shielding and cryostat. The detector carousel housing the detector modules is linked via the cold finger to the cryostat. Several shields of copper, lead, and polyethylene surround the experiment. The copper and lead shielding are enclosed in a radon-free box. The muon veto is used to identify events induced by cosmic radiation. The figure is taken from [70].

beneath the Gran Sasso massif which is equivalent to 3500 m - 3800 m water [71][73]. This reduces the flux of cosmogenic muons by a factor of 10^6 to $\sim 1\,\mathrm{muon/m^2/h}$ [74][75][76]. LNGS operates three halls in the laboratory. CRESST is located in hall A. The CRESST setup is enclosed in a Faraday cage to shield the experiment from electromagnetic interference [77], which can potentially mimic signals or increase the noise in the electronic system and, therefore, decrease the sensitivity.
The experimental setup is located inside the Faraday cage, which is schematically shown in figure 1.8. The detector modules are mounted in a copper carousel and are thermally coupled to the mixing chamber of a ^{3}He/^{4}He dilution refrigerator via a cold finger. The cryostat is run with a base temperature of less than 10 mK. For more information about the working principle of a ^{3}He/^{4}He dilution cryostat, see chapter 2.4. The CRESST experiment is equipped with 66 read-out channels [70].
To lower the ambient background, different layers of shielding surround the experiment. The detector carousel is encased with several layers of lead and copper to shield against gamma radiation. In addition, two layers of polyethylene are used to moderate neutrons, mainly produced by muons interacting with the surrounding material. The innermost shielding of copper and lead is enclosed in a gas-tight radon-free box. The outermost layer consists of plastic scintillator muon veto panels to identify the remaining muons passing through the setup [70][78].

1.5.2 Detector Modules

The core of the experiment is the detector module. CRESST detectors are taking advantage of the phonon-light technique, as described in section 1.4. A schematic drawing of the detector design is shown in figure 1.9, and a photograph of an opened CRESST-III detector module can be seen in figure 1.10. The modules consist of a $20\mathrm{x}20\mathrm{x}10\,\mathrm{mm}^3$ (24 g) scintillating $CaWO_4$ single crystal as target (phonon detector). The crystal is held by instrumented $CaWO_4$ sticks, meaning that the stick is equipped with a TES and read out individually to discriminate holder-induced events originating from, e.g., alphas due to surface contamination. The phonon detector is equipped with a tungsten TES used as a thermometer, directly evaporated on the crystal. The light detector is mounted next to the crystal and is made from a silicon-on-sapphire wafer with a size of $20\mathrm{x}20\mathrm{x}0.4\,\mathrm{mm}^3$. Not-instrumented $CaWO_4$ sticks do the holding of the detector.
External companies from Russia and Ukraine produced the scintillating $CaWO_4$ crystals in the first phase of CRESST-II. The Technische Universität München (TUM) started to grow $CaWO_4$ crystals in-house using the Czochralski method in 2007 to have control of the radiopurity, the crystal growth parameters, and the production process. In the second phase of CRESST-II,

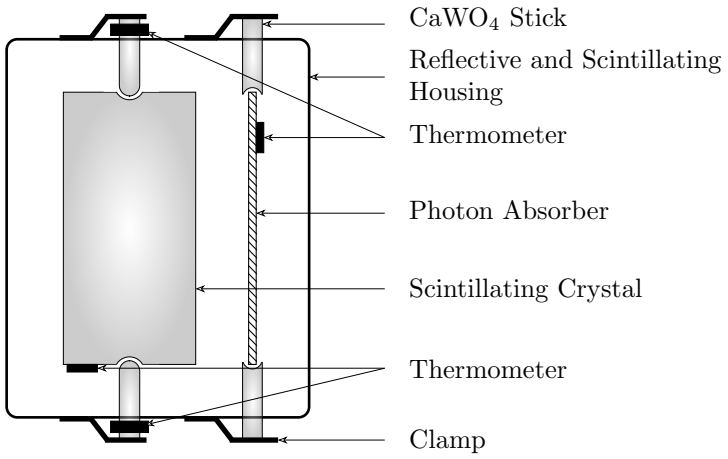

Figure 1.9: Schematic drawing of a standard CRESST-III detector module. The module contains a phonon detector with a 24 g CaWO4 target crystal equipped with an evaporated TES. The light detector consists of a silicon-on-sapphire (SOS) wafer. The SOS is also equipped with an evaporated TES. Both detectors are enclosed in a reflective and scintillating housing. The detectors are held via $CaWO_4$ sticks. Each stick holding the crystal (called i-stick) is connected to a TES to discriminate events in the sticks.

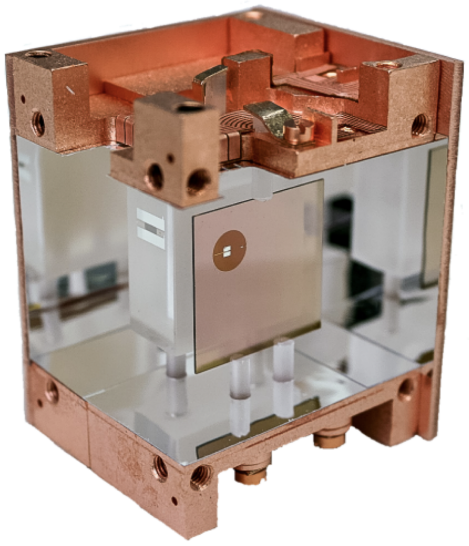

Figure 1.10: Photograph of an opened CRESST-III detector module. The module contains two independent cryogenic detectors, a 24 g $CaWO_4$ target crystal with a direct evaporated TES on it for the readout of the phonon signal, and second a silicon-on-sapphire (SOS) wafer for measuring the scintillation light from the target crystal. The wafer is also linked to a TES. Both detectors are enclosed in a reflective and scintillating housing.

several TUM-grown crystals were installed and demonstrated a radiopurity improved by a factor of 2 - 10 compared to commercial crystals [79][80][81]. The best threshold achieved was a nuclear recoil energy threshold of ~ 307 eV [82]. The best-performing detector in the first phase of CRESST-III was detector A with a threshold of only 30.1 eV [48]. The detector crystal of detector A is a TUM-grown $CaWO_4$ crystal with a high radiopurity compared to commercial $CaWO_4$ crystals.
The crystal and the light detector are enclosed in a reflecting and scintillating housing to collect as much light as possible. For this purpose, a multilayer specular reflecting foil ("Vikuiti") produced by 3M [83] is mounted on the inside of an ultra-pure copper housing structure.

1.5.3 Background Discrimination

As mentioned before, both CRESST-II and CRESST-III use the phonon-light technique for active background discrimination. The main radioactive background in the experiment is due to electron and gamma-induced events. However, alpha events on surfaces or thermal, epithermal, and slow neutrons also represent a source of background. Signals potentially induced by Dark Matter particles are nuclear recoils on tungsten, oxygen, and calcium in the $CaWO_4$ crystal.

With the simultaneous detection of the phonon and light signal, a discrimination of different kinds of interacting particles is possible by introducing the so-called light yield (LY), which is distinct for each type of particle ($\sim 5\%$ scintillation light of the energy deposited [84]). The light yield depends on the energy (E) deposited in the crystal. It is defined as the ratio of the energy deposited in the light detector $E_{Light}(E)$ and the energy deposited in the phonon detector $E_{Phonon}(E)$:

$$LY(E) = \frac{E_{Light}(E)}{E_{Phonon}(E)} \tag{1.6}$$

In most target materials, electron recoils produce the highest amount of light and have, therefore, the largest LY. Alpha events and nuclear recoils, however, lead to a lower light yield due to a quenching effect [85]. With the light yield, defined particle discrimination is possible.
The cross-section for spin-independent coherent WIMP scattering is proportional to A^2, where A is the mass number of the target nuclei. For highly ionizing particles, a reduced LY compared to electron recoils is expected from the quenching mechanism [86].
A typical light yield plot is shown in figure 1.11 with its individual recoil bands. The electron/gamma band (e^-/γ) where e^- and gammas are found is printed in blue. The light yield is defined to be 1 for γs with an energy of 122 keV of a ^{57}Co source. The scintillation efficiency of $CaWO_4$ is interaction type-dependent and can be expressed by a constant quenching factor QF_x for the specific type of interaction x, and the gamma light yield L_γ:

$$LY_x = QF_x \cdot LY_\gamma \tag{1.7}$$

Since Dark Matter particles are expected to scatter off one of the target nuclei, they occur in the nuclear recoil bands (oxygen (O, in red), tungsten (W, in green), or calcium (not included for clarity). The yellow region (region of interest (ROI)) is defined as the region with an upper energy limit of 16 keV and an upper LY limit of the mean of the oxygen band down to the 99.5 % lower boundary of the tungsten band.
The precise knowledge of the quenching factors is essential for the CRESST experiment. The current values for the QF are given by: $QF_O = (11.2\pm0.5)\%$, $QF_{Ca} = (5.94 \pm 0.49)\%$ and $QF_W = (1.72 \pm 0.21)\%$ [87].

1.5.4 The Low Energy Excess

In CRESST-III, an unexpected signal in the previously inaccessible energy range below 200 eV was measured. This signal is shown in figure 1.12. In grey, all events are shown, and in red, only the events in the acceptance region of the Dark Matter analysis. The events raise exponentially from an energy

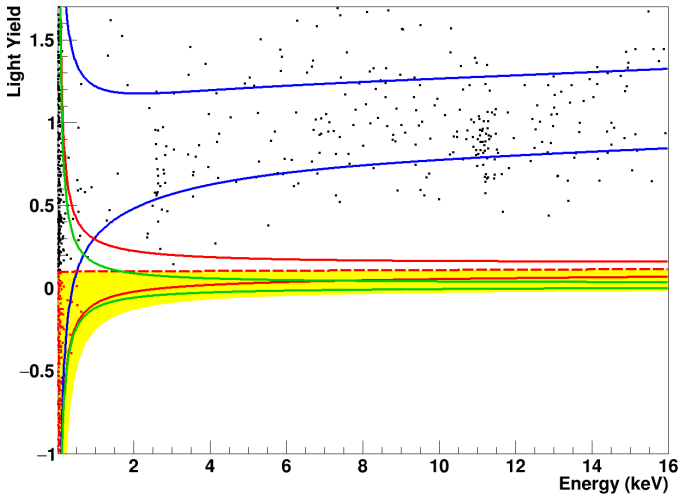

Figure 1.11: Light yield versus energy. Data points are drawn in black dots. The electron/gamma band (e^-/γ) where e^- and gammas are found is printed in blue. The light yield is defined to be 1 for γs with an energy of 122 keV. Since Dark Matter particles are expected to scatter off one of the target nuclei, they are expected in the nuclear recoil bands (oxygen (O, in red), tungsten (W, in green), calcium (not included for clarity). The yellow region (region of interest (ROI)) is defined as the region with an upper energy limit of 16 keV (where the detector energy response is still linear) and an upper LY limit of the mean of the oxygen band down to the 99.5 % lower boundary of the tungsten band. The picture was taken from [48].

of around 200 eV towards the detector threshold. This effect is called Low Energy Excess (LEE) in the DM community. The origin of those events is still unknown. The pulse shape of the excess events can not be distinguished from events induced by a particle interaction at higher energies. As mentioned, the light output at lower energies is rather low, which means that events caused by a nuclear recoil can not be distinguished from an electron/gamma event. Also, noise triggers can be excluded since only 3.6 events are expected. This effect is also seen in other CRESST detectors with a sufficiently low threshold but different spectral shapes of the excess events. Therefore, an origin like, e.g., Dark Matter is excluded [88][89][90]. There are some ideas about the origin which are still under investigation. A not complete enumeration of these ideas are

- Stress-induced events due to the holding of the crystal or internal stress
- Events from the reflecting foil
- Material hardness
- Thermal, epithermal, and slow neutrons

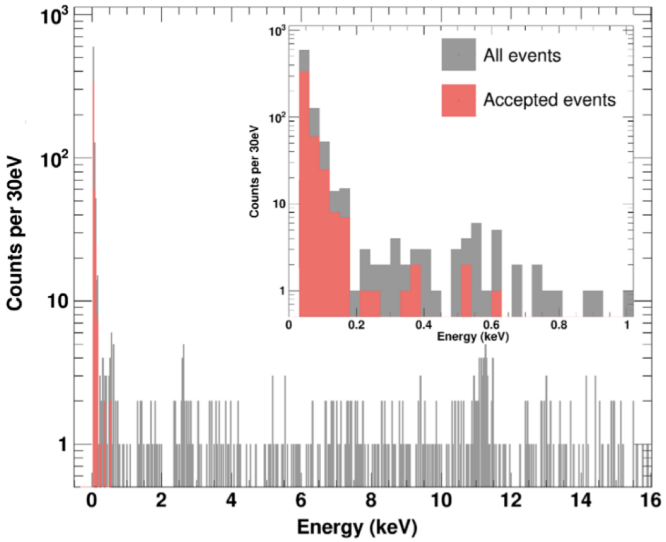

Figure 1.12: Energy spectrum of the Dark Matter data set of detector A. *Grey*: All events. *Red:* Only the events in the acceptance region for the Dark Matter analysis. The picture was taken from [88].

Not only the CRESST experiment is investigating the low energy excess but also several other experiments. Since the energy region of the excess events is in the region of interest, an understanding of the observed excess events is essential for current low-threshold experiments, not only for low-mass Dark Matter but also for coherent elastic neutrino-nucleus scattering (CEνNS). To investigate the origin, recently, a workshop took place with contributions from CONNIE, CRESST, DAMIC, EDELWEISS, MINER, NEWS- G, NUCLEUS, RICOCHET, SENSEI and SuperCDMS collaborations [88] (and references therein).

1.6 Backgrounds in Dark Matter Experiments

Knowing the background is a crucial point for Dark Matter experiments like CRESST. In the region of interest (ROI) below 10 keV, numerous backgrounds arise from α's, electromagnetic interactions, neutrons, electrons, and *gamma*s. A detailed description of these backgrounds can be found in [91] and is briefly discussed in the following.
γ's can deeply penetrate the target crystal and do Compton scattering, leading to an electron-recoil background. γ's are mainly produced during radioactive decays of radioactive isotopes. They are present in trace amounts inside the crystal and the surrounding materials, e.g., the rock and shielding. Common elements are ^{40}K and isotopes from the ^{235}U, ^{238}U and ^{232}U decay chains. The amount of γ rays reaching the detectors can be reduced by

passive shielding around the experiment. Typical materials are high-purity lead and copper, which are well suited to shield against γs because of the large number of nucleons. Lead, in addition, has a low neutron cross-section and a low interaction probability with cosmic rays. Ancient lead, often called roman lead, has a very low ^{210}Pb activity because of its age and is often used as the innermost gamma shield. A series of different methods can clean copper and is, therefore, well suited as shielding. Often water Cherenkov detectors are used in addition to shield against γs.
α's are often too highly energetic to be a dangerous background but can produce radiogenic neutrons from (α, n) reactions in materials with a large alpha-capture cross-section. Typical materials are, e.g., Teflon and polyethylene. Radiogenic neutrons are also produced during spontaneous fission. Those neutrons have to be moderated via scattering processes. Plastic or water, which are rich in hydrogen, are excellent neutron moderators.
Neutron scattering off target nuclei and, with a better detector sensitivity,

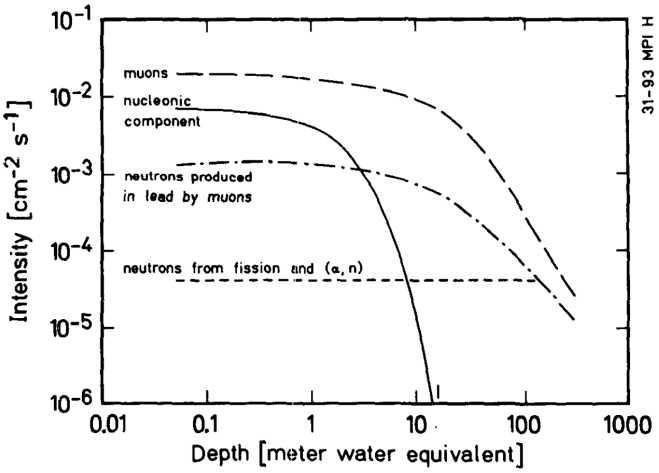

Figure 1.13: Flux of cosmic ray secondaries and tertiary produced neutrons in a typical lead shield versus the shielding depth. The neutron flux from natural fission and (α, n) reactions is also shown. The figure is taken from [92].

coherent neutrino-nucleus scattering can lead to a nuclear-recoil background similar to a Dark Matter signal. Neutrons are uncharged particles that are not interacting electromagnetically and can, therefore, mimic a Dark Matter particle. As mentioned, neutrons are produced by (α, n) reactions but can also be produced by cosmic radiation due to spallation reactions of muons on nuclei in the experimental setup, e.g., the lead shielding or in the surrounding rock. For Dark Matter experiments deep underground, the muon flux is significantly reduced, leading to a lower neutron rate. Still, it can play an important role in low overburden experiments, e.g., CEνNS experiments. Figure 1.13 shows the flux of cosmic ray secondaries and tertiary-produced

neutrons in a lead shield versus the shielding depth. The figure shows a constant neutron background originating from natural fission and (α, n) reactions. The muon-induced neutrons produced in the lead play an important role for shallow underground laboratories with less than 100 m.w.e. like the underground laboratory in Garching, which is described in chapter 2.1. But also, for deeper underground laboratories, the muon neutron background should not be neglected.
A detailed understanding of the neutron background is needed for low overburden rare event search experiments like the CEνNS experiment NUCLEUS [93]. But also for Dark Matter experiments like CRESST, the knowledge about the in-situ neutron background is mandatory with respect to the gain in sensitivity in this field. Therefore, a suitable method had to be found to measure the (muon-induced) neutron flux in the experimental volume after the moderation of the neutrons took place. In the scope of this thesis, a lithium-based cryogenic neutron monitoring system was developed. A description of the detector and its working principle can be found in chapter 3. In addition, a simulation tool was developed to receive information about the spectral shape of the initial neutrons.

Chapter 2

Cryogenic Setup in the Underground Laboratory Garching

The Physics Department of the Technical University of Munich (chair E15 for experimental astroparticle physics) runs a unique experimental site in Garching, the shallow underground laboratory (UGL) [94]. With a shallow overburden and facilities such as a clean room, the UGL offers unique conditions for R&D and measurements. The UGL houses several different experiments from different collaborations, e.g., a ^{3}He/^{4}He dilution refrigerator for the CRESST [48][70][82][95] and NUCLEUS [93] experiment. In the scope of this thesis, a cryogenic characterization facility was reestablished, and major upgrades were done. In the following, an overview of the UGL is presented. Afterward, the cryogenic characterization facility is described as used for the measurements given in this work.

2.1 The Shallow Underground Laboratory in Garching

The shallow underground laboratory (UGL) operated by the Physics Department of the Technical University of Munich is located in Garching, Germany, and consists of two laboratory spaces. The initial shallow underground laboratory featured an area of $30\,\mathrm{m}^2$ (UnderGround Laboratory 1, UGL1). It was part of the Maier-Leibnitz-Laboratorium (MLL) for time-of-flight measurements before it was used as an underground laboratory. In 2011, a second laboratory (UnderGround Laboratory 2, UGL2) was constructed, extending the laboratory area significantly to $\sim 160\,\mathrm{m}^2$ (UGL1 + UGL2). This extension was primarily funded by the German excellence initiative (DFG). The underground laboratory is shielded from cosmic rays by an overburden

of $\sim 6\,\mathrm{m}$ of soil and gravel. This corresponds to a shielding of $\sim 15\,\mathrm{m.w.e.}$ and reduces the flux of atmospheric muons by a factor of ~ 3 and almost eliminates the flux of the hadronic components (see figure 1.13)[96][97]. In addition, a metallic mash was included during the construction to shield the UGL from radio sources. Further, the underground laboratory has a dedicated grounding available to reduce noise originating from the grounding. This makes the shallow underground laboratory an ideal site for developing and fabricating detectors for rare event searches such as direct dark matter searches, the detection of coherent neutrino-nucleus scattering, and the search for neutrinoless double beta decay. A schematic drawing and a side view of the shallow underground laboratory illustrating the overburden are shown in figure 2.1.

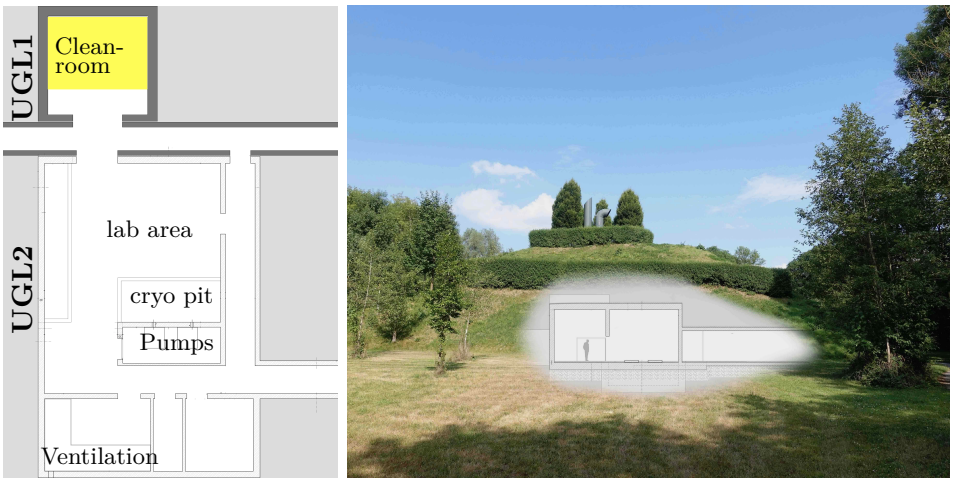

(a) (b)

Figure 2.1: a) Schematic drawing of the TUM shallow underground laboratory in Garching, Germany (UGL1 + UGL2). The available laboratory space is $\sim 160\,\mathrm{m}^2$. The lab consists of the lab area with a cryo pit, where the experiments are located, a dedicated room for the pumps in order to reduce noise induced by vibrations, and a room where the ventilation system is located. In the fall of 2016, a new cleanroom detector laboratory (class ISO 7, yellow-shaded area) was installed in UGL1. b) Illustration showing the shallow underground laboratory from the outside combined with a schematic side view of the laboratory. It is shielded from cosmic radiation by $\sim 6\,\mathrm{m}$ of gravel and soil, corresponding to a shielding of $\sim 15\,\mathrm{m.w.e.}$.

Several experimental activities rely on the shielding provided by the shallow underground laboratory:

- Two screening stations with high-purity germanium detectors (HPGe) are used to measure the radiopurity of materials used in the fabrication and assembly of detectors for rare event searches.

- A cryostat holding $\sim 1\,\text{ton}$ of liquid argon is used to characterize high purity Germanium detectors and develop novel background suppression techniques for the neutrinoless double beta decay experiments GERDA [98] and LEGEND [99].
- A $^3\text{He}/^4\text{He}$ dilution refrigerator and a pulse tube cooled cryostat, each with a base temperature of $\leq 10\,\text{mK}$ are used for the development and characterization of cryogenic particle detectors in the framework of the CRESST [48][70][82][95] experiment.
- A liquid scintillator test facility measures the attenuation length of liquid scintillators for neutrino experiments like JUNO [100].
- A cleanroom detector laboratory (class ISO 7) has been installed in UGL1.

2.2 Shallow-lab Cleanroom Detector Laboratory

For the construction of detectors for rare event searches, a cleanroom is a mandatory facility to avoid surface contaminations of the detectors. The construction of the so-called *shallow-lab cleanroom detector laboratory* in UGL1 finished at the end of 2016. It has an area of $\sim 25\,\text{m}^2$. It is certified according to the cleanroom standard ISO 7, which implies particles with $0.5\,\mu\text{m}$, $1\,\mu\text{m}$ and $2930\,\mu\text{m}$ can be only measured in concentrations below $352000\,\text{particles}/\text{m}^3$, $83200\,\text{particles}/\text{m}^3$ and $0,5\,\text{particles}/\text{m}^3$, respectively (DIN EN ISO 14644-1). The cleanroom is designed as a versatile detector laboratory, enabling detector fabrication and assembly for neutrinoless double beta decay experiments (GERDA & LEGEND), coherent neutrino-nucleus scattering experiments (NUCLEUS), and direct dark matter search experiments (CRESST). An image and a schematic drawing of the cleanroom are depicted in figure 2.2. The laboratory is equipped with a laminar flow workbench and a chemical wet bench with fume-hood. Furthermore, the cleanroom is equipped to process detectors utilizing photolithographic patterning. To this end, a spin-coater to apply photoresist as well as a mask-aligner[1] (model MA-1006, SÜSS, Germany) are available. The lighting in the cleanroom can be switched from white to yellow, preventing unwanted exposure of the photoresist. To facilitate electrical contacts on semiconductor detectors (e.g., silicon photomultipliers), cryogenic detectors as well as high-purity Germanium detectors, an ultrasonic wedge-bonding machine is available at the laminar flow workbench as well as an ultrapure-water system (Purelab Classic from ELGA, United Kingdom), reducing the resistivity of the clean water down to $18.4\,\text{M}\Omega/\text{cm}$. A nitrogen-flushed cabinet is also available to

[1] The mask-aligner is specially modified to process CRESST-II sized detector crystals with a height of up to $\sim 40\,\text{mm}$.

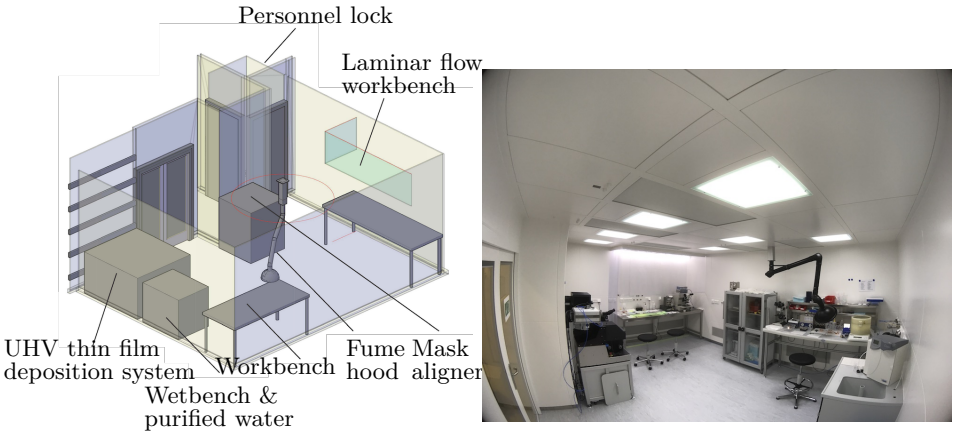

Figure 2.2: a) Schematic drawing and b) image of the shallow-lab cleanroom in UGL1. It consists of a laminar flow workbench, a wet bench with chemical fume-hood, and an ultrapure-water system (Purelab Classic from ELGA, United Kingdom). Additionally, for the photolithographic lift-off method, a spin-coater for depositing the photoresist and a mask-aligner (SÜSS MA-1006) for structuring the detectors are present. The detectors can be connected via aluminum wire bonding.

store detectors and raw materials used for detector assembly in a nearly radon-free environment. A highly efficient ventilation system ensures a full air volume exchange eight times per hour, leading to a radon level equivalent to the outside of the lab, which is approximately $10\,\mathrm{Bq/m^3}$.
To complete the detector fabrication capabilities of the laboratory, a UHV coating system (LAB 500, manufacturer Leybold) is installed with an electron beam evaporator and an Argon plasma source.

2.3 Experimental Applications in the framework of CRESST-III

Due to the infrastructure provided by the shallow underground laboratory, it is currently, among others, relevant for the development of cryogenic detectors in the framework of the CRESST-III experiment:

- The $CaWO_4$ target crystals used in the first phase of the CRESST-III experiment is primarily supplied by the Technical University of Munich. For the second phase of the CRESST-III experiment, it is foreseen that TUM will provide all target crystals. For CRESST-III phase I, three detectors from the TUM-grown crystal (TUM93) are built-in, with detector A having the lowest threshold of 30.1 eV [48].

The crystals are grown and processed in-house at TUM [81][101] to directly influence the crystal growth parameters and their radiopurity. For the second phase of CRESST-III, an improved radiopurity by a factor of 100 compared to the TUM40 crystal is planned [48]. To achieve the required radiopurity of the $CaWO_4$ crystals, measurements of the crystals as cryogenic detectors are needed to assess their contamination with α-decaying isotopes effectively [80]. These measurements will be performed in the cryogenic setup available in the shallow underground laboratory with a dedicated module [102] to provide direct feedback on the crystal growth. Because of the reduced muon rate and the vetoed hadronic components, the crystals are stored in a nitrogen cabinet in the UGL, which allows faster access to the crystals than, e.g., the LNGS.

- The characterization and assembly of detector modules for the second phase of the direct dark matter search experiment CRESST-III is currently planned to partially take place in UGL, in addition to the infrastructure available at the Max-Planck Institute for Physics, Munich, Germany, and the University of Tübingen, Tübingen, Germany.

Further applications of the shallow underground laboratory include the characterization of gram-scale cryogenic detectors to search for coherent neutrino-nucleus scattering with the NUCLEUS experiment [93].

2.4 Working Principle of a ^{3}He/^{4}He Dilution Refrigerator

The story of ^{3}He/^{4}He dilution refrigerators started in 1951 when H. London discovered a new cooling mechanism using the isotopes ^{3}He and ^{4}He [103]. The first dilution refrigerator was built in 1965 by Das and others at Leiden University, reaching a temperature of 220 mK [104]. Nowadays, dilution refrigerators reach stable temperatures below 7 mK. The lowest temperature reached with dilution refrigerators was 1.75 mK by D. J. Cousins and others [105].

The cooling process uses the characteristics of a ^{3}He/^{4}He mixture in the few Kelvin regime. Figure 2.3 shows the phase diagram of a mixture of ^{3}He and ^{4}He as a function of the ^{3}He concentration, c. The λ line represents the phase transition between a liquid helium mixture and Fermi liquid of ^{3}He diluted in supra-fluid ^{4}He. Below 0.8 K (tricritical point), the mixture separates into two different coexistent phases; a ^{3}He rich (concentrated) phase and a ^{3}He poor (dilute) phase. The area below the two phases is forbidden. By lowering the temperature, T, the point (T, c) moves in two directions according to the phase boundary. For the concentrated phase, the concentration c of ^{3}He is increasing and converges to 1 for $T \to 0$. The opposite happens for the dilute

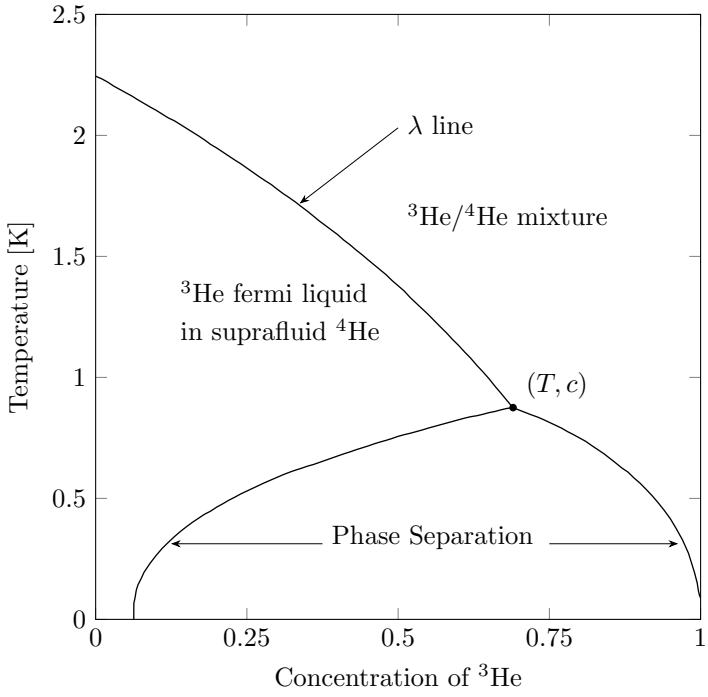

Figure 2.3: Phase diagram of a mixture of ^{3}He and ^{4}He. Starting from a point with temperature T and concentration c, a reduction of the temperature would lead to a change in the ^{3}He concentration according to the phase transition. For the extremum of $T \to 0$, the concentration c of the depleted phase has its minimum at 6.48 %. For the concentrated phase, the concentration of ^{3}He reaches 1. Data were taken from [106].

phase. There, the ^{3}He concentration c is decreasing. The concentration in this case converges to a constant ^{3}He concentration of 6.48 % for $T \to 0$. The finite solubility of ^{3}He in ^{4}He results from the different zero-point energies of the two isotopes. ^{4}He with spin $S = 0$ is a boson and, thus, follows the Bose-Einstein statistics. ^{3}He has spin $S = 1/2$ and is, therefore, a fermion, following the Fermi-Dirac statistics. Because of its fermionic properties, the zero-point energy is much higher for ^{3}He than for ^{4}He. In equilibrium, the two chemical potentials of the concentrated $\mu_{3,c}(T, c_{3,c})$ and the dilute $\mu_{3,d}(T, c_{3,d})$ phase have to be equal [107].

$$\mu_{3,d}(T, c_{3,d}) = \mu_{3,c}(T, c_{3,c}) \tag{2.1}$$

As mentioned, the ^{3}He concentration in the concentrated phase is 1 for $T = 0$. The required energy to move an atom in a vacuum can be explained by the latent heat per atom $L_3(T = 0)$. The chemical potential can than be written as $\mu_{3,c}(0, 1) = -L_3(0)$. For the dilute phase the binding energy of one ^{3}He

atom in liquid ^{4}He at $T = 0$ and $c_{3,d} \to 0$ is given by $E_3 = -\mu_{3,d}(0,0)$. In addition, the Fermi energy $E_F = k_B T_F(c_3)$ has to be included, with the Fermi temperature T_F. The equilibrium concentration of ^{3}He in liquid ^{4}He at $T = 0$ is than given by

$$-L_3(0) = -E_3(0, c_3) + k_B T_F(c_3) \tag{2.2}$$

From this equation, the concentration c_3 can be derived, leading to a value of 6.48 % [107]. If ^{3}He is removed from the dilute phase, ^{3}He diffuses from the

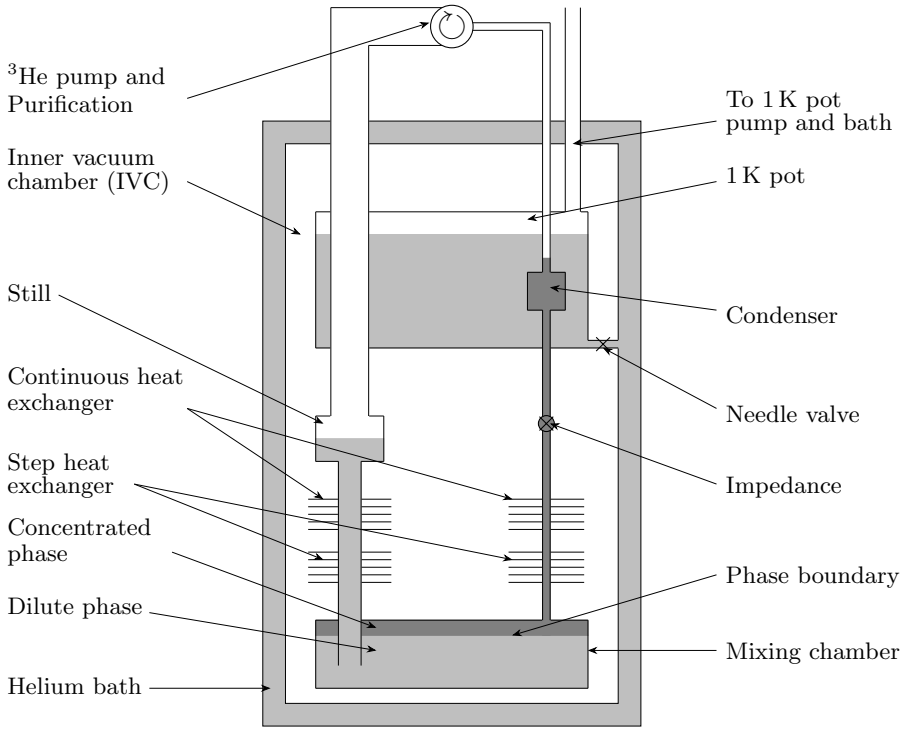

Figure 2.4: Schematic drawing of the mixing circuit. Inside the mixing chamber ($\sim$ 10 mK), a ^{3}He rich (concentrated) phase and a ^{3}He poor (dilute) phase are separated via a phase boundary. Via pumping on the still ($\sim$ 600 mK) ^{3}He is extracted continuously from the system to the outside of the cryostat ($\sim$ 300 K). The dilute phase compensates for the missing ^{3}He by the diffusion of ^{3}He from the concentrated phase into the diluted phase. The extracted ^{3}He gas is guided back to the cryostat to the condenser, a thin capillary down to the impedance. The gas is cooled by the 1 K pot and two heat exchangers to liquefy the gas. The 1 K pot is filled via a needle valve. Due to pumping on the 1 K pot, the helium evaporates, which cools the system. The liquid helium drops back into the mixing chamber and can diffuse again into the dilute phase.

concentrated phase into the dilute phase to restore the equilibrium conditions. Because of the different enthalpies of the two phases, heat is detracted from the system, which defines the cooling mechanism of a dilution refrigerator.
A schematic drawing of a mixing unit is shown in figure 2.4. The mixing circuit consists of three main parts, the mixing chamber, the still, and the condenser. Inside the mixing chamber ($\sim 10\,\mathrm{mK}$), a ^{3}He rich (concentrated) phase and a ^{3}He poor (dilute) phase are separated via a phase boundary. Since ^{3}He is lighter than ^{4}He, the concentrated phase is on top of the dilute phase. The mixing chamber is connected to the still ($\sim 600\,\mathrm{mK}$) via a tube so that the dilute phase fills the still. Via pumping on the still, ^{3}He is extracted continuously from the system to the outside of the cryostat ($\sim 300\,\mathrm{K}$) because of the lower boiling point of ^{3}He with 3.2 K compared to ^{4}He with 4.2 K [108]. As explained above, the dilute phase compensates for the missing ^{3}He by the diffusion of ^{3}He from the concentrated phase into the diluted phase resulting in a cooling of the mixing chamber.
The extracted ^{3}He gas is cleaned via cold traps and guided back into the cryostat. The condenser, which is a thin capillary, re-liquifies the helium. The gas is cooled by the 1 K pot and two heat exchangers. The 1 K pot is filled via a needle valve. Due to pumping on the 1 K pot, the helium evaporates, which cools the system. The liquid helium drops back into the mixing chamber to the concentrated phase and can diffuse again into the dilute phase.

2.5 ^{3}He/^{4}He Dilution Refrigerator in the UGL

To accommodate up to three cryostats and to allow ground-level access to the top of the dewar, the shallow underground laboratory is equipped with a so-called cryo-pit, a rectangular hole with a size of $6\,\mathrm{m} \times 2\,\mathrm{m}$ and a depth of $\sim 2\,\mathrm{m}$. A ^{3}He/^{4}He dilution refrigerator (model Kelvinox 100 from Oxford Instruments plc, UK) is installed there. The cryostat has a cooling power of $\sim 140\,\mu\mathrm{W}$ at a temperature of 100 mK and is capable of reaching a base temperature of $\leq 10\,\mathrm{mK}$.
An illustration of the experimental setup is shown in figure 2.5. The liquid helium reservoir lasts for approximately five to six days, enabling longterm-measurements of cryogenic detectors for a duration of several months under very stable conditions.
The external lead shielding is enclosed by a nearly 4π active muon-veto which improves the capability for low-background measurements significantly [109][97]. The experimental volume below the mixing chamber has a diameter of 98 mm and a height of 300 mm. The maximal crystal mass that can be operated above ground, having a tolerable detector counting rate caused by cosmic rays, is approximately 100 g. Since the flux of muons in the UGL is reduced by a factor of ~ 3, an increased acceptable maximal crystal mass of the same order can be expected.

The cryogenic system can be cooled from room temperature down to its base temperature of 10 mK in $\sim$ 48 h. The main steps of a cool-down are typical:

1. Connecting and evacuating of all pumping lines like the 1 K pot tube, the condenser line, and the still line.
2. Evacuation of the inner vacuum chamber (IVC) overnight to a pressure $< 5 \cdot 10^5$ mbar. Afterward, 5 cm^3 of ^{4}He gas are injected as exchange gas to cool the insert in a reasonable time.
3. First pre-cooling step to < 100 K of the complete insert by filling the dewer with $\sim$ 20 l of liquid nitrogen (lN2). The exchange gas acts as the thermal link.
4. Removal of lN2 from the dewar and flushing of the system with ^{4}He gas to avoid freezing of the nitrogen in the 1 K needle valve in a later stage.
5. Second pre-cooling step to < 7 K of the complete insert by filling the dewar with liquid helium (lHe). Again, the injected exchange gas acts as the thermal link.
6. Removal of the ^{4}He exchange gas via pumping on the IVC. This step is typically done overnight.
7. Complete filling of the cryostat dewer with lHe.
8. Cooling to $\sim$ 1.5 K via the 1 K pot, which cools the setup via evaporation on lHe while pumping on the 1 K pot. The helium is taken from the liquid helium bath and pumped via a sniffler into the 1 K pot.
9. Condensation of the ^{3}He/^{4}He mixture into the mixing chamber.
10. Setup of the electronics to monitor transitions.
11. Start the circulation of the mixture.

The cryogenic system is optimized for the operation of TES (Transition Edge Sensor) based detectors read out via DC-SQUIDs (Superconducting QUantum Interface Device). Furthermore, wiring required for the operation of NTLE (Neganov-Trofimov-Luke Effect) cryogenic light detectors[110][111] is also available in the cryostat.
The cryostat was installed in its current position in the cryo pit of UGL2 in Q1 2017 after its old place in UGL1 became unavailable due to the construction of the shallow lab cleanroom. Since the system was already outdated, the relocation was used to do major modifications to the cryostat setup to build up an entire cryogenic characterization facility with a CRESST-like data acquisition. The modifications were divided into working packages realized stepwise and described in the following.

1. *Relocation of the cryogenic infrastructure*, including the relocation of the lead castle to the new cryo pit, the insertion of the dewer to the new lead castle, construction of the pumping and mixture lines infrastructure, and the gas handling

2. *Installation of new oil-free pumps.*

3. *Modification of the data acquisition.*

4. *Recabling of the cryostat insert,* including bias and heater lines as well as lines for temperature read-out and a 3-channel SQUID system.

5. *Relocation and modification of the muon veto.*

In the following, the working packages are explained in more detail.

2.5.1 Rebuilding of the Cryogenic Infrastructure

As a first step, the complete cryogenic setup had to be rebuilt. To shield the cryostat against ambient natural radioactivity from the laboratory walls, it is surrounded by a lead shielding with a thickness of $\sim 10 - 15\,\mathrm{cm}$ and a total weight of $\sim 10\,\mathrm{t}$. Figure 2.5 shows a schematic drawing of the cryogenic setup. As indicated there, the lead castle is built on a wooden pedestal for height compensation to the ground floor. On top of a $\sim 40\,\mathrm{cm}$ platform made of lead bricks, lead hollow cylinders with a diameter of 15 cm are stacked with a total height of $\sim 2\,\mathrm{m}$. The dewar is sitting on the top lead cylinder and is then surrounded by another 30 cm of lead hollow cylinders with a diameter of 10 cm. If needed, the lead castle is open on the top side but can be closed by lead cylinders. The pumping lines had to be redesigned. Initially, the pumping lines were made from soft vacuum tubes. To reduce vibrations, those tubes were exchanged for stainless steel tubes fixed on the walls of the cryo-pit and guided through the wall into the pumping room.

2.5.2 Installation of New Oil Free Pumps

To reduce vibrations originating from the coupling of the pump to the cryostat, ultimately resulting in microphonic noise, all pumping units (1 K pot pump, mixing circuit pump, and booster pump) are located in a separated pumping room and are decoupled from the floor using a damped platform.

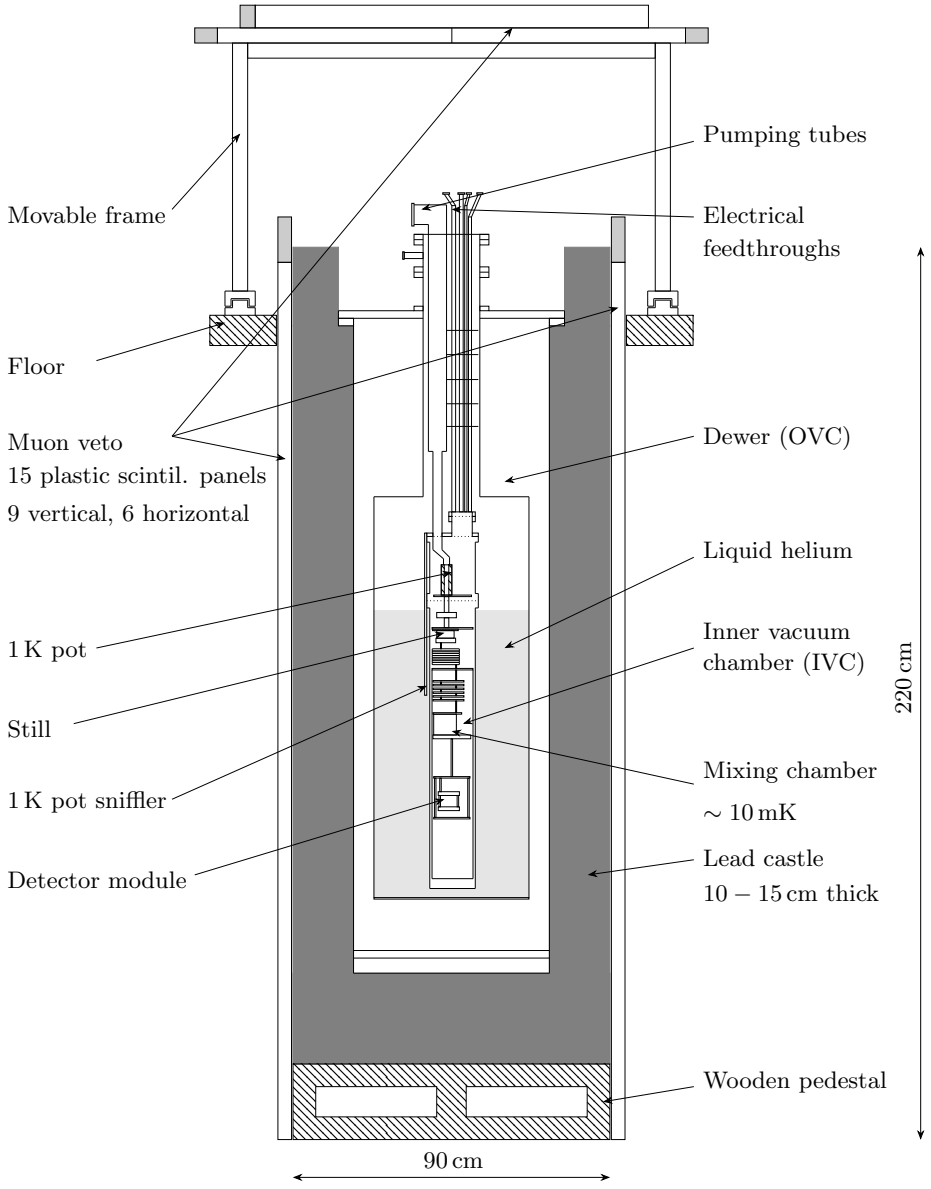

Figure 2.5: Schematic drawing of the cryogenic setup in the UGL. In the center is the Kelvinox 100 ^{3}He/^{4}He dilution refrigerator from Oxford Instruments plc, UK. The cryostat is surrounded by an external lead shielding (lead castle) enclosed in a nearly 4π active muon-veto. The horizontal panels can be moved via a movable frame to guarantee an easy refill of the cryostat.

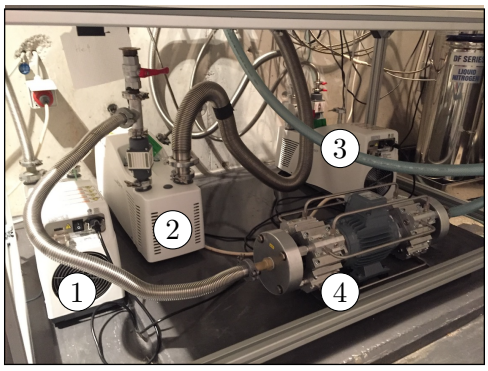

Figure 2.6: New oil-free pumping units. (1): Booster pump, (2): 1 K pot pump, (3): mixing circuit pump, (4): diaphragm pump for 1 K pot pump backup.

There is only one exception; to guarantee a pressure below 10^{-1} mbar for efficient circulation of the mixture, a ^{3}He turbo pump is mounted inside the cryo pit, very close to the lead castle. A T-ballow is mounted on top of the turbo pump to decouple from the cryostat in the sense of vibrations effectively. Additionally, the frame is loaded with lead bricks to dump any vibrations. The turbo pump is a HiPace 400 with a DN 100 ISO-F flange and a gas throughput at final rotation speed for helium of $4\,\mathrm{hPa}\cdot\mathrm{l/s}$, produced from Pfeiffer, Germany [112]. In the original setup at UGL 1, no turbopump was connected to the cryostat. It was installed in the cryostat upgrade to enlarge the pumping power and, therefore, lower the base temperature of the cryostat. All pumps of the old setup were oily pumps. This has the disadvantage that oil partially gases into the pumping lines of the mixing circuit. To reduce the impurities of the mixture (which could lead to a block in the condenser), all pumps were exchanged with oil-free pumps, type ACP40 from Pfeiffer, Germany [112] (see figure 2.6 1-3). Additionally, the mixing circuit pump is sealed and tested to be tight for helium gas not to lose the mixture. To increase the pumping power of the ACP40 for a lower 1K pot pressure, the ACP40 is backed up by a PB 9 8-cylinder diaphragm pump from hyco Vakuumtechnik GmbH, Germany [113] (see figure 2.6 4).

2.5.3 Modification of the Data Acquisition

To upgrade the cryostat, the data acquisition (DAQ) was completely exchanged to be fully compatible with the electronics used in the direct dark matter search experiment CRESST. The VME-based data acquisition (DAQ) system consists of a VME interface card (model SIS1100e, SIS GmbH, Germany), a 16-channel transient recorder (model VD80, INCAA Computers B.V., Netherlands), a 4-channel arbitrary waveform generator (model V375, Highland Technology, USA), a digital voltmeter and a digital-to-analog converter (models PAS 9737 and PAS 9816, Precision Analog, USA) as well

as custom build analog filter modules. This DAQ system enables active detector stabilization. A more detailed description of the DAQ can be found in chapter 3.11.

2.5.4 Recabling of the Cryostat Insert

All electronic measurement equipment in the cryostat must be fed into the inner vacuum chamber. For the cabling of the cryostat, two different cable materials are used, depending on the temperature level. All bias, heater, and temperature read-out lines are constructed following this scheme. For cabling from 300 K down to the 4 K stage of the cryostat, the twisted-pair copper cable GVLZ081 from GVL cryoengineering GmbH [114] is used. It consists of two 0.15 mm thick copper wires, each coated with varnish. As shield, a CuNi mash (55 % Cu, 44 % Ni, 1 % Mn) is used. The cable is, in addition, encapsulated by a Teflon shield and has a total diameter of 1.2 mm and a normal conducting resistance of $R_{wire} = 1.1\,\Omega/\mathrm{m}$. For the cables going down from 4 K to the mixing chamber, a twisted pair Nb/Ti cable (GVLZ030 from GVL cryoengineering GmbH [114]) is used. The cable consists of two 0.1 mm thick NbTi in CuNi matrix (90 % Cu, 10 % Ni) wires each coated with varnish. The ratio of NbTi to CuNi is in the order of 1/1.5. Again the cable is encapsulated in a CuNi mash (55 % Cu, 44 % Ni, 1 % Mn) shield and Teflon as outer layer. It has a total diameter of 0.8 mm and a normal conducting resistance of $R_{wire} = 41\,\Omega/\mathrm{m}$. The cables are shielded to avoid electromagnetic noise. Below 10 K, these NbTi cables become superconducting and are, therefore, well suited for low-resistance cabling in the cryostat.

Detector Read-Out

The cryostat is designed for the operation of TES-based cryogenic detectors and is, therefore, equipped with a DC-SQUID system (Superconducting QUantum Interface Device). The SQUID system was upgraded after the relocation of the cryostat from a 4-channel read-out system (model CS-blue from Supracon, Jena, Germany) to a new 3-channel system (model C6L1 from Magnicon, Hamburg, Germany [115]). For the old Supracon system, single electronics for each channel were necessary, whereas the electronics for the new Magnicon system is included in one single electronic. Further, the new system has a computer interface to optimize all channels and load the optimized SQUID settings afterward for comparable runs.

Figure 2.7: *Upper left:* Three channel SQUID system from Magnicon with the 300 K connector and the three SQUIDs which are located at 1.5 K. Figure adopted from [115]. *Bottom left:* The SQUID is encapsulated in a niobium housing (long grey cylinder). Adopted from [115]. *Right:* The SQUIDs are mounted on the 1 K pot stage. Additional copper strings are screwed between the 1 K pot stage and the SQUID frame for a better thermal link.

The Magnicon SQUIDs have niobium superconducting coils which have a transition to their superconducting phase below 9.25 K [116]. Therefore, the SQUIDS must be placed in a position well below this temperature. On the other hand, they should be placed on the highest stage possible to reduce thermal load to lower stages, ending in a higher base temperature. In the UGL cryostat, they are mounted on the 1K pot stage where the temperature is well below 9 K and the thermal load is minimal. Figure 2.7 right side shows the three SQUIDs mounted in a copper frame on the 1 K pot stage. The SQUID itself is encapsulated in a niobium housing (long grey cylinder, fig 2.7 bottom left) to shield the SQUID from electromagnetic fields. For a better thermal link, additional copper strings are screwed between 1 K pot stage and SQUID frame. The three-channel Magnicon system consists of a 24-pin LEMO socket where a $\sim$ 1 m long copper/alloy30[2] wire bundle in a silicon tube has to be soldered. For each channel, 8 0.2 mm thick wires are foreseen (one single wire, two twisted pairs, and one twisted triple). The cable is manifold into three lines for the last 25 % each ending in a plug (figure 2.7 top left).

[2] alloy30 composes 98 % Cu, 2 % Ni with a specific resistivity of 4.99 $\mu\Omega$/cm

Temperature Read-Out

The temperature read-out is realized with two different systems. First, an internal temperature read-out is available, as Oxford supplies it. Thermometers are installed on the 4 K plate, 1 K plate, and the mixing chamber. Each of these plates is equipped with a dedicated ohmic heater. Using a PID controller can also stabilize the mixing chamber, as it is included in the cryostat software. Second, four calibrated diodes from Lakeshore (Model 325 Temperature Controller [117]) is used to control the temperature during the cool-down. Those diodes have a large dynamic temperature range from 1 K up to 300 K and are therefore well suited to monitor the temperature during the cool down. Three diodes are located close to the one installed from Oxford. In addition, a fourth diode is installed below the IVC to control the filling level during the cool-down. The third temperature read-out system is a commercially available system from Lakeshore (Model 372 AC Resistance Bridge [117]). A two-channel read-out was mounted down to the mixing chamber of the cryostat. The system reads out two ruthenium oxide thermometers (RuOx) calibrated down to 7 mK, delivered and calibrated from Bluefors (RU-1000-BF0.007), Helsinki, Finland [118]. With those thermometers, it is possible to monitor the mixing chamber temperature precisely and stabilize the mixing chamber with a PID controller included in the DAQ software.

4 K Filter Boards

Each bias and heater line is filtered by a 4-π-filter, consisting of 4 equal resistances of 10 kΩ (heater lines) and 100 kΩ (bias lines) combined with a 1 nF capacitor (see figure 2.8).
The capacitors are Surface Mounted Device type (SMD) made from NP0. The SMD resistances are made from Ni/Cr to keep the resistance constant over a wide temperature range. The cut-off frequency f_{3dB} is the frequency where the signal is reduced by 3 dB (factor 0.707) and can be calculated via

$$f_{3dB} = \frac{1}{2\pi RC} \tag{2.3}$$

to be 1.6 kHz for bias and 16 kHz for heater lines. The filter boards are mounted on the 4 K stage to reduce thermal noise. The filter boards are at the position where the cable material is changing from copper to niobium-titanium to reduce the wire resistance to a minimum.

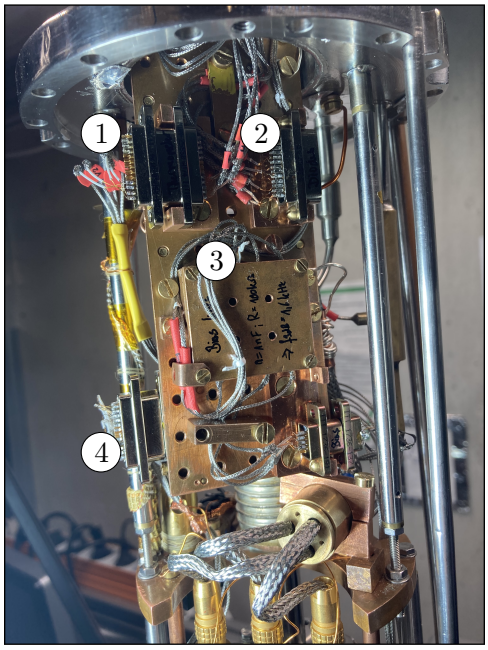

Figure 2.8: 4 K stage of the cryostat insert. 1: Wires for temperature read-out on the MC for RuOx thermometers, 2: Heater lines. Filter not visible on the back, 3: Bias lines with filter box, 4: Wires for temperature read-out with diodes.

2.5.5 Relocation and Modification of the Muon Veto

The decay of secondary charged pions and kaons predominantly creates atmospheric muons. They are the most abundant charged particles arriving at the surface of the Earth and can deeply penetrate the underground. The flux of atmospheric muons in the underground laboratory is reduced to approximately one-third because of 6 m soil, corresponding to 15 m.w.e..
The cryostat is equipped with an active muon veto relocated from the UGL1 location to identify muon-induced events effectively. For a more detailed description of the old muon veto system, the reader is referred to [96][97][119][120].
Figure 2.9 shows the installed muon veto in the underground laboratory surrounding the new cryostat setup in UGL2. The muon veto consists of 15 plastic scintillator panels as they have listed in table 2.1. The long panels of type I (Dimension 220x32x2.5 cm^3 with a 1" PMT on the short side of the panel) are positioned vertically in the cryo-pit (2). The panels of type II (Dimension 100x50x2.5 cm^3 with a 1" PMT on the short side of the panel) and type III (Dimension 100x50x5 cm^3 with a 2" PMT on the short side of the panel) are positioned on a movable frame (2)(3) to guarantee access to the filling port for the liquid helium refill.

	Dimensions [cm]	Quantity	PMT	HV [V]
Type I	220x32x2.5	9	1"	+1400
Type II	100x50x2.5	4	1"	+1400
Type III	100x50x5	2	2"	+1900
Total	8.6 m^2	15		

Table 2.1: List of all muon panels. On the site of the lead castle, the Typ I, on top of the cryostat, the Typ II and Typ III panels are used.

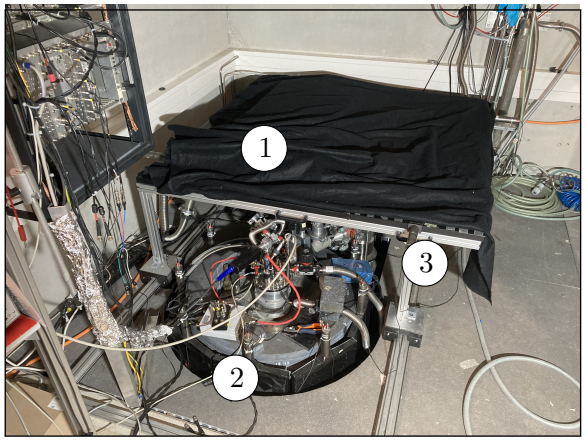

Figure 2.9: Muon veto of the cryogenic setup. 1: 6 horizontal panels covered with black fabric, 2: 9 vertical panels, 3: Moveable table for cryostat refill.

A major upgrade was done in terms of the electronics of the veto system to use the muon veto signals to identify muons and evaluate the background. For data acquisition, the fast analog to digital converter (FADC) SIS3316 from Struck Innovative Systeme is used [121]. The FADC consist of 16 VME digitizer channel. The threshold for each individual panel is set via a computer interface only to detect muons. In [109], a new analysis was developed to quantify the separation of the gamma background and muons by evaluating the peak-to-valley ratio. The output of all PMTs of the muon veto panels is combined in an OR logic by using the digital NIM trigger output of the FADC. The software used for the muon veto FADC was developed in [122], called LLAMA. The signal is afterward shaped in an external unit. The trigger logic is set to an "or" for all panels. Therefore, a trigger in one panel leads to a trigger of the muon veto system. The logical signal from the FADC is afterward shaped to a pulse-like signal with a length of 100 μs and recorded with the standard cryo data acquisition on a separate digitizer channel. The cryo data acquisition is not triggering on muon veto signals but writes the signal whenever a cryogenic detector is triggering. Thus, a trigger in the phonon detector leads to the simultaneous readout of the light detector and the muon veto channel. A detailed overview of the muon veto can be found

in [109].

Chapter 3

The Lithium - Fluoride Neutron Monitor

In the framework of this thesis, a cryogenic lithium-fluoride neutron monitoring system was developed, built, and tested to measure the neutron flux inside the experimental volume. The system can be used, e.g., in the CRESST setup, to in-situ monitor the neutron flux close to the detectors. The following chapter presents the lithium-fluoride detector and its basic working principle. In the end, the detector operation is described.

3.1 Thermal Detector Model

Cryogenic calorimeters rely on the detection of phonons by a sensitive thermometer like a so-called TES (transition edge sensor) as described in section 3.3. The understanding of the detector behavior is crucial for the development of cryogenic detectors.
In the first approach, a cryogenic calorimeter consists of three components. The first is an absorber crystal with a heat capacity of C. A particle interacts with the crystal and deposits an energy ΔE. The second is a thermometer which is thermally connected to the crystal. The thermometer measures the temperature change which is given by:

$$\Delta T = \frac{\Delta E}{C} \tag{3.1}$$

The last component is the thermal link L, which connects the thermometer to a heat bath, which enables the absorber and thermometer to return to thermal equilibrium. A schematic drawing is shown in figure 3.1.
A more detailed approach is described in [123] and [77] and is briefly presented in the following. As already described, a particle interaction leads to an energy deposition E_0 in the absorber crystal. This interaction creates high-frequency optical phonons. These optical phonons decay very fast ($\mathcal{O}$(ns))

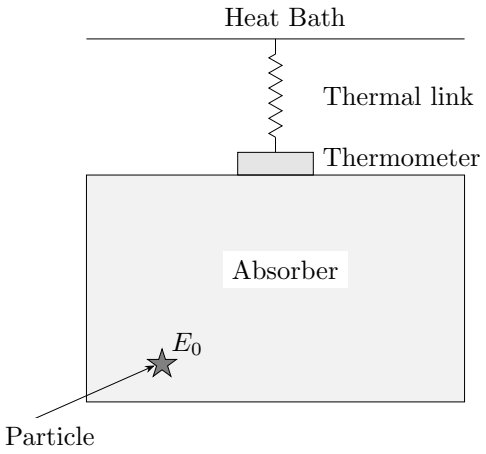

Figure 3.1: Schematic drawing of a cryogenic detector consisting of an absorber crystal equipped with a thermometer (TES) connected via a weak thermal link to a heat bath. A particle deposits energy E_0, which is read out by the TES.

into acoustic phonons with a frequency f_{Ph} half of the Debye frequency f_{Debye}.

$$f_{Ph} = \frac{f_{Debye}}{2} = \frac{k_B \Theta_{Debye}}{2h} \tag{3.2}$$

Θ_{Debye} is the material depend Debye temperature, k_B the Boltzmann constant and h the Planck constant. For lithium-fluoride the Debye temperature has a value of $\Theta_{Debye,LiF} = 734\,\mathrm{K}$ [124] and, therefore, 3.2 calculates to $f_{Ph} = 7.6\,\mathrm{THz}$. The energy of these phonons is given by $E_{Ph,nt} = hf_{Ph} = 21.5\,\mathrm{meV}$, which is high compared to the energy of thermal phonons with an energy of $E_{Ph,t} = k_b T \approx 1\,\mu\mathrm{eV}$ at $\approx 20\,\mathrm{mK}$. Those high-frequency phonons are called non-thermal phonons. The decay of non-thermal phonons is strongly frequency dependent with $\Gamma_d \propto f^5$ and, therefore, the decay is prompt within a few ms down to a frequency of $\sim 300\,\mathrm{GHz}$. The non-thermal phonons are reflected in the absorber and fill the crystal uniformly after $\sim 10\,\mu\mathrm{s}$. A fraction ϵ enters the thermometer and is absorbed by the electron system. The strong interaction of phonons with the electron system leads to fast thermalization and a temperature rise in the thermometer. The efficient absorption of non-thermal phonons results in a fast signal rise. This component can be described by a time-dependent power input $P_e(t)$. A second signal component results from the remaining fraction of $(1-\epsilon)$, leading to a power input $P_c(t)$

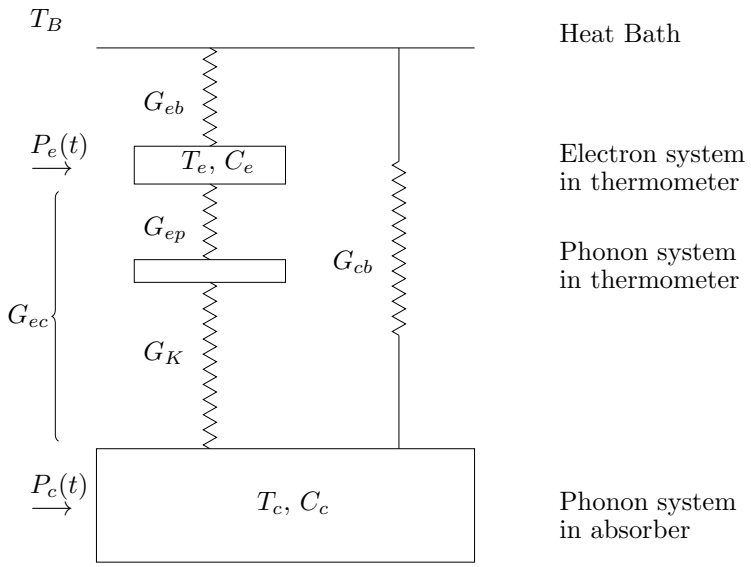

Figure 3.2: Schematic drawing of the thermal detector model developed in [123]. (T_c, C_c) and (T_e, C_e) describe the temperature and heat capacity of the crystal and the electron system of the thermometer, respectively. The temperature of the heat bath is given by T_b. The power input from non-thermal phonons is described by $P_e(t)$ and $P_c(t)$. The factors G_x are the thermal conductances in the system.

in the thermalised phonon system of the crystal::

$$P_e(t) = \Theta(t)\epsilon\frac{\Delta E}{\tau_n}e^{-t/\tau_n} \tag{3.3}$$

$$P_c(t) = \Theta(t)(1-\epsilon)\frac{\Delta E}{\tau_n}e^{-t/\tau_n} \tag{3.4}$$

where ΔE is the energy deposited by the initial particle, $\Theta(t)$ the step function and τ_n the time constant for the non-thermal phonon thermalisation. τ_n is a function of the time constants τ_e and τ_c for the thermalization in the thermometer and crystal, respectively:

$$\tau_n = \left(\frac{1}{\tau_e} + \frac{1}{\tau_c}\right)^{-1} \tag{3.5}$$

The temperature change of the thermometer and crystal can be directly connected to the power inputs described above. In addition, the power lost in the system must be considered. Figure 3.2 shows a schematic drawing of the

model described. There the crystal (C_c, T_c) and the thermometer (C_e, T_e) are thermally coupled via G_{ec} and linked to the heat bath (T_b) via G_{cb} and G_{eb}. This temperature change can be calculated with the following equations:

$$C_e \frac{dT_e}{dt} + (T_e - T_c)G_{ec} + (T_e - T_b)G_{eb} = P_e(t) \tag{3.6}$$

$$C_c \frac{dT_c}{dt} + (T_c - T_e)G_{ec} + (T_c - T_b)G_{eb} = P_c(t) \tag{3.7}$$

where $C_e \frac{dT_e}{dt}$ and $C_c \frac{dT_c}{dt}$ are the temperature change of the thermometer and the crystal, respectively. At $t = 0$, the inputs $P_e(t)$ and $P_c(t)$ are in thermal equilibrium with the bath. The two coupled differential equations above can be solved for $\Delta T_e(t) = T_e(t) - T_b$:

$$\Delta T_e(t) = \Theta(t)[A_n(e^{-t/\tau_n} - e^{-t/\tau_{in}}) + A_t(e^{-t/\tau_t} - e^{-t/\tau_n})] \tag{3.8}$$

with the non-thermal component $A_n(e^{-t/\tau_n} - e^{-t/\tau_{in}})$ and the thermal component $A_t(e^{-t/\tau_t} - e^{-t/\tau_n})$. A_n and A_t are the amplitudes of the two components. τ_n describes the time constant of the non-thermal component, τ_t and τ_{in} are the thermal relaxation time of the absorber crystal and the intrinsic relaxation time of the thermometer, respectively.
The ratio τ_{in/τ_n} is responsible for the sign of the non-thermal component A_n. Therefore, two different operation modes are found.
Calorimetric mode ($\tau_n \ll \tau_{in}$): The power input $P_e(t)$ is integrated for this mode, which means that the flow of phonons into the thermometer is faster than out of the thermometer. Thus, the total energy of the absorbed high-frequency phonons is measured. Since $A_n \approx -\epsilon\Delta E/C_E$, the given energy deposition and the heat capacity C_e determine the amplitude A_n. Here, τ_n describes the rise time for both components, whereas τ_t and τ_{in} describe the decay times of the thermal and non-thermal components, respectively.
Bolometric mode ($\tau_n \gg \tau_{in}$): The flow of phonons into the thermometer is slower than out of it. Therefore, the flux of non-thermal phonons is measured in this mode. Again the pulse height is proportional to the energy deposition in the crystal. τ_n is the decay time of the non-thermal and the rise time of the thermal component. τ_{in} and τ_t describe the non-thermal rise and thermal decay time, respectively.
For composite detectors, the model has to be modified by an additional phonon system. In composite detectors, the thermometer is built on a carrier substrate which is then glued to the absorber crystal. For an accurate description of the detector signal, the glued absorber interface component has to be considered and described according to [125][110]. The modified schematic drawing of the detector model is shown in figure 3.3. In comparison to figure 3.3 for a classic cryogenic calorimeter, the substrate carrying the thermo-

meter is added with a temperature T_S and heat capacity C_S. The coupling G_{Gl} to the crystal is done by a glue spot which does not contribute thermally to the system. Due to the added substrate, non-thermal phonons can either thermalize in the crystal contributing to the mentioned power input $P_c(t)$, or travel through the glue leading to a time-dependent power input $P_n(t)$ into the phonon system of the substrate. Those non-thermal phonons in the substrate can then be absorbed in the thermometer and induce the power input $P_e(t)$. In addition, they can be thermalized in the substrate (power input P_S) or reemitted into the absorber. The power input into the substrate leads to a temperature rise and introduces a slow component.

The signal analysis of such composite detectors can be done like classic

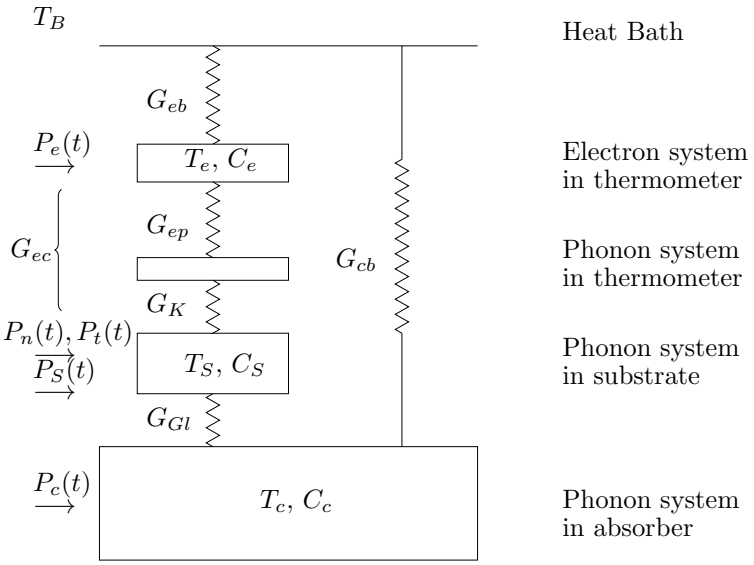

Figure 3.3: Schematic drawing of the thermal detector model developed in [123] for the composite detector design.

cryogenic calorimeters. In contrast, the energy input can not be treated as an instantaneous process since both power inputs $P_t(t)$ (thermal component) and $P_n(t)$ (non-thermal component) are time-dependent. The passing of non-thermal phonons depends on the thermalization rate and collection time, which is defined by the glue spot area relative to the absorber volume. It was found that the exact detector design and especially the TES-to-glue-area ratio strongly influence whether non-thermal phonons or both non-thermal and thermal phonons contribute significantly to the pulse signal.

3.2 LiF Cryogenic Detector as In-situ Neutron Monitoring System

An innovative neutron monitoring system was developed as the main focus of this research activity. The goal was to run a neutron-sensitive cryogenic detector inside the same experimental set-up employed for rare event searches with cryogenic detectors. This new detector concept allows for an in-situ efficient neutron tagging, enabling the identification and suppression of neutron-related background in Dark Matter experiments, but also in coherent elastic neutrino-nucleus scattering investigations.
The concept developed is based on the phonon-light technique, as explained before, which is the key technology employed by the CRESST Dark Matter experiment. An additional benefit of the phonon-light technique is the multi-target approach. This technique is not limited to a specific material as a target crystal but can use a wide choice of crystals. Therefore, it is possible to select the material by its physical properties, depending on the physics goal of the experiment. For the development of a neutron monitoring system, materials with high neutron-capture cross-sections had to be selected. The neutron energies that we are interested in studying are from 0.025 eV (thermal neutrons) up to a few MeV. These are the typical energies that lead to background contributions in direct DM searches, as neutrons produce the same type of signature of DM particles, namely low-energy nuclear recoils. To efficiently tag neutrons, neutron-capture processes have to be identified, which lead to a clear signature that lies in regions of the energy spectrum with a favorable signal-to-background ratio (e.g., far from multi-Compton energy regions). This is the case of energies above 2.6 MeV (^{208}Tl gamma line) and the so-called alpha region, which lies at energies of a few MeV.
Processes that fulfill the previously mentioned requirements are:

1. ^{3}He(n, p) ^{3}H: The neutron capture on ^{3}He leads to a proton and tritium, giving a clear signal with a Q-value of 764 keV [126]. The natural abundance of ^{3}He is very low with only 0.00014 % [127]. Therefore, to increase the amount of ^{3}He, it has to be enriched. But the main problem with ^{3}He is that it is impossible to bind it in a crystal lattice.

2. ^{10}Be(n, α) ^{7}Li: The neutron capture on ^{10}Be triggers an alpha decay of ^{11}Be into ^{7}Li. The Q-value of this decay is 2.31 keV in 93.7 % of all captures, leaving the ^{7}Li in its first excited state. In 6.3 % of all captures, the ^{7}Li is in its ground state, leading to a Q-value of 2.79 keV [128]. Also, here this would give a clear signal in the detector. But also ^{10}Be can not be used in a crystal since the only stable isotope is ^{9}Be with a natural abundance of almost 100 %.

3. ^{6}Li(n, ^{3}H) α: The neutron capture on ^{6}Li to an alpha and a triton has

a high energetic signal with a Q-value of 4.78 MeV.

$$n + {}^{6}Li \rightarrow \alpha + {}^{3}H + 4.78\,\text{MeV} \tag{3.9}$$

The alpha and the triton share the energy of 4.78 MeV. ^{6}Li has a relative high natural abundance of 1.9 %-7.8 % [129]. Therefore, an enrichment of the material is not necessary but possible. The disadvantage of using the neutron capture on ^{6}Li is the high energy of 4.78 MeV, which is in the energy range of alpha decays from natural decay chains. The cross-section for the lithium capture is high for a broad energy range, as shown in figure 3.4. A feature of the cross-section is the relative maximum at a neutron energy of 240 keV, which is in the following named resonance. Therefore, the capture process on ^{6}Li is a good detection channel for thermal neutrons up to MeV neutrons.

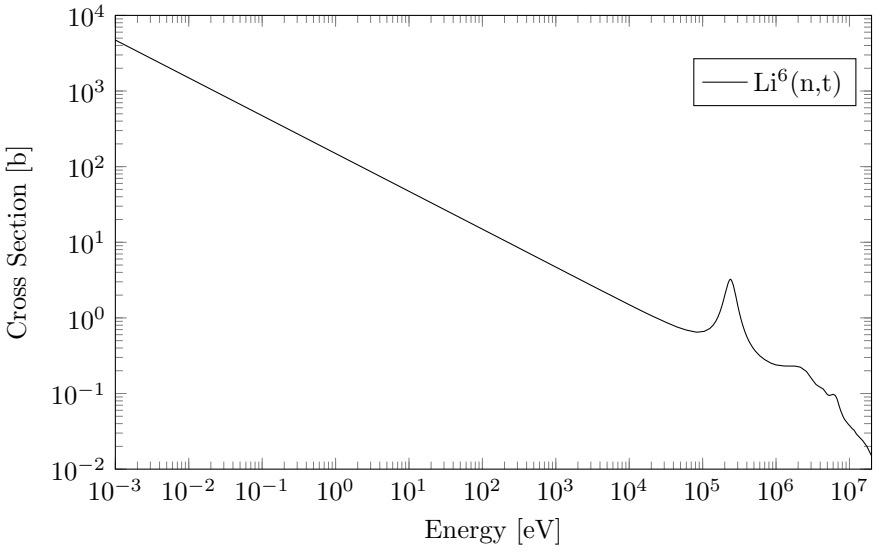

Figure 3.4: Cross section of the neutron capture process on ^{6}Li as a function of the initial neutron energy.

According to this list, lithium was chosen as a crystal component. There are many possibilities for lithium-containing crystals. There are LiF, $LiAlO_2$, Li_2MoO_4 or $Li_2Mg_2(MoO_4)_3$ to mention a few. In the framework of this thesis, a 100 g LiF (lithium-fluoride) crystal was selected as detector material for the following reasons:

1. Lithium fluoride is a scintillating material. Therefore, it is suited to be used as a target crystal with the phonon-light technique.

2. Since the crystal contains only lithium and fluoride, the amount of lithium is very high with $\sim 27\,\%$.

3. Lithium-fluoride is a commercially available product since it is used in optics applications because of its good optical properties.

However, the material also has some disadvantages. The light output is very low compared to other materials, e.g., $CaWO_4$. From the detector production point of view, it is a difficult material since the direct deposition of a thermometer was not possible, and the crystal was destroyed during the process.
Hence, the LiF crystal is equipped with a tungsten TES (Transition Edge

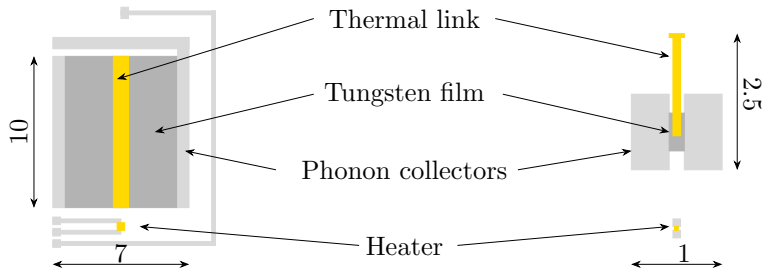

Figure 3.5: Schematic drawing of the TES used. *Left:* Phonon detector TES. *Right:* Light detector TES. Each TES consists of superconducting tungsten film equipped with two Al phonon collectors. A thermal link couples the TES weakly to a heat bath. Each TES is utilized with an ohmic heater to heat the TES in the transition.

Sensor), which was sputtered on a $CaWO_4$ substrate with a size of 20x10x1 mm^3. The size of the TES was chosen concerning the large crystal size and to cover a high energy range. The TES was produced in collaboration with the Max-Planck Institut für Physik (MPP) with a selected transition temperature of $> 30\,\mathrm{mK}$ [130]. A schematic drawing of the TES can be seen in figure 3.5. The TES consists of superconducting tungsten film equipped with two Al phonon collectors on two sites. A thermal link made from gold couples the TES weakly to a heat bath. To heat the TES in the transition, an ohmic heater is utilized. The $CaWO_4$ substrate is glued with a glue spot of the size of a pinhead ($\varnothing \sim 1\,\mathrm{mm}$) directly below the tungsten film to ensure a good phonon propagation from the crystal through the glue into the TES [1]. Silvered bronze clamps hold the crystal in a NOSV copper housing, similar in construction to a common CRESST II detector module. Figure 3.6 on the left shows a picture of the phonon detector.

[1] The used glue is the epoxy resin GP11 from Gössl und Pfaff [131].

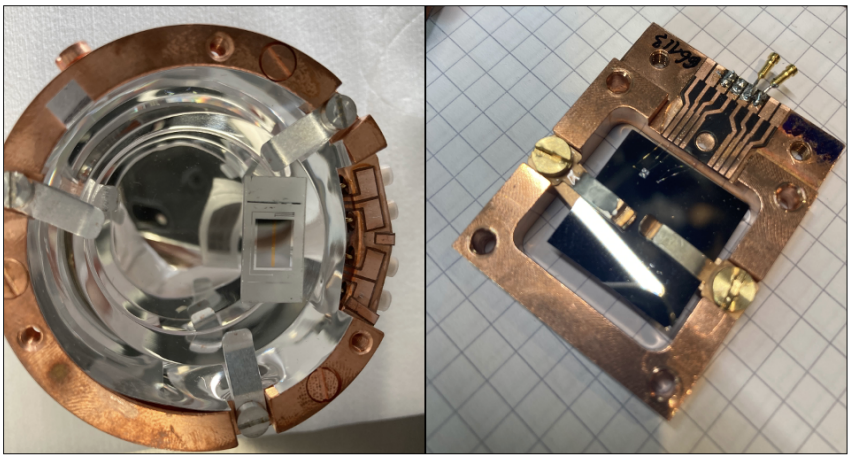

Figure 3.6: Phonon (left) and light (right) detector used in the measurement. Silvered bronze clamps hold both detectors. To increase the light detection efficiency, the module is completely enclosed in a reflecting and scintillating foil. The housing is made from NOSV copper to ensure a cooling down to mK temperatures.

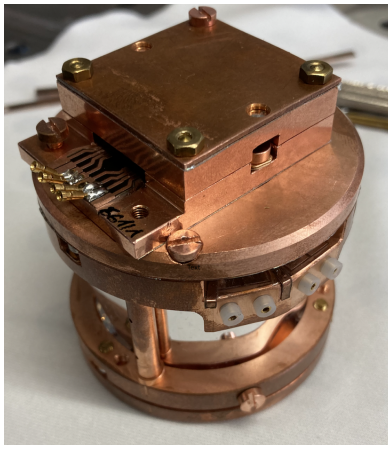

Figure 3.7: Closed detector module as it is mounted in the cryostat.

Besides the lithium-fluoride phonon detector, a silicon light detector was selected with a size of $20x20x0.5\,\mathrm{mm}^3$. There, a TES is directly deposited on the crystal. The TES here is much smaller than the one for the phonon detector to reduce the heat capacity for better performance (see figure 3.5 right). Also, the light detector was made in collaboration with the MPP. The detector was chosen to have a transition close to the one of the phonon detector to avoid cross-heating effects. The detector is held by silvered bronze clamps and is equipped with ^{55}Fe source for energy calibration. A picture of the light detector is shown in figure 3.6 on the right.
A picture of the detector module can be seen in figure 3.7. The light detector is screwed on a ring with a hole in the center with a diameter of $\sim 25\,\mathrm{mm}$, mounted on top of the crystal holder. A schematic drawing of the lithium-fluoride neutron monitor is shown in figure 3.8.

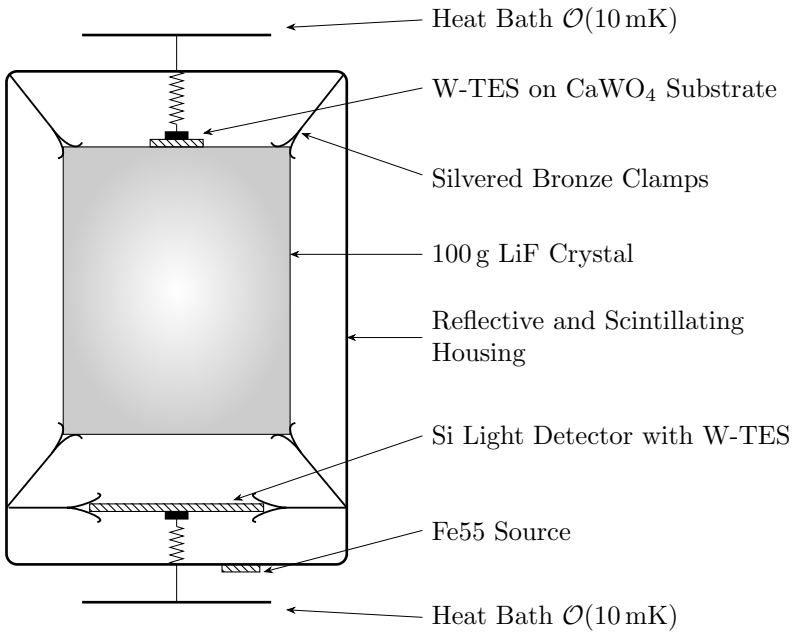

Figure 3.8: Schematic drawing of the lithium-fluoride neutron monitor. The module consists of two separated detectors, a 100 g lithium-fluoride phonon detector and a silicon light detector, each equipped with a tungsten TES coupled to a heat bath. Both detectors are held by silvered bronze clamps and are encapsulated in a reflecting and scintillating housing. The light detector is equipped with ^{55}Fe source for energy calibration.

3.3 Detector Operation

To operate cryogenic detectors, two main components are necessary. First, a thermal sensor in combination with a suited read-out circuit is needed. And second, a high-quality data acquisition is mandatory to guarantee stable measurements over a long time. In the following, these two aspects are described in more detail.

3.3.1 Thermal Sensor Read-out System

A particle interaction in the phonon or light detector leads to a slight temperature rise ($\mathcal{O}(\mu\mathrm{K})$). The temperature rise is measured by a transition edge sensor (TES), a superconducting thin film made of, e.g., tungsten, and temperature stabilized within the transition region between the normal- and the superconducting phase [132]. A schematic drawing of such a phase transition is shown in figure 3.9.

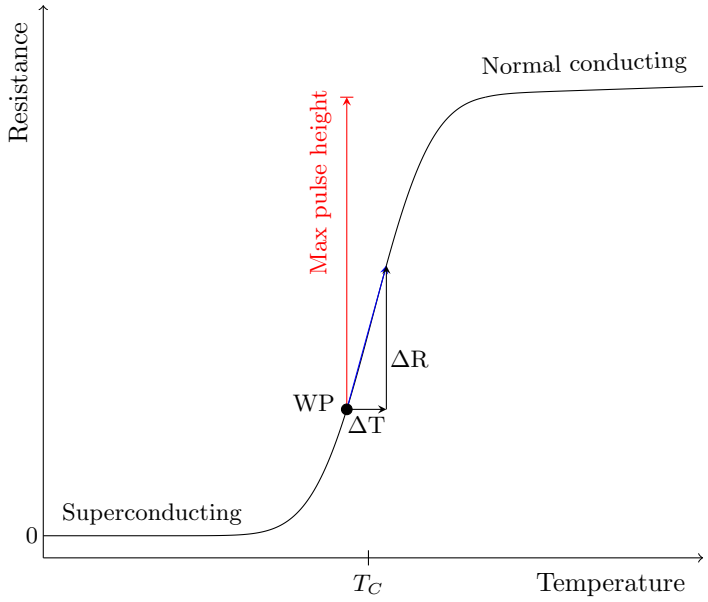

Figure 3.9: Schematic drawing of the phase transition between the normal conducting and superconducting phase of a Transition Edge Sensor (TES). The TES is stabilized at a certain temperature (working point WP) in the transition region. A small increase in temperature ΔT off the thin metal film on the TES leads to a measurable increase in the resistance ΔR of the TES. As indicated in red, the height of the pulses detected is limited since the transition has a finite level.

Due to the steep transition around the critical temperature T_C ($\mathcal{O}$(mK)), a small change of the temperature leads to a comparably large change of the

resistance in the transition ($\mathcal{O}(\mathrm{m}\Omega)$) which is measured. For the operation of the detector, the TES is stabilized at a defined temperature ("working point") to have a correct and linear energy calibration. As indicated in red in figure 3.9, the height of the pulses detected is limited since the transition has a finite level. Both TES, the one on the phonon detector and the one on the light detector is equipped with an electrically isolated heater. The heater consists of a thin gold stripe with aluminum pads on both ends to ensure easy and successful contact by bonding with an 33 μm aluminum bond wire. [2] The heater is used for two different reasons. First, to heat the TES into the transition of the tungsten film, and second, for sending pulses for an active working point stabilization and offline energy correction over time.

Due to the small resistance change of $\mathcal{O}(\mathrm{m}\Omega)$, the signal can not be meas-

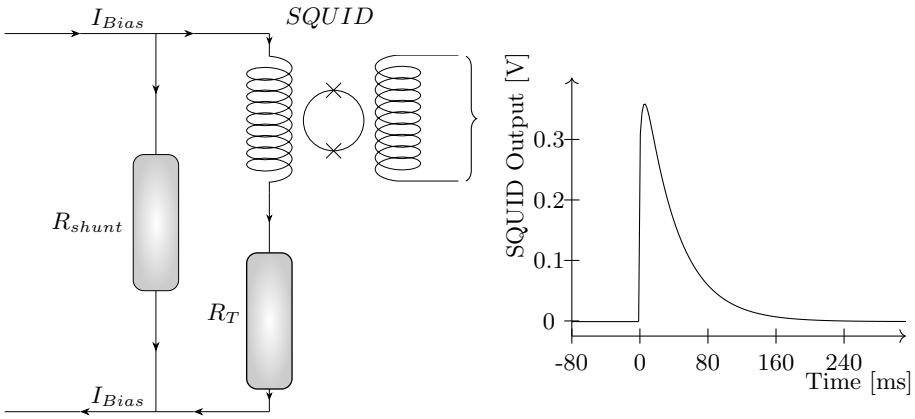

Figure 3.10: Detector read-out scheme. A constant bias current I_{Bias} is floating through the SQUID circuit and is splitting into the two branches (R_T + coil and R_{shunt}) following the Kirchhoff'schen rules (left side of the plot). A temperature change and, therefore, in the TES resistance R_T leads to a change of the current ratio in the two branches and a change of the magnetic field in the coil. This change is transferred into a voltage signal, resulting in a pulse as indicated on the right.

ured traditionally by, e.g., a four-point-measurement where the potential difference across the film is measured. A very elegant way to measure this small resistance change is the usage of so-called SQUIDs (Superconducting QUantum Interference Device), which are susceptible magnetometer devices [132][134][135]. A schematic read-out scheme utilizing SQUIDs is shown in figure 3.10.

The bias circuit contains two parallel branches. The first branch consists

[2] Wire bonder used: HB16 from tbt [133]. Gold and aluminum wires with a diameter of 25 μm and 33 μm, respectively.

of the SQUID coil and the TES with the temperature-dependent resistance $R_T(T)$. The second branch contains a reference resistance, also called shunt resistance R_S, with a resistance value ($\mathcal{O}(20\,\mathrm{m\Omega})$) lower than R_T, to have a weak negative electrothermal feedback in the circuit. Through the circuit, a constant bias current I_B is flowing. The current is split between the two parallel branches according to the Kirchhoff rules. The current I_{SQUID} flowing through the coil is given by

$$I_{SQUID} = \frac{I_B R_S}{R_S + R_T(T)} \tag{3.10}$$

For a small change of R_T, the SQUID current change ΔI_{SQUID} is proportional to the temperature change of the TES. For resistance changes of $\Delta R << R_T$, the current change flowing through the SQUID can be calculated in the following way.

$$\begin{aligned} \Delta I_{SQUID} &= \frac{dI_{SQUID}}{dR_T}\Delta R_T \\ &= \frac{I_B R_S}{\left(R_S + R_T(T)\right)^2}\Delta R_T \\ &= \frac{I_B R_S}{\left(R_S + R_T(T)\right)^2}\frac{dR_T}{dT}\Delta T \\ &\propto \Delta T \end{aligned} \tag{3.11}$$

Any current change in the thermometer branch of the circuit causes a difference in the bias current flowing through the input coil, which is then converted into a change in the magnetic flux. The SQUID acts as an amplifier that converts the magnetic flux change into a measurable voltage pulse $\mathcal{O}(\mathrm{V})$. The SQUID is operated in a flux-locked mode (FLL) with a separate feedback coil that keeps the flux through the loop constant. The output voltage of the SQUID electronics is then proportional to the feedback current I_F [132]. A typical signal recorded by a TES and measured by the SQUID system is shown in figure 3.10 (right).

3.3.2 Data Acquisition

For an accurate and stable long-term measurement, a high-quality data acquisition is mandatory. A schematic drawing of the data acquisition (DAQ) used for the measurements performed in this work is presented in figure 3.11. For a better overview, the four parts of the DAQ are highlighted in different colors. In black, the heater and pulser line is shown. In red is the bias line, in blue is the SQUID circuit, and violet is the muon veto line.
As already mentioned, the heater is used for two purposes. First, to heat the TES into the transition, a variable heater voltage between 0 V and 10 V is applied, controlled via the DAC output. The voltage output is then propor-

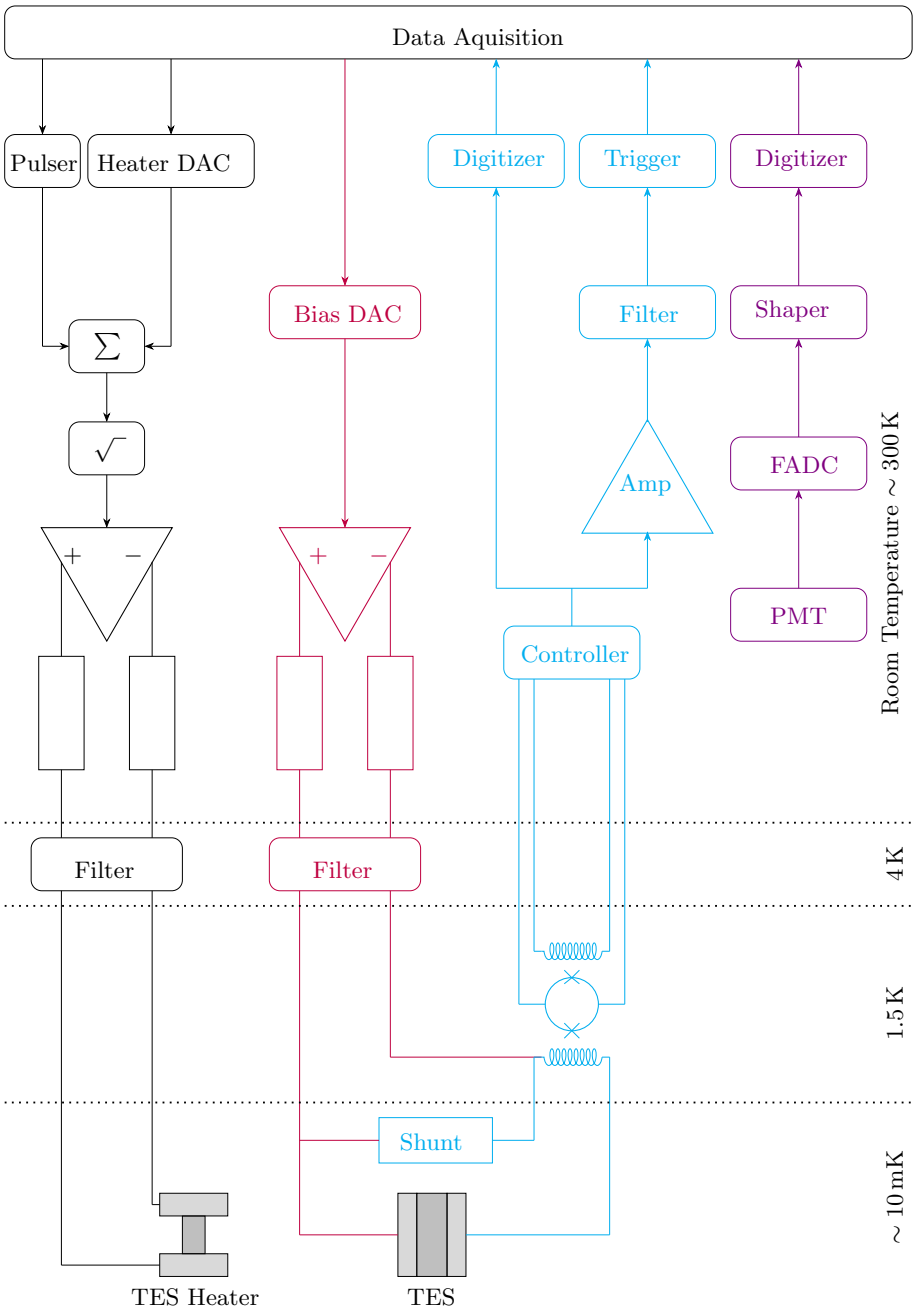

Figure 3.11: Schematic drawing of the data acquisition used for the measurements. In Black, the heater system stabilizes the detector at its working point and sends test pulses and control pulses for active detector stabilization and pulse height correction. The bias line is shown in red. In blue, the SQUID circuit with the shunt resistor is shown. In violet, the muon veto electronics is drawn.

tional to the heating current. And second for sending pulses generated by an arbitrary function generator with a defined shape, length, and amplitude. These pulses are used to stabilize the detector at its working point actively and to adjust the variable heater by a feedback loop (control pulses (CP)) and for an energy correction over time afterward (test pulses (TP)). Both the heater and pulser voltage signal are summed up and guided through a square rooter and a set of resistors, which defines the final current sent through the heater line. In the last step, the signal is guided through an H-filter at 4 K with a cut-off frequency of 16 kHz to reduce electrical noise.
As mentioned, control pulses are used to stabilize the detector at its working point. Those pulses are huge pulses that kick the TES out of its superconducting transition. The height of a control pulse depends on the working point as highlighted in red in figure 3.9. As those pulses are completely saturated, their pulse height can be used to measure the distance between the current working point to the normal conducting phase. For stabilization, the so-called set point is defined as a constant control pulse height. If the working point moves, the DAC heater voltage is automatically adjusted via a PID (Proportional-Integral-Derivative) controller to bring the TES back to its set point. If the control pulse is too high, the working point is too low in transition, and the DAC value has to be increased and vice versa.
Furthermore, test pulses can be injected, which imitate particle interactions in the detector. Test pulses are sent in several amplitudes to cover the complete dynamic range of the detector. These test pulses can be used to monitor detector gain drifts in the analysis and for energy calibration of the detector module (see section 4.7).
The bias chain (figure 3.11 red) provides a DAC voltage between 0 V and 10 V. This voltage is guided through a set of resistors, which defines the final current, and through an H-filter at 4 K with a cut-off frequency of 1.6 kHz.
For the muon veto (figure 3.11 purple), an FADC is used, which sends a logical trigger signal if one of the muon veto panels fires. The logical signal is very short compared to the time base of the data acquisition ($\mathcal{O}$(ns)). To optimize the timing accuracy, the signal is shaped to the length of 100 μs and recorded as a third channel.

3.3.3 Working Point Adjustment

To find a suitable working point, the shape of the transition for the phonon and light detector is measured. For this two steps with a step height of 0.1 V and 1 V corresponding too 100 nA and 1 μA are sent to the bias chain. The step height of the SQUID output is recorded as a function of the mixing chamber temperature. A dedicated heater on the mixing chamber is swept up and down. The measured SQUID output is shown in figure 3.12 as a function of temperature for the phonon detector (left) and the light detector (right). In black (blue), the SQUID response for an injected Step amplitude of

1 μA (100 nA) is shown. The critical temperature T_c for the lithium-fluoride detector is around 34 mK, the critical temperature T_c for the light detector at 33 mK.

For the working point selection, several test pulses and a control pulse are

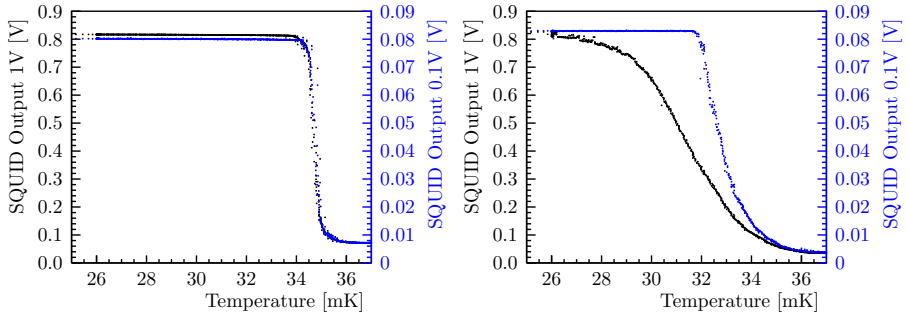

Figure 3.12: Transition Curves for the lithium-fluoride detector module. *Left*: Transition of the phonon detector TES. In black (blue), the SQUID response for an injected Step amplitude of 1 V (0.1 V), corresponding to a bias current of 1 μA (100 nA). The critical temperature T_c for this detector is around 34 mK. *Right:* Transition of the light detector TES. In black (blue), the SQUID response for an injected Step amplitude of 1 V (0.1 V), corresponding to a bias current of 1 μA (100 nA). The critical temperature T_c for this detector is at 33 mK.

sent to the detector. The heater is swept through the transition, and a curve is recorded for each test pulse. Figure 3.13 shows a heater sweep of the light detector. For a sweep, a constant bias current is selected (here 2 μA (black), 3 μA (green), 4 μA (red)) and test pulses with different amplitude are also sent in the height of the control pulse. The pulse height is then recorded as a function of the injected heater DAC. The working point is selected using the following criteria. On the one hand, the control pulse curve should be very steep to ensure a fast reaction of the PID loop to working point changes. On the other hand, the lowest test pulses should have a comparably high pulse height to maximize the detector's sensitivity. In addition, the test pulse curve should be flat to ensure the detector response for particle pulses does not change for small working point fluctuations. Since the transition temperatures are relatively high compared to the cryostat base temperature of 10 mK, the mixing chamber was heated to 26 mK to reduce the injected heating power of the TES heaters. According to the shown plot, one could select a bias current of 4 μA (red) with a DAC voltage of 0.17 V since the highest control pulse shows a steep slope around this value whereas the lowest test pulses are flat.

A suitable bias current for the phonon and light detector is found for values of 16 μA and 4 μA, respectively.

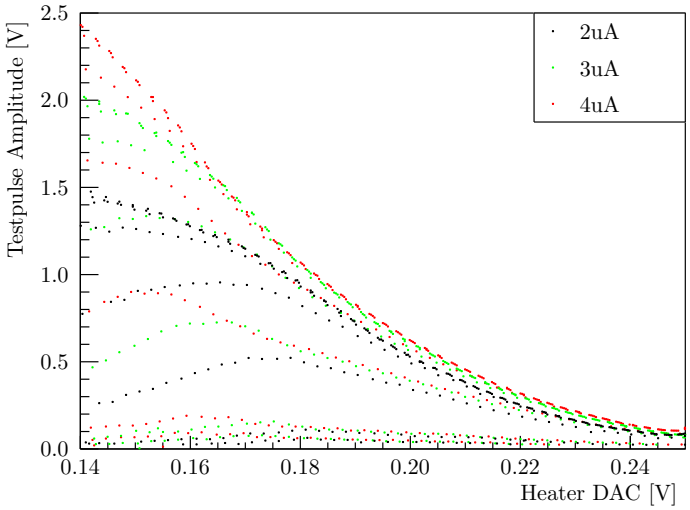

Figure 3.13: Sweep of the light detector channel. At a fixed bias current (here $2\,\mu$A (back), $3\,\mu$A (green), $4\,\mu$A (red)) test pulses are sent, and the pulse height is recorded as a function of the heater dac value injected by the heater on the TES.

Chapter 4

Analysis of the Cryogenic Neutron Measurement

The main software package used for the analysis presented is CAT (Cryogenic Analysis Tools) [90]. CAT is a ROOT [136] based analysis tool and can read, visualize and analyze binary data files produced by CRESST-like data acquisition systems. In addition, the software tool can easily be extended by user-defined macros and libraries. For fitting bands in the light yield plots in addition the software package Romeo [137] is used, which is based on the programming language Julia [138]. Both CAT and Romeo are part of the CRESST analysis framework and are developed in the collaboration.
In the previous chapter, the lithium-fluoride detector module was presented. The detector operation and the final working points for the measurements performed were shown. In the following section, the main ideas and concepts of the data analysis done for this measurement are presented. Starting from the description of the data in section 4.1, followed by the definition of the main parameters calculated for each pulse recorded in section 4.2. The sections 4.3-4.6 present the main analysis steps and analysis methods.

4.1 Data Description

For the measurement analyzed in this work, two dedicated measurement campaigns were performed. In run 22 the background was measured and an external calibration source was placed. An alpha calibration was done in run 23. The data-taking for run 22 and run 23 in the shallow underground laboratory in Garching took place from 02.09.2021 - 16.11.2021 and 25.12.2021 - 17.01.2022, respectively. For the measurements three different channels were used, the phonon and light channel and a muon veto channel. The channels were assigned to the following digitizer channels:

1. Digitizer channel 0: lithium-fluoride phonon detector

2. Digitizer channel 1: silicon light detector
3. Digitizer channel 2: muon veto

Since a high timing precision is necessary to evaluate the muon veto signal exactly a short time base of 5 μs was chosen for all channels. In addition, the pulses from the lithium-fluoride detector are very long ($\mathcal{O}$(500 ms)) because of the high detector mass of 100 g and the small glue spot between carrier and crystal. Therefore, the sampling length had to be set to 65536 samples. The

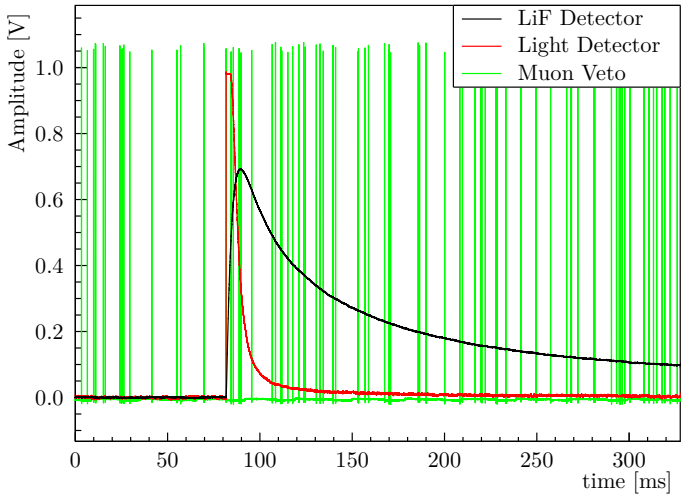

Figure 4.1: Typical event from the operation of the lithium-fluoride module. Each event has a timebase of 5 μs and a sampling length of 65536 samples. The total record window length was therefore 328 ms. The trigger is set to trigger on the phonon detector. When the lithium-fluoride detector triggers the light and muon veto channels are read out simultaneously. In black, a pulse of the lithium-fluoride detector is shown, and in red the light detector. The green pulses correspond to the muon veto trigger pulses.

total record window length was, therefore, 327.68 ms. The pre-trigger region is defined as the first quarter (81.92 ms) and contains baseline information. The post-trigger region is the remaining three quarters (245.76 ms) of the record window and defines the pulse information. The trigger is set to trigger on the phonon detector only when the signal in this channel extends a certain threshold (threshold trigger). The threshold is selected in a way that the signal-to-noise trigger ratio is more than 10:1 to minimize the dead time while the event is read out and is set to a value corresponding to $\sim$ 300 keV. Since the measurement is not designed to be a low threshold experiment but to measure events in the MeV range the trigger threshold could also be chosen higher. A trigger in the lithium-fluoride detector leads to the

simultaneous read-out of light and muon veto channels. Therefore, the light and muon veto channels are acquired independently of the presence of the signal in those channels. Figure 4.3 shows a typical event recorded during the data-taking campaign. In black, a pulse of the lithium-fluoride detector is shown, in red the scintillation light pulse is recorded by the light detector. The green pulses correspond to the muon veto trigger pulses. The muon veto triggers with a rate of $\sim 300\,\mathrm{Hz}$. Due to the high sampling rate and long record window of each pulse and the three different detectors recorded the amount of data taken is about 1.3 TB in total.

4.2 Main Pulse Parameters

To analyze the data recorded basic parameters are automatically determined for each triggered event.

BaseLineOffset: The SQUID output is a combination of a constant voltage and the voltage pulse on top of it. The constant baseline voltage has discrete levels up to the maximum limit of 10 V. The baseline offset is a parameter for each pulse where this voltage value is stored in [V].

BaseLineDiff: The baseline difference, also called right-left baseline, is the difference of the first 50 samples and the last 50 samples of the recorded pulse given in [V].

BaseLineRMS: The baseline RMS parameter is calculated from the Gaussian standard deviation of the first samples in the pre-trigger region. It, therefore, describes the noise conditions of a pulse. The parameter has the unit [V].

PulseHeight: The pulse height of a pulse is defined as the difference between the maximal sample in the record window and the baseline level, calculated from the pre-trigger region.

PeakPosition: This parameter is the channel or time where the pulse has its maximum. The parameter is stored in [ms] or channel number.

Onset: The onset of a pulse is given by the first sample with a value that reaches 10 % of the pulse height.

RiseTime: The rise time is defined as the time between the onset of a pulse and a signal level of 50 % of the pulse height parameter given in [ms].

DecayTime: The decay time is the time between the onset of a pulse and the sample where the pulse height decayed to $\frac{1}{e}$.

TimeStampCPU: The time stamp of the CPU parameter is the Central European Time where the pulse was recorded in unit seconds since January 1st, 1970 00:00:00 (Unix time).

4.3 Stability Cuts

As described above the detector module is actively stabilized. However, also with an active stabilization, it is possible to have periods where one of the two detectors is out of transition or has temporarily changed noise conditions. Furthermore, the muon veto channel provides an additional channel with possibly unstable working conditions. Therefore, not all data can be used for the analysis. Usually, control pulses are used for stability cuts. This cut works well if the total rate is low. However, when the rate is high, i.e. in above-ground measurements, control pulses often pile up with particle events, and a correct control pulse amplitude calculation is not possible. Hence, a different method was applied to select stable periods.

For a preselection of the data, a time cut on the muon veto is applied. Only

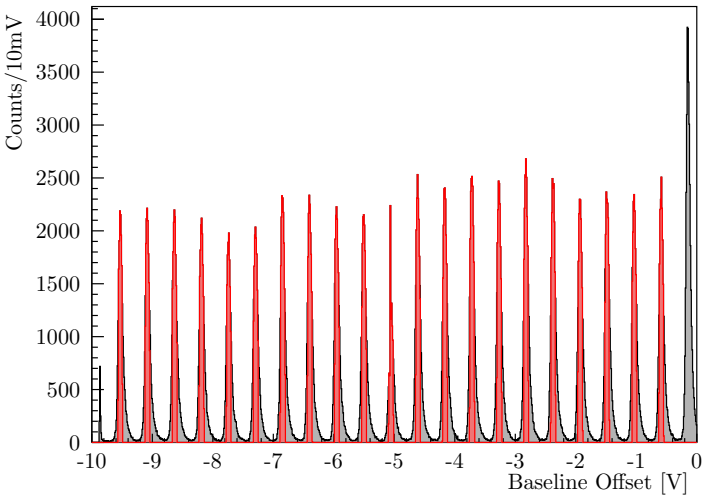

Figure 4.2: Stability cut on the baseline offset of the phonon channel. *Black:* Baseline offset of all particle pulses measured for the phonon channel. *Red:* Baseline offset of all pulses which survived the baseline offset stability cut. For the cut, a Gaussian function is fitted to each peak. Accepted are all events around the mean value with a maximum distance of a standard deviation. Since the offset values $-10\,\mathrm{V}$ and $0\,\mathrm{V}$ are treated as the same value the two peaks around $-10\,\mathrm{V}$ and $0\,\mathrm{V}$ are neglected.

periods are selected where the muon veto is working in stable conditions.
A second stability cut on the baseline offset of the phonon channel is applied. As already mentioned the baseline offset can take values between $-10\,\mathrm{V}$ and $0\,\mathrm{V}$. If the baseline of a pulse differs from these discrete values the working point has changed its value or the pulse contains unwanted features and can therefore be neglected. Figure 4.2 shows the baseline offset of all particle pulses measured for the phonon channel (black). For the cut, a Gaussian is fitted to each peak. Accepted are all events around the mean value with a maximum distance of a standard deviation (red). Since the offset values $-10\,\mathrm{V}$ and $0\,\mathrm{V}$ are treated as the same value the two peaks around $-10\,\mathrm{V}$ and $0\,\mathrm{V}$ are neglected.

4.4 Template Fit

As already previously mentioned the pulse height of a recorded pulse is a good estimator for the energy deposited in the detector for events with small energies that are recorded in the full linear region of the TES. However, the pulse height parameter can be influenced by two components, noise, and nonlinearity of the TES transition. A possible way for a more accurate pulse height estimation is the so-called template fit or also standard event fit (SEF). A valid assumption is that pulses from the same type of event (e.g. carrier events or bulk events) have the same pulse shape, where only the pulse size varies with the energy deposited. Thus, the energy can be estimated by fitting a template with a defined pulse shape to measured pulses.
In the first step, a standard event for each pulse shape is created while considering the thermal model of [123] which is described in section 3.2 in more detail. A number ($\mathcal{O}(100\,\text{events})$) of non-saturated events with the same energy range as from mono-energetic lines are summed up and averaged. These pulses have to be selected in a way that they don't have any artifacts to have a "noise-free" standard event. Due to the averaging process, the resulting template pulse describes the pulse shape of the respective event class with a reduced noise contribution compared to a single pulse. In the second step, the created template is fitted to all pulses. As shown in figure 4.3 an algorithm is searching for the minimum of the root mean square (RMS) between standard event samples (red) and pulse samples (black) by shifting the standard event ((1) and (2)) and scaling it to the right amplitude (3). The best-fit parameters are stored for each event with a set of new parameters. The most important are described in the following.

Amplitude: The amplitude, in the following called fitted amplitude, is the new estimated pulse height parameter.

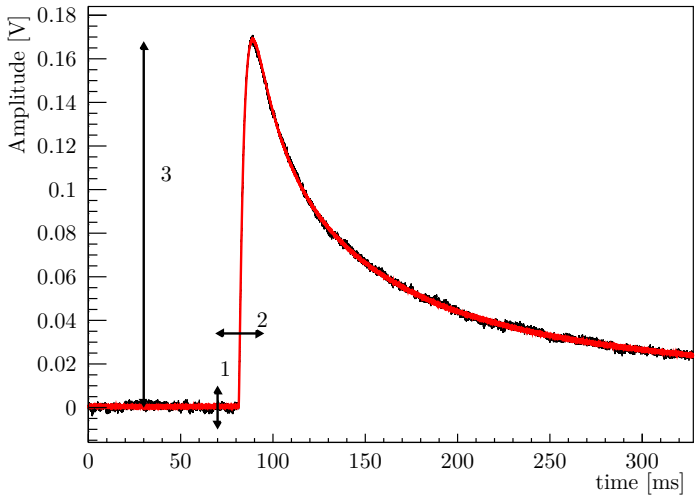

Figure 4.3: For each event class, a template or standard event with a typical pulse shape is created. This standard event fitted (red) to the recorded pulses (black) under optimization of baseline offset (1), time shift (2), and pulse amplitude (3).

RMS: The RMS of the fit is a measure of the deviation between fit and data.

OptimumShift: The optimum shift is the time the template onset had to be shifted to fit the data best. The value is given in [ms] .

NShifts: The same parameter as the optimum shift. The difference is that the value is given in [channel].

Truncated Template Fit

The standard event fit is a good energy estimator for pulses originating from the same type of event with the same pulse shape. This is not valid for saturated pulses where the pulse shape is changing drastically until the complete saturation of the thermometer is reached. To estimate the energy of saturated events a so-called truncated template fit (or truncated standard event fit) can be applied. For the truncated fit only a subset of the pulse is used, for which the detector response is still linear and the pulse amplitude can be reconstructed with limited uncertainties. This subset consists of samples above the baseline noise level but below a certain defined value, the so-called truncation limit, as it is indicated in figure 4.4 dotted line. In black the recorded pulse is shown. The part of the pulse above the truncation limit

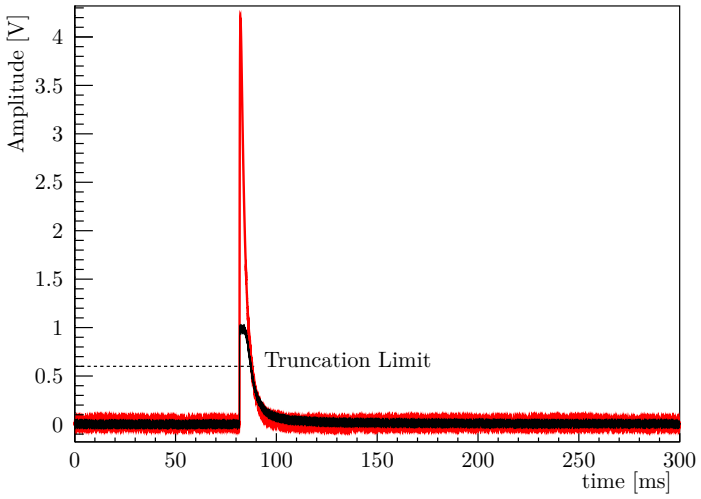

Figure 4.4: If the energy release of a particle interaction is too high, the pulse is saturating (black) since it is partially not in the linear region of the transition and cannot be described by the template anymore. To also be able to fit those pulses a truncated template fit is applied (red). A truncation limit is defined (dashed black line) where only pulse samples below this limit are used to extrapolate the original pulse shape and amplitude.

line is neglected for the fit and only the part of the pulse below is used. The truncation limit is usually determined by applying first a template fit. The lowest fitted amplitude where the fit RMS starts to increase is defined as the truncation limit. For the measurements performed the truncation limit is evaluated to be 0.6 V for both, phonon and light detector. The resulting fitted pulse is shown in figure 4.4, red pulse.

Used Templates

For this work, the template fit is applied both to particle pulses and test pulses in the phonon and light detector. The template for the particle pulses for the light detector is created from pulses of the ^{55}Mn K_α line, originating from the decay of ^{55}Fe calibration source. For the lithium-fluoride detector template pulses from the neutron capture peak at 4.78 MeV are used which are slightly below the truncation limit. Both templates are shown in figure 4.5. The templates for the test pulses are created from a non-saturated test pulse line for both, the phonon and light detector. For all templates, the set of pulses is cleaned using some basic data quality cuts to remove artifacts, pile-up effects, and pulses of different pulse heights.

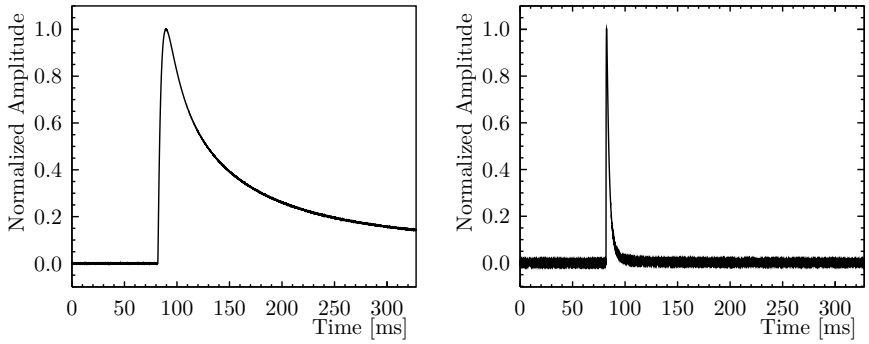

Figure 4.5: *Left:* Template or standard event (SE) for the phonon detector. For the SE creation pulses from the neutron capture line are used. *Right:* Template or standard event for the light detector. For the SE creation pulses from the ^{55}Mn K_α lien are used.

4.5 Optimum Filter

The standard event fit provides a reliable method for energy estimation but has limitations e.g. for very small pulses over a broad energy range with amplitudes in the order of the baseline resolution. For the lithium-fluoride module, the light detector has a significant number of these low energetic

pulses as the absolute scintillation light output of the lithium-fluoride is very low, as shown later in this chapter.
Another reconstruction method that is specialized in the reconstruction of such small pulses is the so-called Optimum Filter (OF) or Gatti-Manfredi filtering technique [139]. This filter assigns different weights to the thermal pulse frequencies and the ones of the noise, maximizing the signal-to-noise ratio. The filter transfer function $y(t)$ is built from the ideal signal shape $S(t)$ (standard event), the amplitude A and the noise power spectrum $n(t)$. $S(t)$ is estimated by averaging a large number of triggered pulses (so that stochastic noise superimposed to each pulse averages to zero) while $n(t)$ is computed by averaging the power spectra of randomly acquired waveforms where no pulse was found. The amplitude of a signal is estimated as the maximum of the filtered pulse. Therefore, $y(t)$ can be described via

$$y(t) = AS(t) + n(t). \tag{4.1}$$

The filter output can be described by a Fourier back transformation

$$y(t) = \frac{A}{2\pi} \int_{-\infty}^{\infty} \mathscr{H}(iw)\mathscr{S}(w)e^{i\omega t}d\omega \tag{4.2}$$

with $\mathscr{S}(\omega)$ the Fourier transformation of signal $S(t)$, the transfer function $\mathscr{H}(i\omega)$ and the amplitude A. In order to maximize the signal-to-noise (S/N) ratio at the time of measurement t_m [139] showed that this can be achieved by applying the transfer function $\mathscr{H}(\omega)$ (the optimum filter)

$$\mathscr{H}(i\omega) = \kappa \frac{\mathscr{S}^*(\omega)}{\mathscr{N}(\omega)} e^{-i\omega t_m} \tag{4.3}$$

where $\mathscr{N}(\omega)$ is the noise power spectrum (NPS) of $n(t)$ and κ a normalisation constant. A NPS is created by the sum of Fourier transformed baseline samples recorded constantly (so-called empty baselines) in the Fourier space. For more information about the optimum filter method, the reader is referred to [139][140].
Contrary to the standard event fit the optimum filter method can not be applied to saturated events. The use of the optimum filter leads to an improvement of the baseline resolution by a factor of 2-3 in comparison to the standard event fit and again to a new set of parameters.

Amplitude: The amplitude, in the following called filtered amplitude, is the new maximum sample value in the record after the filtering.

RMS: The filter RMS is the root mean squared difference of the filtered pulse and the filtered and scaled standard event.

4.6 Quality Cuts

For the analysis performed in this work, a list of basic quality cuts is applied to ensure the validity of the data. In the following, these cuts are explained in more detail.

The detector module consists of two detectors (see section 3.2). The lithium-

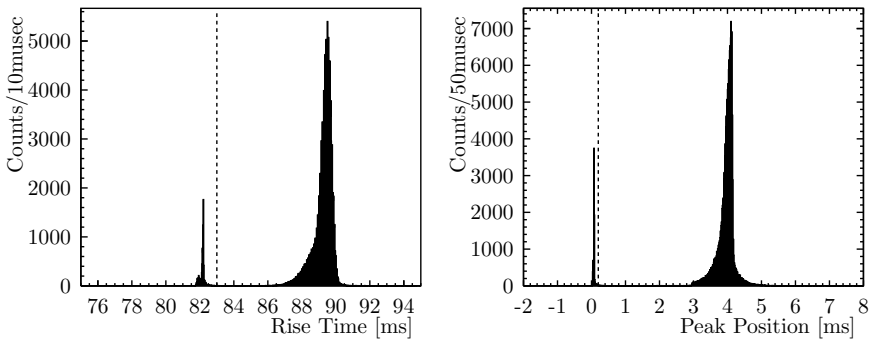

Figure 4.6: *Left:* Rise time of all lithium-fluoride events after stability cuts. All events on the left of the dotted line ($< 83\,\text{ms}$) are classified as carrier events and are neglected. *Right:* Peak position of all lithium-fluoride events after stability cuts. All events on the left of the dotted line ($< 0.2\,\text{ms}$) are classified as carrier events and are neglected.

fluoride phonon detector and a silicon light detector. Whereas the TES is directly evaporated on the silicon detector, a $CaWO_4$ carrier with a sputtered TES is glued on the lithium-fluoride detector. Therefore, in addition to the particle interaction events in the lithium-fluoride, so-called carrier events are recorded, events whose origin is an interaction in the $CaWO_4$ carrier. Due to the slower and reduced phonon propagation through the glue spot, lithium-fluoride pulses are much slower than events in the carrier. A sufficient way to distinguish carrier and lithium-fluoride events is a cut on the two parameters rise time and peak position, as they are described in section 4.2. Figure 4.6 shows the cuts made on the two parameters rise time (left) and peak position (right) of all pulses triggered by the phonon detector after stability cuts. All events on the left of the dotted line ($< 83\,\text{ms}$ and $< 0.2\,\text{ms}$, respectively) are classified as carrier events and are neglected.

A second cut is made on the baseline difference parameter (*BaseLineDiff*). Since the lithium-fluoride pulses are very long, this parameter must be treated carefully. Figure 4.7 shows the baseline difference of the phonon detector in the range between $-1\,\text{ms}$ and $1\,\text{ms}$. The dashed lines indicate the cut done on this parameter. All pulses within $-0.2\,\text{ms}$ and $0.5\,\text{ms}$ are accepted. Negative baseline differences are pulses with e.g. SQUID resets or flux-quantum-losses. Flux-quantum-losses are pulses where the rise of the pulse is so fast that

the SQUID can not follow and is losing flux quanta. Therefore, the pulse's baseline is lower at the end of the pulse than at the starting point. A SQUID reset happens after several FQLs where the electronics of the SQUID reaches its dynamic range and the SQUID resets to its starting point. The triggered signal is a sharp jump of the baseline in the order of 10 V. Those pulses can not be reconstructed and have to be neglected. The upper limit of 0.5 ms is chosen low enough to minimize the acceptance of pile-up pulses and large enough to not cut away part of the energy spectrum.

A third cut is made on the truncated fit RMS as a function of the fitted

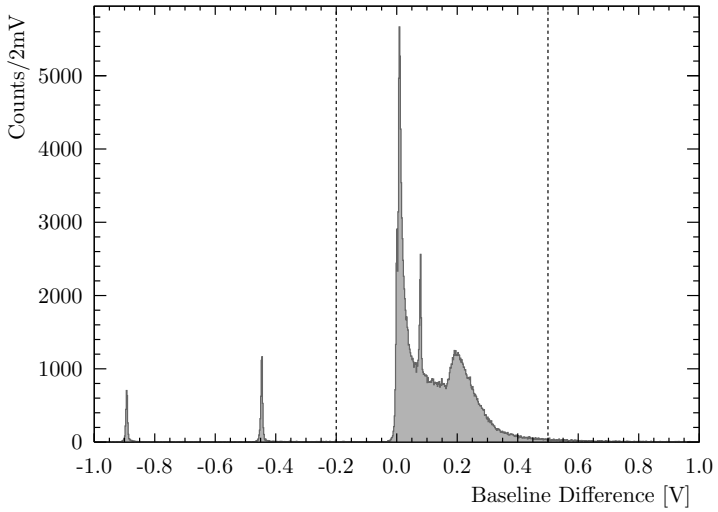

Figure 4.7: Histogram of the parameter baseline difference of the lithium-fluoride phonon detector data. Since the pulses are longer than the record window the baseline difference is growing with the amplitude. Negative baseline differences are pulses with flux-quantum-losses, pulses where the rise of the pulse is that fast that the SQUID can not follow and is losing flux quanta. Therefore, the pulse's baseline is lower at the end of the pulse than at the starting point. Those events are not included in the analysis.

amplitude of the phonon detector as it is shown in figure 4.8. Above the truncation limit of 0.6 V, which corresponds to an energy of > 5 MeV, the fit is not working perfectly anymore since the RMS value is rising moderately. The red line indicates the cut. The cut is chosen quite strictly for better data quality. The cut is energy-dependent, meaning that the cut strength depends on the pulse height of the event. This effect is included in the analysis via the calculated cut efficiency which is also energy-dependent.

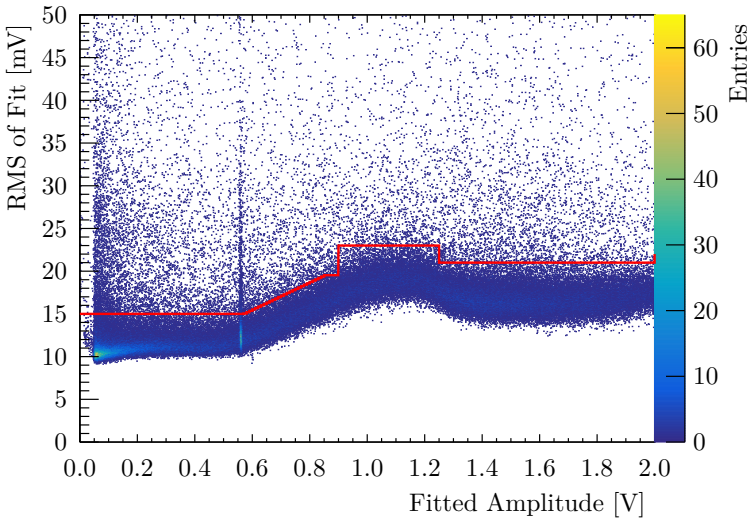

Figure 4.8: RMS of the truncated standard event fit as a function of the fitted amplitude for the phonon detector. The red line indicates the cut on the RMS parameter. Events above the red line are neglected.

4.7 Test Pulse Calibration

For a solid energy calibration, the time-dependent detector response must be considered.
For this, the heater pulses (test pulses) described in section 3.3.2 are used. Those heater pulses with various test pulse amplitudes are injected into the detector at regular time distances to correct the energy calibration because of time variations of the detector response due to instabilities over long periods. For the data presented in this work, 8 different amplitudes were injected, covering energies from 500 keV to 10 MeV. As mentioned the test pulses are used to monitor the detector response in the different energy ranges over time to apply a time-dependent energy correction. Figure 4.9 shows the fitted amplitude of injected heater pulses over time for a subset of the data taken in run22. For the reconstruction of the test pulse amplitude, a truncated standard event fit is applied. The gaps where no data is present are due to refills of the cryostat or neglected data files because of bad data quality. During the refill of the cryostat with liquid helium vibrations and temperature fluctuations are induced which leads to changes in the noise and working conditions of the detectors. Therefore, to ensure a constant high data quality a new file is started a few hours after the refill is finished.
Since each test pulse amplitude corresponds to a fixed injected energy they can be used to transfer the reconstructed amplitude into an injected energy over time in the whole energy range. Figure 4.10 shows the energy calibration

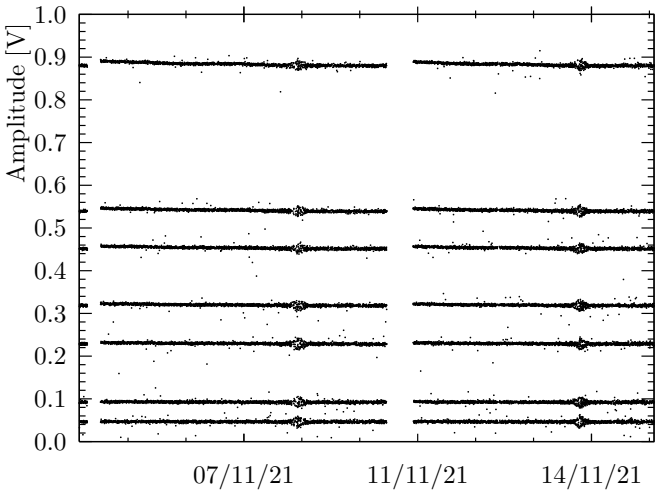

Figure 4.9: Fitted amplitude of injected heater pulses over time for a subset of the data taken in run 22. Heater pulses, so-called test pulses, with various known test pulse amplitudes are injected into the detector at regular time distances to correct the energy calibration because of time variations of the detector response due to instabilities over long periods. The gaps where no data is present are due to refills of the cryostat or neglected data files because of bad data quality.

with test pulses at a specific time. The black data points are the reconstructed amplitude from a truncated standard event fit as a function of the injected test pulse amplitudes (left scale) at a certain time and fitted with a spline function, also called the transfer function (red line). In blue the calibration peak of the neutron capture peak at 4.78 MeV is shown. It connects the fitted and injected scale with the energy scale (right). The fitted amplitude of a particle event can be converted into equivalent particle energy by evaluating the fit function at the fitted amplitude of the particle pulse occurring at this time (green). In between two test pulses of the same amplitude ($\mathcal{O}(1-2\,\mathrm{min})$) splines are fitted to the test pulses of each amplitude to guarantee a sufficient energy calibration between those two test pulses.

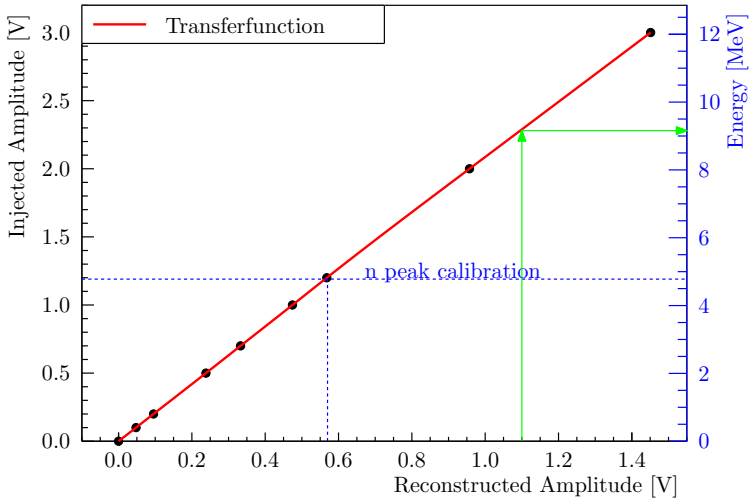

Figure 4.10: Energy calibration with test pulses at a specific time. The black data points are the reconstructed amplitude from a truncated standard event fit as a function of the injected test pulse amplitudes (left scale) at a certain time and fitted with a spline function, also called the transfer function (red line). In blue the calibration peak of the neutron capture peak at 4.78 MeV is shown. It connects the fitted and injected scale with the energy scale (right). The fitted amplitude of a particle event can be converted into equivalent particle energy by evaluating the fit function at the amplitude of the particle pulse occurring at this time (green).

4.8 Empty Baseline Simulation

An important step in the data analysis is the removal of the majority of events where their amplitude cannot be correctly estimated. However, each cut also removes valid pulses. All cuts applied are chosen in a way that invalid pulses are removed effectively but conservative enough to reduce the removal of valid pulses to a minimum. In addition, cuts can be energy-dependent due to e.g. the energy-dependent quality of the truncated standard event fit. Therefore, to calculate e.g. rates for the neutron background a cut efficiency has to be determined. The cut efficiency is the probability that a valid pulse survives the analysis chain and is not cut away.

A method to calculate the cut efficiency is a so-called empty baseline simu-

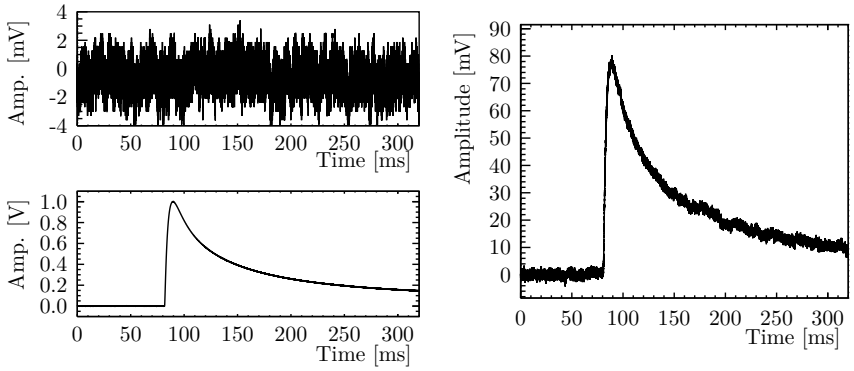

Figure 4.11: Creation of simulated pulses. During data taking so-called empty baselines are recorded (top left), events without a pulse, and just the baseline. The template pulse (bottom left) is scaled to different amplitudes and therefore energies and added to the empty baselines (right). The simulated events are then guided through the analysis chain as applied to the real data. With this method, an energy-dependent survival probability can be determined.

lation where pulses are simulated on a set of empty baselines over the energy range of interest between 2.5 MeV and 6.5 MeV. Figure 4.11 shows the creation of simulated pulses. During data taking empty baselines are recorded (top left). The template pulse (bottom left) is scaled to different amplitudes (energies) and added to the empty baselines (right). The simulated events are then guided through the same analysis chain as applied to the real data to determine an energy-dependent survival probability. Since the number of empty baselines is limited but a high statistic is needed various fixed pulse heights are simulated on the same empty baseline list. In figure 4.12 the energy-dependent cut efficiency for run22 is shown. The cut efficiency is relatively low ($\mathcal{O}(40\,\%)$) since stability cuts are included. The cut efficiency is constant for energies smaller 5 MeV which hints that the cuts applied are

energy independent. For energies larger 5 MeV the cut efficiency is rising linearly. This behavior is originating from the RMS cut applied as described in section 4.6. Due to the cut on the RMS parameter, more events are surviving the analysis chain which ends in a higher surviving probability. Since no deeper analysis is done for the light channel the cut efficiency is only calculated for the phonon channel.

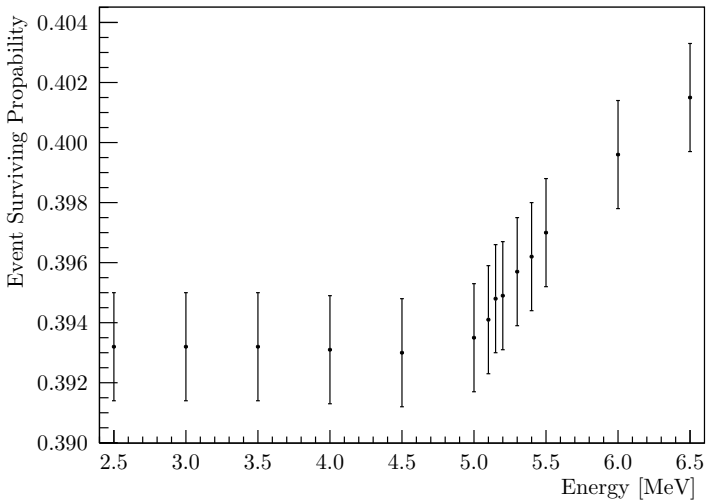

Figure 4.12: Energy-dependent cut efficiency of the background run run22. For the determination, a baseline simulation is performed.

4.9 Light Yield Band Fits

For fitting the electron/gamma band, alpha band, and the alpha/tritium band (compare section 1.5.3) a band fit tool is used as it is described in [137][87]. This program called Romeo is based on the programming language Julia.
For the electron/gamma band, the mean light yield can be written as a function of the energy via

$$L_e(E) = L_0 E + L_1 E^2 \tag{4.4}$$

with the two fitting parameters L_0 and L_1. Often at lower energies the so-called non-proportionality effect reduces the light yield and bends the bands towards lower light yields. This can be described by an exponentially

decaying factor that changes the above-shown equation to

$$L_e(E) = (L_0 E + L_1 E^2)\left[1 - f_e exp\left(-\frac{E}{\lambda_e}\right)\right] \tag{4.5}$$

where λ_e and f_e are two additional material-dependent fitting parameters. The mean light yield of the alpha band as well as the alpha/tritium band can be calculated via

$$L_\alpha(E) = L_e(E) \times Q_\alpha(E) \tag{4.6}$$

where $L_e(E)$ is the described light yield for the electron/gamma band and the energy-dependent quenching factor $Q_\alpha(E)$. This quenching factor includes three additional fitting parameters A_0, A_1 and A_2 and can be calculated with

$$Q_\alpha(E) = \frac{A_0}{1 - A_1 exp\left(-\frac{E}{A_2}\right)} \tag{4.7}$$

The mean light yield for alphas is finally summed up in the following equation:

$$L_\alpha(E) = (L_0 E + L_1 E^2) \cdot QF_\alpha \cdot \left[1 + exp\left(-\frac{E}{\lambda_\alpha}\right)\right] \tag{4.8}$$

To determine the width of the bands one can use

$$\sigma_x(E) = \sqrt{\sigma_L(L_x(E)) + \frac{dL_x}{dE}\sigma_P(E)} \tag{4.9}$$

with

$$\sigma_L(L) = \sqrt{\sigma_{L,0}^2 + S_1 L + S_2 L^2} \tag{4.10}$$

and

$$\sigma_P(L) = \sqrt{\sigma_{P,1}^2 (E^2 - E_{thr}^2)} \tag{4.11}$$

which describe the resolution of light and phonon detector respectively. The two parameters $\sigma_{L,0}$ and $\sigma_{P,0}$ are the determined baseline resolutions of the light and phonon channels, whereas $\sigma_{P,1}$, S_1 and S_2 are additional fitting parameters.

Chapter 5

Results of the Cryogenic Neutron Measurement

In the following, the main results of the measurement presented in chapter 4 are shown. First, the detector module calibration is described. Then, the UGL muon veto is characterized, and a new timing parameter is presented to tag muon-induced events, e.g., neutrons. Afterward, the first neutron spectrum is calculated.

5.1 Detector Module Calibration

To reconstruct the energy scale correctly, an energy calibration is necessary. For this purpose, different radioactive sources are used for this measurement. To calibrate the light detector, a weak ^{55}Fe source ($\mathcal{O}$(mBq)) is used, which is directly mounted on the module. For the calibration of the phonon detector, two different sources irradiated the crystal. A ^{228}Th gamma source was temporally placed between outer lead shielding and dewer. In an additional calibration run (run 23), a ^{147}Sm alpha source was placed inside the module, facing the crystal side. In the following, the calibration is presented in more detail.

5.1.1 Silicon Light Detector Calibration

As described in section 1.4, the energy information about a particle interaction in the target is mainly given by the energy deposited in the phonon detector. Therefore, an exact energy calibration is crucial. On the other hand, the light channel is mainly used to discriminate between the different particle interactions, and calibration is not mandatory. However, a direct calibration of the light detector can be used to evaluate the light output of lithium-fluoride.
For this a weak ^{55}Fe gamma source (activity of $\mathcal{O}$(mBq)) is used. The source

can not be placed outside the cryostat since the typical Mn gamma lines are too low energetic (6 keV) and are stopped by the cryostat shielding.

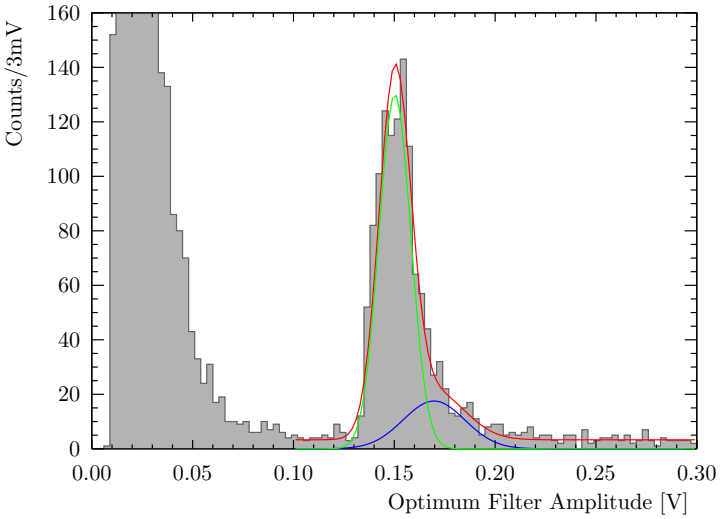

Figure 5.1: Light detector calibration with an ^{55}Fe source. Shown is a histogram of the reconstructed amplitude with an optimum filter, as described before. The optimum filter used is the same as in the background measurement. Used are events occurring in the light detector. Therefore, the trigger is set to trigger on the light channel instead of the phonon channel, and the pulse height of the phonon detector is limited to be smaller than 0.1 V. Due to the decay chain of ^{55}Fe the ^{55}Mn K_α and K_β with energies of 5.9 keV and 6.4 keV, respectively, are detected [127]. In green and blue, the fits of the two Gaussian of the K_α and K_β, and in red, the combined fit of two Gaussian and a constant background are drawn.

The standard triggering is done on the phonon channel. Since ^{55}Fe events are not a coincident event class between phonon and light channel and because of the comparable low energy, which can only be detected in the light channel, the triggering scheme is changed to trigger on the light channel only. An optimum filter was used to evaluate the amplitude of the pulses (see section 4). The reconstructed pulse height spectrum is shown in figure 5.1.
The source is mounted in a way to only irradiates the light detector. There is no direct line of sight to the phonon detector. Therefore, no or only random coincident pulses are expected to occur in the phonon detector. The amplitude in the phonon detector is limited to a value smaller than 0.1 V. The spectrum shows a rising background for low energies, which are related to gamma and electron-induced events originating from, e.g., the surrounding material. In addition a double structure due to the ^{55}Mn K_α and K_β lines with energies of 5.9 keV and 6.4 keV, respectively, are visible [127]. Applying a double Gaussian fit a 1σ resolution of 310 eV at 5.9 keV is calculated.

5.1.2 Lithium Fluoride Phonon Detector Calibration

For the calibration of the lithium-fluoride detector, three different approaches are used.

1. Calibration with the 4.78 MeV neutron capture line
2. Calibration with an external ^{228}Th source
3. Calibration with an internal ^{147}Sm alpha source

The following describes the lithium-fluoride phonon detector calibration in more detail.

Neutron Capture Peak Calibration

For the calibration of the lithium-fluoride crystal, an intuitive calibration line is the 4.78 MeV neutron capture line. This line is very well suited because of the known kinematics of the capture process and its high cross-section at 4.78 MeV. It is also an intrinsic calibration source, and therefore, the total energy is released in the crystal. The only exception is capture interactions

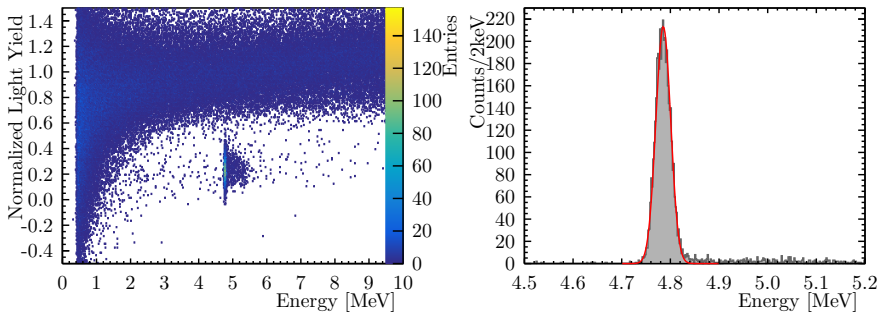

Figure 5.2: *Left:* Light yield plot of the complete background run after all cuts. The light yield is normalized to one for electron/gamma events in the energy range between 4 MeV and 6 MeV. The neutron capture events with a light yield of around 0.2 can clearly be distinguished from electron/gamma events. *Right:* Lithium-fluoride energy spectrum, calibrated with the neutron capture peak at 4.78 MeV. Shown are only events between 4.5 MeV and 5.2 MeV and related to a neutron capture. A Gaussian fit is applied to the data. A 1σ resolution of 15 keV at 4.78 MeV is calculated.

very close to the crystal's surface where the mean free path of the decay products is large enough to leave the crystal and carry away a finite amount of energy. The α and ^{3}H ions share the Q-value Energy of 4.78 MeV with a ratio

of $E_\alpha = 2.05\,\text{MeV}$ and $E_{^3\text{H}} = 2.73\,\text{MeV}$. The corresponding path length of those particles inside the LiF is given by $6.31\,\mu\text{m}$ and $33.05\,\mu\text{m}$, respectively [141]. This leads to a maximum volume of $2.07\,\text{mm}^3$ in comparison to the total volume of $37.7\,\text{cm}^3$ where an α or ^{3}H particle can potentially leave the crystal and carry away energy.
The right plot in figure 5.2 shows the energy spectrum of the lithium-fluoride phonon detector in the range between 4.5 MeV and 5.5 MeV, calibrated on the neutron capture peak at 4.78 MeV. Only neutron capture events are selected via a light yield cut for the plot. Figure 5.2 left shows the normalized light yield of the complete background run after all cuts. The light yield is normalized to one for electron/gamma events at $5 \pm 1\,\text{MeV}$. The neutron capture events with a light yield of around 0.2 can clearly be distinguished from electron/gamma events. The peak is fitted with a Gaussian (red) leading to a 1σ resolution of 15 keV at the captured energy.

^{228}Th Gamma Calibration

An external ^{228}Th gamma source is used to validate the energy scale. The

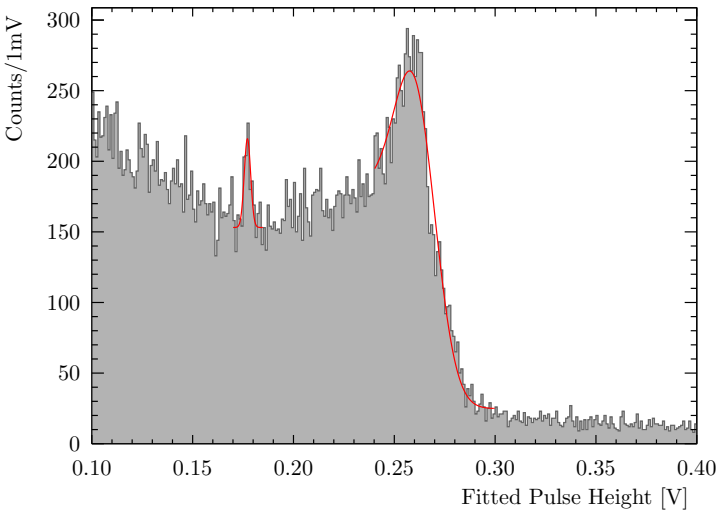

Figure 5.3: Pulse height spectrum of an external ^{228}Th calibration source measured with the lithium-fluoride phonon detector. The source is placed between lead shielding and dewer. A ^{228}Th source emits the highest natural gamma energy of 2614.53 keV, originating from the β decay of ^{208}Tl to ^{208}Pb [127]. These high energetic gamma events are not seen in the detector but its Compton edge with an energy of 2381.78 keV as well as the double escape line at an energy of 1592.53 keV. Both, the double escape line and Compton edge are fitted and drawn in red.

source is placed temporarily between lead shielding and dewer at the height of the detector module. Figure 5.3 shows the pulse height spectrum of the calibration source measured with the lithium-fluoride phonon detector. ^{228}Th sources emit the highest natural gamma energy of $E_{Tl} = 2614.53\,\text{keV}$, originating from the β decay of ^{208}Tl to ^{208}Pb [127]. These high energetic gamma events are not seen in the detector (the total energy of the photoelectrons can not be contained) but its Compton edge with an energy of $E_{CE} = 2381.78\,\text{keV}$. In addition the double escape line of ^{208}Tl at an energy of $E_{DE} = E_{Tl} - 2 \cdot 511\,\text{keV} = 1592.53\,\text{keV}$ can clearly be seen. Mathematically the Compton edge fit function $R(E)$ can be described by [142]

$$R(E) = \alpha \cdot e^{\frac{-(E-E_C)^2}{2\cdot\sigma^2}} + \beta \cdot erfc\left(\frac{E - E_C}{\sqrt{2}\cdot\sigma}\right) + const \tag{5.1}$$

with the Compton edge energy E_C, the standard deviation σ, α and β two scaling parameters and the error function.

Since a calibration on a Compton edge often has large uncertainties, the

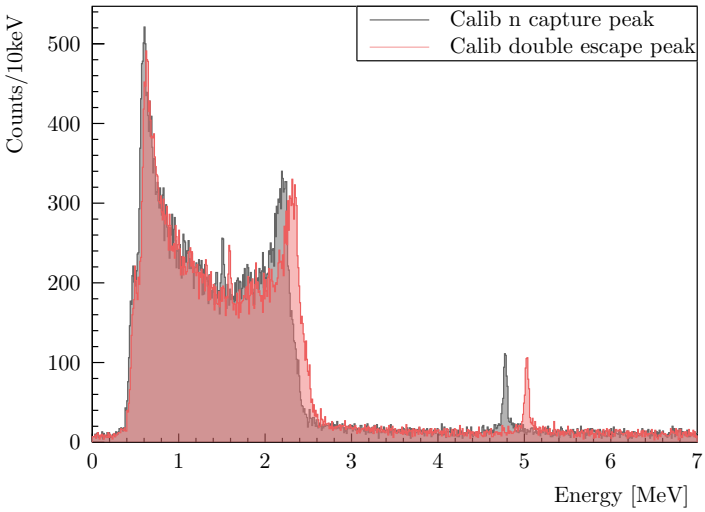

Figure 5.4: Comparison between two different energy calibrations. In grey (red), the energy spectrum with a calibration with the neutron peak (double escape peak of ^{208}Tl). There is a clear discrepancy of both spectra of 270 keV (5.6 %). An accurate energy calibration with ^{208}Th is feasible only for the electron/gamma band but not for the α+^{3}H band.

spectrum is calibrated with the double escape line of ^{208}Tl and compared to the neutron peak calibrated spectrum. The double escape peak is fitted with a Gaussian with a mean at 0.177 V and a σ deviation of 0.002 V. A fit on the Compton edge with equation 5.1 shows the position of the Compton

edge at 0.262 V with a σ deviation of 0.011 V. With an energy calibration on the double escape peak, the position of the Compton edge is given by $E_{CE,fit} = 2357.30 \pm 102.49$ keV, which is in good agreement with the literature value of 2381.78 keV.

In the next step, the spectrum is calibrated with the neutron capture peak,

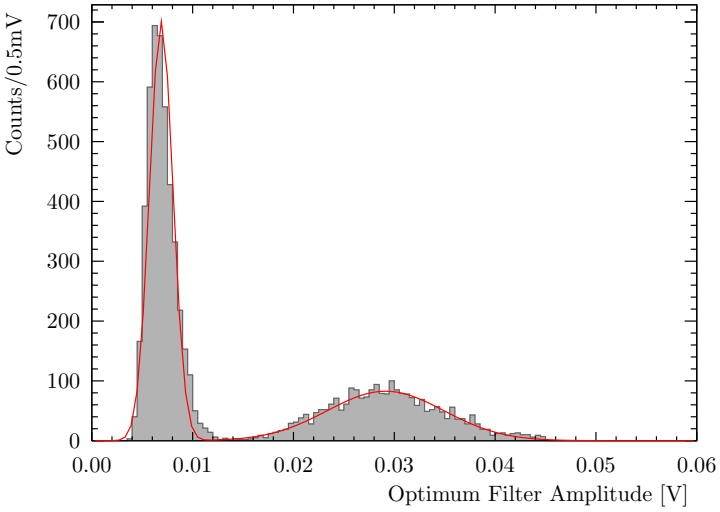

Figure 5.5: Measured pulse height spectrum for the light channel for events detected in the phonon channel with energies between 4.7 MeV and 5.2 MeV. The left peak belongs to the neutron capture peak, and the right peak to the electron gamma band.

and both spectra are compared. This comparison is shown in figure 5.4. In grey, the energy spectrum with the neutron peak calibration is drawn. In red, the energy spectrum is calibrated with the double escape line of ^{208}Tl. There is a clear discrepancy of both spectra of 270 keV (5.6 %) at the energy of the neutron capture peak of 4.78 MeV. This effect has been observed in other detectors of this kind [143]. A possible explanation for this discrepancy is the overestimation of the phonon energy, the so-called phonon-anti quenching. The deposition of a total energy E_{tot} is converted into phonons E_{Ph} and scintillation light E_L, which is detected with the light detector. Since the number of light changes with the type of particle interaction, gamma events have a higher fraction of the total energy converted into light than, e.g., α events. Therefore, for α events, a higher fraction in the phonon channel is measured, meaning that for gamma and α events with the same measured pulse height in the phonon detector, less energy has to be deposited for α events since less energy is going into light [143][144]. However, the light output of lithium-fluoride is very small. Figure 5.5 shows the optimum filter amplitude

for the light channel for events detected in the phonon channel with energies between 4.7 MeV and 5.2 MeV. The left peak belongs to the neutron capture peak, and the right peak to the electron gamma band, both fitted with a Gaussian. With the energy calibration of the light detector (see section 5.1.1), events in the electron/gamma-band with a phonon energy of 4.78 MeV emit 1.14 ± 0.24 keV (light output 0.02 %) off scintillation light. For events in the neutron capture peak, the energy emitted is 0.28 ± 0.05 keV (light output 0.006 %) only. An energy discrepancy of ~ 270 keV can, therefore, not be explained by the discrepancy of scintillation light emitted by different types of particle interactions. Other mechanisms might lead to long-living states that act as energy traps (with half-lives much longer than the length of a LiF thermal pulse), leading to such a large discrepancy.
An accurate energy calibration with ^{208}Tl is feasible only for the electron/gamma band but not for the α+^{3}H band. Therefore, a dedicated α calibration is needed and described in the next section.

^{147}Sm Alpha Calibration

Since a calibration with a gamma source is not suited for the calibration of the α-^{3}H band, a dedicated run (run 23) with an ^{147}Sm source is done. The detector operation and working point are unchanged from the one described in section 3.3. Also, the setup was left untouched, meaning the same SQUID channels and heater/bias channels are used, and thermal coupling is the same as in the background measurement described before. Only a 2x2 cm^2 rectangle is cut out from the reflecting foil on the cylinder barrel of the detector module to mount the ^{147}Sm source. The source is faced the side of the lithium-fluoride crystal. There is no line of sight to the TES of the crystal or the light detector. Figure 5.6 shows the decay scheme of ^{147}Sm to ^{143}Nd under the emission of an α particle with an Q-value energy of 2310 keV. The half-life of this process is $1.06 \cdot 10^{11}$ y [127].
The energy spectrum of the ^{147}Sm α measurement run is shown in figure 5.7. The neutron capture peak at 4.78 MeV is used to calibrate the spectrum. The α spectrum is not a single line but a continuous spectrum with an edge as the α particle travels through the source, leaving the material to reach the detector and releasing part of the energy. In addition, a clear signal at the energy of the neutron capture peak with 4.78 MeV can be seen.
A light yield cut is used to reduce the electron/gamma background in the spectrum. Figure 5.8 shows a normalized light yield plot. For the light yield, an optimum filter is applied for the light channel, whereas a truncated standard event fit is used for the phonon signal. The light yield is again normalized to 1 for electron/gamma events in the energy range between 4 MeV and 6 MeV. To clearly distinguish α events from electron/gamma events, a relatively strict cut at a normalized light yield of 0.5 is chosen, indicated by the red line in figure 5.8. The plot shows that a clear separation is possible

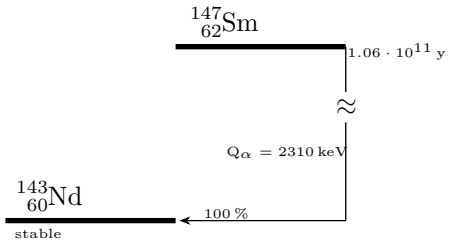

Figure 5.6: Decay scheme of ^{147}Sm to ^{143}Nd under the emission of an α particle with an Q-value energy of 2310 keV. The half-life of this process is given by $1.06 \cdot 10^{11}$ y [127].

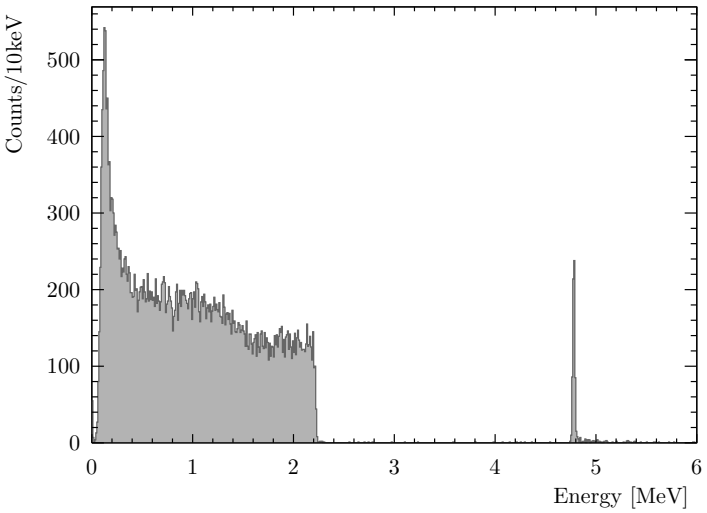

Figure 5.7: Energy spectrum of the ^{147}Sm α measurement run. The calibration is done with the neutron capture peak at 4.78 MeV. ^{147}Sm decays to ^{143}Nd under the emission of a α particle with an Q-value energy of 2310 keV. The α particle has to travel through the source and leave the material to reach the detector and release part of the energy. Therefore, a sharp edge with a continuous spectrum is observed in the measurement. A light yield cut reduces the electron/gamma background for the plot.

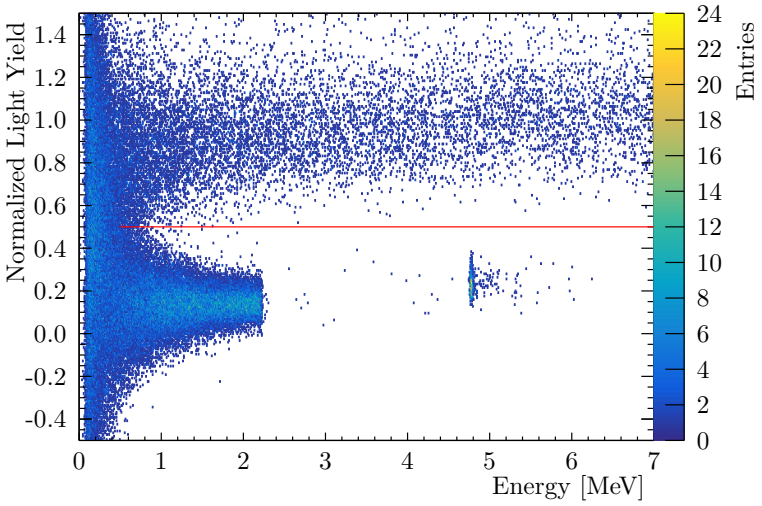

Figure 5.8: Normalized light yield for the ^{147}Sm α run. An optimum filter is applied for the light channel, whereas a truncated standard event fit is used for the phonon signal. The light yield is normalized to 1 for electron/gamma events in the energy range between 4 MeV and 6 MeV. To distinguish α events from electron/gamma events, the red line indicates a relatively strict cut at a normalized light yield of 0.5. A clear separation between α and electron/gamma events is possible down to an energy of 1 MeV.

down to 1 MeV.
To validate the calibration method using the neutron capture peak, the spectrum measured with the lithium-fluoride detector is calibrated with this line. Then a fit to the edge of the α spectrum is done and compared to the energy spectrum measured for an ^{147}Sm α source in a silicon surface barrier detector. A comparison of those spectra is shown in figure 5.9, where the measured spectrum in the cryostat is drawn on the left and the spectrum for the silicon barrier measurement on the right. A fit to the spectra leads to an edge at (2221.32 ± 27.46) keV and (2238.36 ± 6.22) keV for the cryo measurement and the silicon barrier measurement, respectively. The discrepancy is inside the fit errors. This fits the expected alpha energy value of $E_\alpha = 2.23 \pm 0.02$ MeV [145]. Therefore, the energy calibration with the neutron capture peak at 4.78 MeV is a suited calibration method and is used in the following.

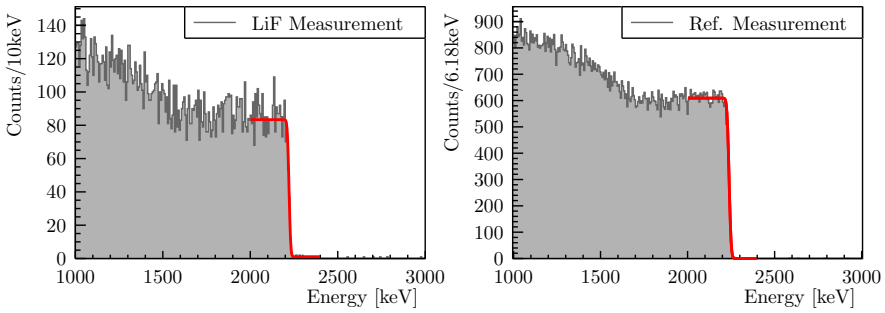

Figure 5.9: Comparison of the energy spectrum measured for an ^{147}Sm α source in the cryostat irradiating a lithium-fluoride detector (left) and a silicon barrier detector measurement (right). A fit to the spectra leads to an edge at (2221.32 ± 27.4607) keV for the cryostat measurement and (2238.36 ± 6.2228) keV for the silicon barrier detector measurement. The discrepancy is inside the fit errors. Therefore, the energy calibration with the neutron capture peak at 4.78 MeV is a suited calibration method.

5.2 UGL Cryostat Muon Veto

The previous sections describe the analysis steps and the calibration of the lithium-fluoride measurement in the underground laboratory. The following section presents the final results, starting from the efficiency calculation of the muon veto. Afterward, the muon-induced neutron spectrum and the total neutron spectrum are shown.

5.2.1 Light Yield Cut for Neutron Selection

For the analysis of the neutron background, a cut has to be defined to distinguish the alpha/tritium band from the electron/gamma band. Figure 5.10 shows the normalized light yield for the background measurement of run22. Bands from a Romeo band fit for the electron/gamma and alpha/tritium bands are included. The light yield of the electron/gamma-band at 5 ± 1 MeV is selected, and a gaussian is fitted to both spectra. The mean value is referred to be 1. For the neutron selection, 2σ from the mean value of the band fit is accepted. Therefore, 95 % of all events in the alpha/tritium band are selected with the cut. The expected leakage from the electron gamma band is calculated to be < 1 %.

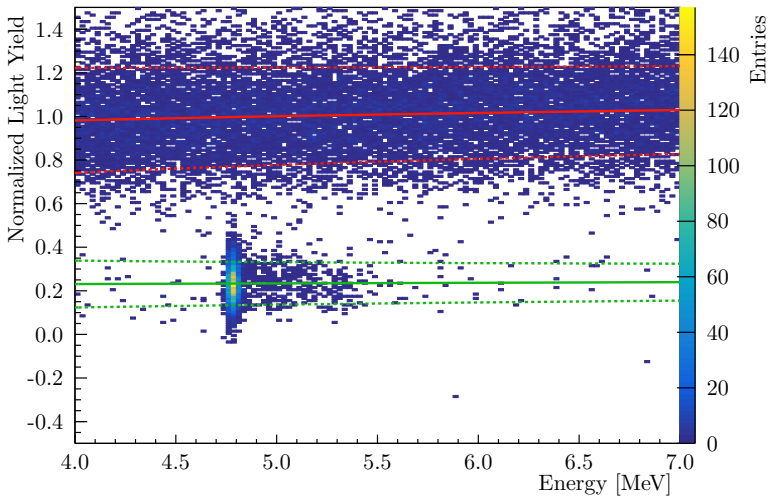

Figure 5.10: Normalised light yield for the background measurement of run22. Bands from a Romeo band fit for the electron/gamma and alpha/tritium bands are drawn. The light yield of the electron/gamma band at 5 ± 1 MeV is selected, and a gaussian is fitted to both spectra. The mean value is referred to be 1. For the neutron selection, 2σ from the mean value of the band fit is accepted.

5.2.2 Neutron Timing Information

For the lithium-fluoride run, the UGL muon veto is used to gather information about events induced by muons in the surrounding material of the cryostat. As already described, the muon veto triggers when one of the panels triggers. The logical signal is shaped and recorded with the standard cryo data acquisition. To evaluate coincident events between cryo detector and muon veto, a new timing parameter has to be included in the analysis. In the framework of this thesis, a parameter was developed to calculate the

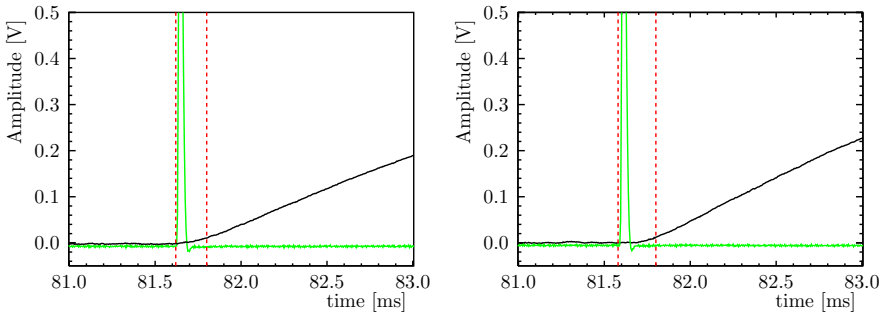

Figure 5.11: *Left:* Zoom in on a direct muon hit event with the cryo pulse in black and the muon veto pulse in green. The onsets are highlighted with red dashed lines. *Right:* Zoom in on a neutron capture event with the cryo pulse in black and the muon veto pulse in green. Red dashed lines indicate the onsets. Both events are classified as muon-induced events. However, the cryo signal for a neutron capture event is later with respect to the muon veto pulse than for a direct muon hit.

time difference between a recorded cryo pulse and the closest muon veto signal. For this, the onset of both cryo pulse and muon veto signal is calculated. Since the CMP parameters are relatively rough (described in section 4.2), the results of the truncated standardevent fit (see section 4.4) are used. The standardevent fit calculates the optimum shift parameter besides the amplitude and RMS of the fit. The optimum shift is defined as the time the template had to be moved to describe the recorded pulse best. Summed up with the onset of the standardevent, a new parameter is defined in the following called the optimum onset. The optimum onset, therefore, describes the onset of the measured pulse after the standardevent fit.
A moving average is used to calculate the onset of the closest muon veto pulse. For the moving average, a sampling number of 10 samples is chosen. Suppose a channel is larger than 10σ of the moving average RMS. In that case, the algorithm sets the onset of the muon veto pulse (muon onset) and pauses for 20 channels, which corresponds to the length of a muon veto pulse of 100 μs. Afterward, the minimum distance is calculated by minimizing the difference between the optimum onset and muon onset. Figure 5.11 shows two muon-induced events. The left event is a zoom-in of a direct muon hit in the phonon detector. In black, the cryo pulse and the muon veto pulse in green. The onsets are highlighted with red dashed lines. The right event is a zoomed neutron capture event. Again in black, the cryo pulse, and in green, the muon veto pulse with highlighted onsets via red dashed lines. Both classes of events are muon induced. However, the cryo signal for a neutron capture event is later concerning the muon veto pulse than for a direct muon hit. This is expected as for neutron capture the neutron first has to be created

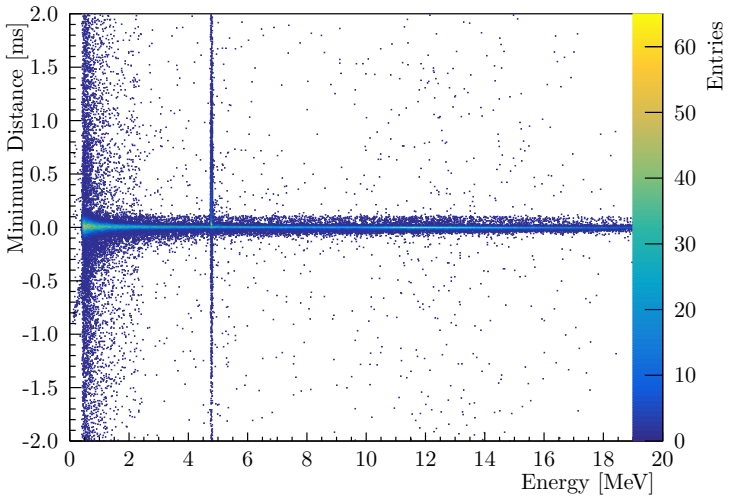

Figure 5.12: Timing parameter (minimum distance) between muon veto and phonon detector as a function of the energy. The minimum distance is calculated as the onset difference of an event recorded in the phonon detector and the closest muon veto pulse. For energies larger than 2.6 MeV, most of the events are close to zero time difference. A large spread can be observed around the neutron capture peak energy.

in the lead and captured in the lithium-fluoride detector. Hence, the cryo signal is delayed compared to a direct muon hit.

Figure 5.12 shows the minimum distance as a function of the energy between 0 MeV and 20 MeV. For energies larger than 2.6 MeV, most of the events are close to zero time difference and hence muon induced. The highest gamma energy from natural decay is the decay of ^{208}Tl with the energy of 2.6 MeV. All other gamma lines have lower energy. Therefore, gamma events are only expected for energies smaller 2.6 MeV. Higher energetic events must be muon induced and should mainly be detected with the muon veto. For neutron capture events, the time difference spreads over a larger area due to the delay described before. This large spread is also expected since not all neutrons captured have a muon-induced origin or no origin in the surrounding material of the cryostat.

The algorithm presented has some limiting factors. Due to the high muon rate ($\sim$ 300 Hz), there is a non-zero probability of having two pulses very close to each other. When the distance is smaller than the sampling length of the moving average algorithm, the second muon veto pulse can not be detected. The probability of having a random pulse in the critical time window of 100 μs before the coincidence muon veto pulse is calculated to be 2.9 %. An example pulse is shown in figure 5.13. For the minimum distance calculation,

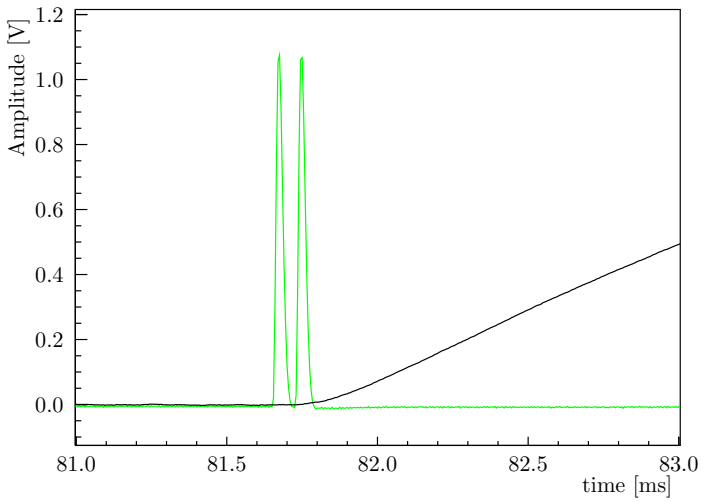

Figure 5.13: Example pulse for a wrong tagged muon veto pulse. Because of the moving average used, the searching algorithm tags the first muon veto pulse to the cryo pulse, whereas the second would be the closest.

the pulse on the left is used by the algorithm and, therefore, wrongly tagged. Because the distance between the two muon veto pulses is smaller than the sampling length, the algorithm is "blind" for the second pulse.

5.2.3 Tagging Efficiency of Direct Muon Hits

An efficient muon veto is crucial for the measurement to tag muon-induced events successfully. The tagging efficiency is calculated to validate the muon veto, which is defined as the ratio of the number of direct muon hits and the number of tagged muon events.

Figure 5.14 shows the light yield plot for non-neutron capture events selected via a light yield cut. The events in the band with low light yield (slightly above zero) are events with a direct hit in the phonon channel only and, therefore, a small light detector signal coming from scintillation light. Events with higher light yield are events with a direct hit in both phonon and light detector. Since the highest gamma line has an energy of 2.6 MeV events in the phonon detector above, this energy can be assumed as muon events. Because the energy deposited in the light detector can be rather high for direct muon hits ($\mathcal{O}(250\,\mathrm{keV})$ for muons with $E_\mu > 10\,\mathrm{GeV}$) it is very likely to have so-called flux quantum (FQ) losses. Flux quantum losses are events where the rise of the pulse is too fast. The SQUID can not follow and is losing one or more flux quanta. This leads to a lower baseline in discrete steps at the decaying side of the pulse. A correct energy estimation is not

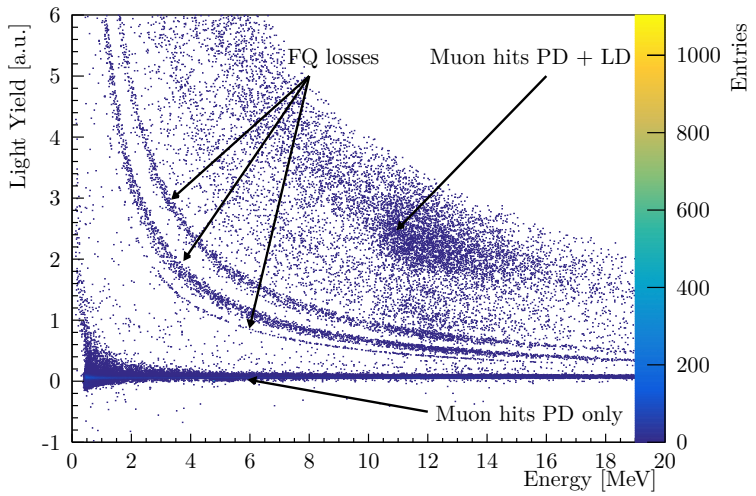

Figure 5.14: Light yield plot for non-neutron capture events. The events in the band with a low light yield of ~ 0.1 are classified as muon events with phonon signals only. Events with higher light yield are muon events with a hit in both phonon and light detector. The deposited energy in the light detector can be rather high. Therefore, it's very likely to have so-called flux quantum (FQ) losses in the SQUID. Flux quantum losses are events where the pulse's rise is too fast for the SQUID and leads to a loss of one or more flux quanta.

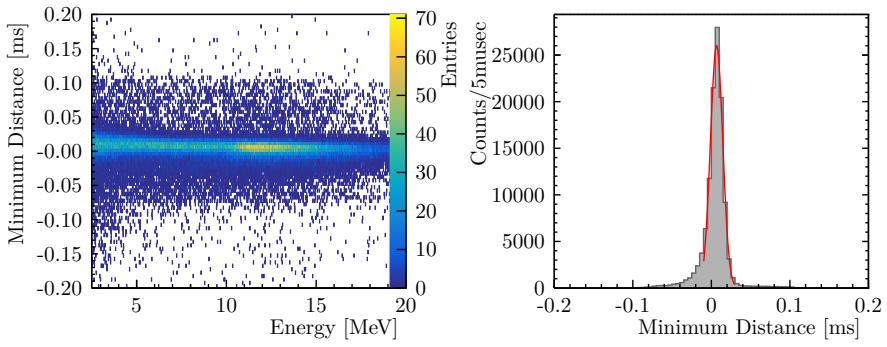

Figure 5.15: *Left:* Timing parameter (minimum distance) as a function of the energy between 2.6 MeV and 20 MeV for events classified as muon events. The neutron capture events are removed by applying a light yield cut. *Right:* Projection of the minimum distance. The shape of the spectrum is fitted with a Gaussian. The tail on the left originates from the non-zero probability of a muon veto pulse being wrongly assigned to a cryo pulse because it is randomly closer to the cryo pulse.

trivial for pulses with flux quantum losses.
The minimum distance for all classified muon events is shown in figure 5.15. The left plot shows the minimum distance as a function of the energy between 2.6 MeV and 20 MeV for events in the electron/gamma band. The neutron capture events are removed by applying a light yield cut. A projection of the minimum distance is drawn on the right side of figure 5.15. The shape of the spectrum is fitted with a Gaussian. The tail on the left originates from the non-zero probability of a muon veto pulse being wrongly assigned to a cryo pulse because it is randomly closer to the cryo pulse (described in section 5.2.2). A coincidence window has to be defined to decide if an event is a muon event.

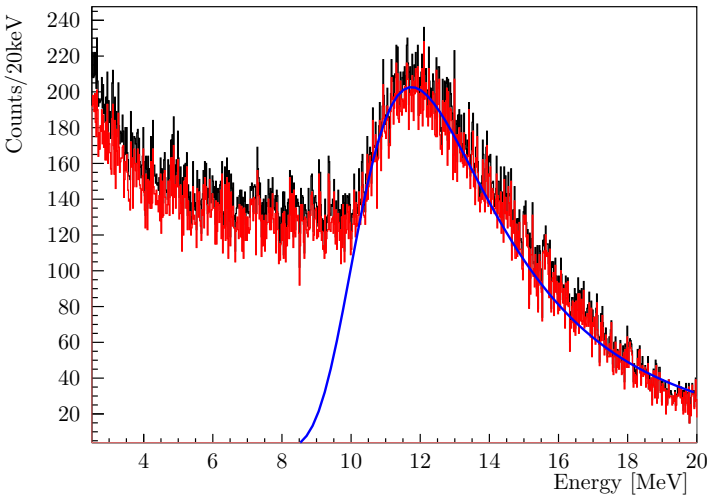

Figure 5.16: Tagging efficiency of the muon veto. *Black:* Measured spectrum between 2.6 MeV and 20 MeV. The neutron capture events are neglected via a light yield cut. Events with a higher light yield and flux quantum losses in the light detector are included. *Red:* Spectrum off tagged events from the measured spectrum in black. For tagging, the minimum distance parameter is used as described in figure 5.15. Events are accepted with a 5σ distance from the mean value. The efficiency of the muon veto is determined to be 94 %. *Blue:* Landau fit. The peak of the Landau fit is at an energy of 12.1 MeV.

From the fit (figure 5.15 right side), a 5σ coincidence window is selected. Figure 5.16 displays the tagging efficiency of the muon veto. In black, the measured spectrum between 2.6 MeV and 20 MeV, as shown in the light yield plot 5.14, is drawn. The neutron capture events are neglected via a light yield cut. Events with a higher light yield and flux quantum losses in the light detector are included. The red spectrum consists of the tagged events

from the measured spectrum. The efficiency of the muon veto is determined to be 94 % by dividing the two integrals of tagged muon events and all muon events. The probability of finding a random coincidence, i.e., an event tagged wrongly as a muon event, is determined to be 2.3 %. Since muons are minimal ionizing particles, a Landau distribution is expected. A Landau fit is shown in figure 5.16 in blue. The fit describes the data well. The peak of the Landau fit is at an energy of 12.1 MeV. This agrees with the expected maximum of the deposition energy of muons with 2 MeV/cm and the crystal's geometry.

5.2.4 Muon Veto Coincidence Measurement

To evaluate the muon-induced neutron spectrum, the minimum distance parameter is used, which is the time difference between an event in the cryo detector and the closest muon veto signal. Thus, the larger the value of the

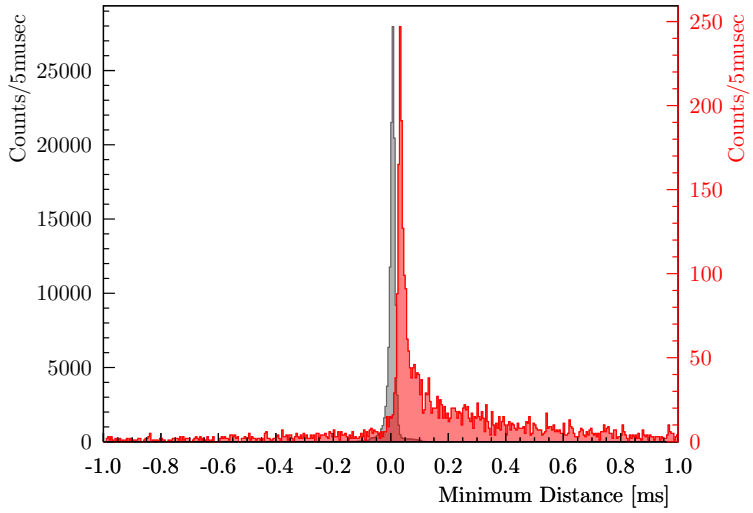

Figure 5.17: Comparison of the minimum distance parameter between 4 MeV and 7 MeV for events in the electron/gamma band (grey, left y-axis) and events around the neutron capture peak (red, right y-axis). The two populations are separated via a light yield cut. A sharp peak around zero with a high statistic of $\sim$ 26000 events can be observed for the electron/gamma band. For events around the neutron capture, a less populated ($\sim$ 250 events) and $\sim$ 50 μs delayed peak with a tail towards an increased time difference between cryo detector and muon veto is measured.

parameter, the later the cryo pulse with respect to the muon veto signal. Figure 5.17 shows a comparison of the minimum distance parameter for events in the electron/gamma band (grey), which are identified as muons and events around the neutron capture peak (red) in the energy range of 4 MeV to

7 MeV. The left y-axis corresponds to the electron/gamma events, whereas the right y-axis corresponds to the neutron capture events. A light yield cut is applied to distinguish between electron/gamma and neutron capture events. For the direct muon events, a sharp peak around zero is observed with a high statistic of ~ 26000 events in the peak. The neutron capture peak is less populated with ~ 250 events. It shows a tail towards higher minimum distance times, which means an increasing delay of cryo events with respect to the muon veto signal. This can be explained by the different traveling and/or thermalization times of neutrons created in the surrounding material, e.g., lead, before capturing them. Further, a discrepancy of $\sim 50\,\mu$s between direct muon events in the electron/gamma band and neutron capture events is measured.

To investigate the muon-induced neutron background, the time difference

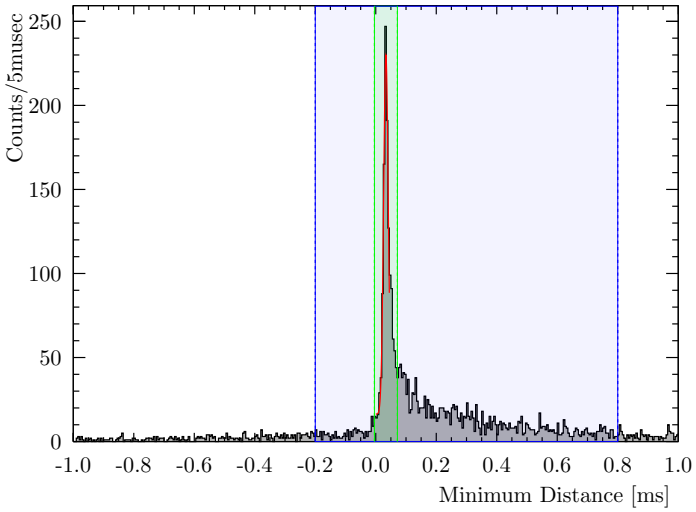

Figure 5.18: Definition of coincidence window. The time difference between cryo detector event and the closest muon veto event (minimum distance) for events in the neutron capture region with two defined coincidence windows is shown. For the definition of a first window, a Gaussian is fitted to the peak (red) and all events with an absolute time difference smaller than 5σ (width of coincidence window: $85\,\mu$s) are selected (green area). This coincidence window is further called a short window. Minimum distances between -0.2 ms and 0.8 ms define the second coincidence window, where the flanks on the left and right of the peak are included (blue). This coincidence window is further called the long window.

information between the cryo detector and muon veto (minimum distance parameter) is used by applying two coincidence windows of different lengths, shown in figure 5.18. For the definition of a first and strict coincidence window,

a gaussian function (red) is fitted to the peak of the minimum distance, and only events with an absolute time difference closer than 5σ to the mean value (green) are accepted (further labeled with short window). For the definition of a second coincidence window (further labeled with long window), events with time differences between -0.2 ms and 0.8 ms are selected, where the decaying flanks on the left and right of the peak are included (blue). Therefore, the sharp window gives information about fast-captured neutrons, whereas the long window tags most muon-induced neutrons.
Figure 5.19 shows the final measured muon-induced neutron spectrum with the large coincidence window applied in the energy range between 4 MeV and 7 MeV. This spectrum is used for the following calculations, e.g., the initial neutron energy spectrum.

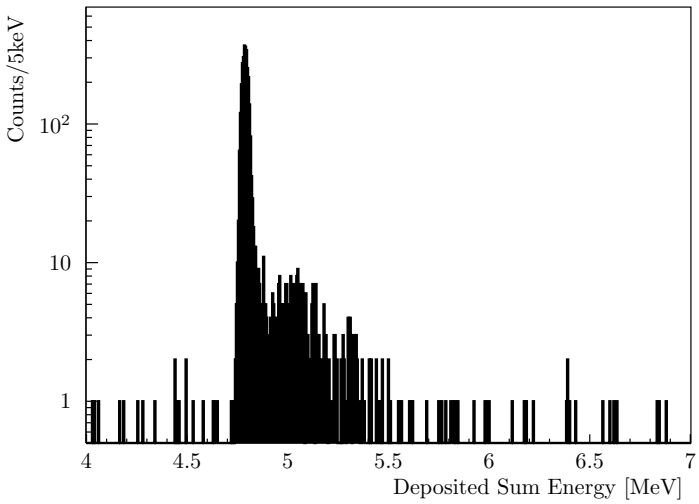

Figure 5.19: Measured energy spectrum after muon veto coincidence cut with the long window (see figure 7.3) in the energy range between 4 MeV and 7 MeV. For the following calculations, this spectrum is used.

5.3 Calculation of Incident Neutron Flux

The lithium-fluoride neutron monitor uses the advantage of the neutron capture on ^{6}Li. A measured event with deposited energy in the crystal is always the sum of initial neutron energy and the energy of the created alpha and tritium. This implies that measured energy x in the detector can be translated into an initial neutron energy of $x - 4.78$ MeV. The first initial energy bin with a bin width λ ($[0\,\text{keV}, \lambda]$) corresponds to the measured energy range of [4.78 MeV,4.78 MeV + λ]. In general, the rate of neutron captures

can be calculated with

$$R = N \cdot \phi \cdot \sigma \tag{5.2}$$

where N is the number of targets in the volume (here ^{6}Li atoms), ϕ the flux of neutrons and σ the energy-dependent cross-section of the capture process. Further, the rate is the ratio of the number of events C and the measurement time t_{meas}:

$$R = \frac{C}{t_{meas}} \tag{5.3}$$

Therefore, the initial neutron flux as a function of the energy E can be calculated via

$$\phi(E) = \frac{C(E)}{t_{meas} \cdot \sigma(E) \cdot N} \tag{5.4}$$

For the measurement presented in this work $N = 1.7 \cdot 10^{23}$ ^{6}Li targets are in a volume of $V = 37.68\,\mathrm{cm}^3$, taking into account that the natural abundance of ^{6}Li is 7.5 %. The measurement time is 326.33 h. The cross-section of the neutron capture process is an energy-dependent function. Figure 5.20 shows the selected cross-section for each energy bin. As a cross-section value, the value of the center of each bin is chosen. The error of the cross-section is selected as the maximum value and minimum value of the cross-section of each bin. Especially in the first energy bin, the cross-section varies by three orders of magnitude because of the exponential rise of the cross-section (compare cross-section of ^{6}Li capture in figure 3.4). For 20 keV neutrons, for example, a cross-section of 1.1 barn is expected, whereas for thermal neutrons 938.8 barn.
The final calculated flux as a function of the initial neutron energy is shown in figure 5.21, according to equation 5.4. For the propagation of the errors, statistical errors and the error in the cross-section are considered. Due to the large discrepancy in the cross-section in the first bin also the neutron flux with a value of $15.6^{+0.6}_{-15.6}\,\mathrm{cm}^{-2}\mathrm{h}^{-1}(20\,\mathrm{keV}^{-1})$ shows large errors with spreading over four orders of magnitude. For initial neutron energies above 100 keV the flux varies between $(0.45 - 0.11)\,\mathrm{cm}^{-2}\mathrm{h}^{-1}(20\,\mathrm{keV}^{-1})$. Within the presented measurement in the energy range up to 500 keV a total muon-induced neutron flux of $32.4^{+0.9}_{-17.9}\,\mathrm{cm}^{-1}\mathrm{h}^{-1}(20\,\mathrm{keV})^{-1}$ is found.
Calculating the initial neutron energy spectrum using the effective cross-section alone can only be a rough estimator of the neutron flux. In particular, the lowest energy bin, which is most important for the neutron background in rare event search experiments, does not provide an accurate value because the change in the effective cross-section is too large for the capture process in the first 10 keV. Moreover, the calculation does not consider other important parameters such as the geometry of the detector crystal, inelastic and elastic

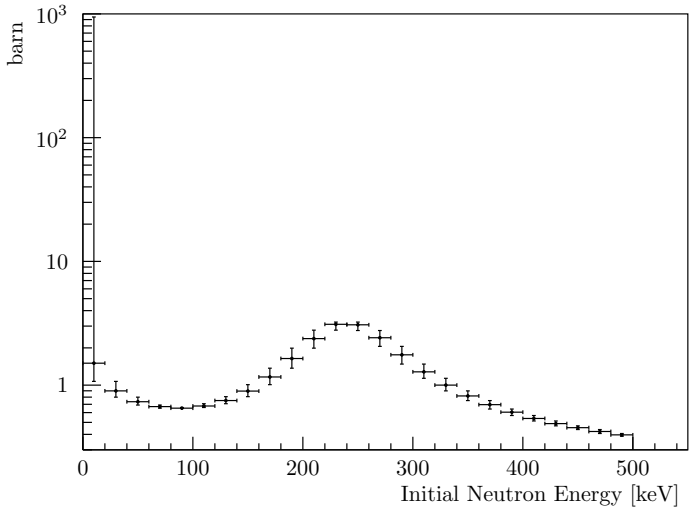

Figure 5.20: Cross Section of the ^{6}Li capture process with a 20 keV binning. In the first 20 keV, the cross-section varies strongly according to the energy. 20 keV neutrons have a cross-section of 1.1 barn, whereas for thermal neutrons 938.8 barn. For the calculation, an averaged cross-section of 1.5 barn is chosen, according to the center of the bin at 10 keV. The error on the cross-section is selected as each bin's maximum and minimum cross-section.

scattering processes in the detector crystal before the capture process, or other reaction processes in the detector. In particular, scattering processes, which are assumed to be the dominant process in the crystal, can lead to an overestimation of the neutron flux. Since the measured energy in the detector is always the sum of the energy deposited during a scattering process and the energy released during the capture process, the effective cross-section for the capture process may be higher because the energy has already been deposited in the crystal and the remaining neutron energy is lower than the initial neutron energy.
Furthermore, the geometry can influence the result because the larger the crystal is, the more possible scattering processes can occur before the capture. To account for all these factors, additional simulations are required. A neutron simulation for the described detector and two unfolding methods are presented in the following chapters.

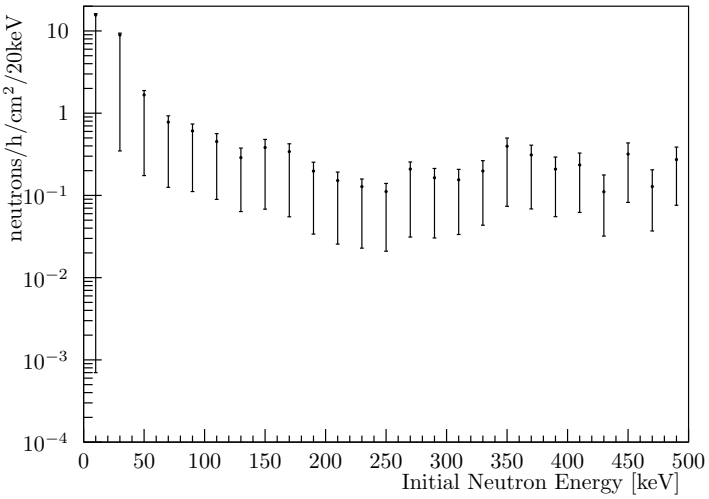

Figure 5.21: Calculated neutron spectrum up to 500 keV incident neutron energy. The spectrum is calculated using the cross-section of the capture process according to figure 5.20. The energy scale is binned in 20 keV steps. For the propagation of the errors, statistical errors and the error in the cross-section are considered.

Chapter 6

Simulations of the Lithium - Fluoride Neutron Monitor

In chapter 3, a cryogenic neutron monitoring system based on the neutron capture process on ^{6}Li in a 100 g lithium-fluoride crystal is described. A four months cryogenic measurement and its results are presented in chapter 5. In addition, a first initial neutron spectrum was calculated based on the cross-section of the neutron capture process on ^{6}Li. The cryogenic in-situ neutron monitoring system is developed with the aim of measuring the neutron flux inside the experimental volume of rare event search experiments down to sub-keV energies.
The measured neutron signal and, therefore, through a neutron deposited energy in the detector crystal is the sum of released energy due to scattering processes and the released energy due to a neutron capture and the resulting prompt decay of ^{7}Li. A simulation with a simplified geometry was performed in cooperation with the Technical University of Vienna [146][147]. The goal of the simulation is to study the neutron response in LiF, which is the information on the energy deposited in the LiF crystal of a neutron with an initial E_i. Out of the response and the measured energy spectrum, an initial neutron energy spectrum (neutron flux) can be calculated. In the following, the neutron simulation is presented.

6.1 Introduction

The neutron capture on ^{6}Li leads to an excited state of ^{7}Li which immediately decays into an alpha ($E^{\alpha}_{kin} = 2.73\,\mathrm{MeV}$) and a tritium ($E^{t}_{kin} = 2.05\,\mathrm{MeV}$) particle, which release the energy of 4.78 MeV in the detector [148]. In addition to the 4.78 MeV, the initial kinetic energy of the neutron is deposited in the crystal via scattering processes before the neutron capture process or directly during the capture of the neutron. Due to the presence of inelastic neutron nucleus scattering processes on lithium and fluorine, the initial neut-

ron energy can not simply be obtained by folding the measured spectrum with the cross-section of the neutron capture process for more reliable results (compare section 5.20). The goal of the simulation presented is to calculate a neutron detector response function to unfold the initial neutron energy from a measured spectrum. The detector response is defined as the transfer matrix, which translates an initial neutron energy E_i to all possible energy depositions E_{dep} in the LiF crystal weighted by the reaction probability. For the simulation, the CRESST simulation software ImpCRESST was used.

6.1.1 The Simulation Softwares ImpCRESST and Geant4

ImpCRESST (Improved CRESST Simulation) is a simulation toolkit developed inside the CRESST collaboration. It is based on Geant4 (Geometry and Tracking, version 4) [149] and implements the CRESST setup with respect to the geometry of the cryostat and detector modules but also, e.g., the UGL, materials, involved physics models, and backgrounds and provides different particle sources. ImpCRESST is continuously improved inside the CRESST collaboration. Due to its structure, the implementation of new materials or geometries is possible with an adequate amount of effort.
As mentioned, ImpCRESST is based on the comprehensive Monte Carlo simulation framework Geant4. It has been developed at CERN as a general simulation tool for the simulation of particles traveling through matter with the main focus on collider experiments and, therefore, high energetic particles. Still, it can also be adapted for other experimental setups [149]. Geant4 simulations are done on an event-by-event basis, all events are, therefore, treated independently. In general, Geant4 is a mighty toolkit for particle interactions with matter over a broad energy range. It includes all necessary information about the interaction, e.g., the primary and secondary particle, the energies involved, and the reaction process. It is freely available and written in C++, using the object-oriented approach, providing easy modification and extension possibilities.

6.1.2 Neutron Simulation on Lithium-Fluoride

For the simulation, the parameters of the LiF crystal were implemented with respect to geometry, temperature, and material. However, for simplicity, not the complete detector is simulated but the crystal only. Components like the housing, the light detector, and the thermometer are not implemented.
Figure 6.1 shows the simulated setup. A cylindrical 100 g lithium-fluoride crystal with a diameter of 4 cm and a height of 3 cm was placed in a vacuum. The temperature of the crystal was considered to be 20 mK. The density implemented in the simulation for lithium-fluoride was 2.64 g/cm^3, corresponding to molar masses of 6.94 g/mol and 19.00 g/mol for lithium and fluorine, respectively. The abundance of isotopes follows the natural

abundance of the element and is already included in Geant4. For lithium the two isotopes ^{6}Li and ^{7}Li were included with a natural abundance of 7.4 % and 92.6 %, respectively. For fluorine, the only stable and naturally occurring isotope is ^{19}F.

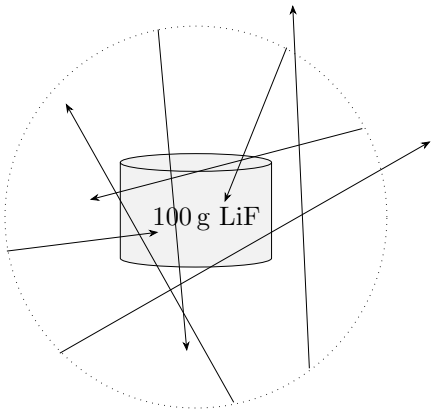

Figure 6.1: Simulated setup. A cylindrical lithium-fluoride crystal with a diameter of 4 cm and a height of 3 cm is placed in a vacuum. A sphere with 5 cm is defined around the crystal for particle creation. Neutrons with energies between 0 MeV and 3 MeV are created isotropically according to a linear spectrum and sent under a random angle inside the volume. In total, 10^9 neutrons are simulated.

The particle source is based on the GPS (General Particle Source) and is used to simulate neutrons. It is defined as a spherical surface with radius 5 cm, and the detector is placed inside the center. Neutrons are created on the surface of the sphere with a random number generator, according to a flat energy spectrum, and are emitted toward the inside of the sphere. The angle of the particle direction on the starting point is chosen randomly at the beginning of each event. Since a uniform distribution of the random number generator is used, the source is fully isotropic.
With the setup described, two dedicated simulations were run. The first with a flat energy spectrum between 0 MeV and 3 MeV with a total number of 10^9 simulated neutrons. To get a better resolution of the thermal neutron peak, a second simulation was run with 10^6 simulated neutrons with an energy of 0.025 eV, corresponding to the energy of thermal neutrons. In total, 5.8 TB of simulation data was created. To keep the files in an acceptable and manageable size, the simulations were split into 1000 simulations with 10^6 simulated neutrons each for the flat energy spectrum and ten simulations,

each with 10^5 events for the thermal neutron simulation.

6.1.3 Data Processing and Analysis

The processing and the analysis of the simulated data are done with the object-oriented modular scientific software package ROOT [136]. ROOT is written in C++ and was developed by CERN. The scripts used in the analysis are based on the work of [146]. A simulation run consists of a list of initialized events, starting with a primary particle. The data of each event, like hits and tracks, is stored in a simulation file. To analyze the data, one has to iterate over all events in all ROOT files created from ImpCRESST. The desired data is extracted from the simulation according to an event library defined by ImpCRESST to properly interpret the data since ImpCRESST defines the structure of all events.
Because ImpCRESST stores the tracks in every detail, the execution time for a single script can be too long ($\mathcal{O}(50\,\mathrm{h})$) for reasonable data analysis. To avoid that, the data is reduced by a macro, which selects the needed event information beforehand and stores it in a new ROOT file with the new data structure. The process can be parallelized easily in order to reduce the execution time. The reduction of the files is based on C++ STL container classes [146]. With this method, the file size can be reduced to 1 % of its original size.

6.2 Detector Response on Neutrons

An important result from the simulation is the information about the neutron response on a lithium-fluoride detector as it was used for the measurements. With the response, the initial neutron spectrum can be derived from the measured spectrum. In the following, the results of the simulation are described.

6.2.1 Source Energy Distribution

For the simulation a flat energy spectrum between 0 MeV and 3 MeV is used. In order to not bias the detector response for a specific energy, it has to be ensured that the real simulated energy spectrum is flat.
The energy distribution of all simulated events is shown in figure 6.2. In total, 10^9 neutrons were simulated. With a bin width of 20 keV over an energy range of 3 MeV in average $6666.\overline{66} \cdot 10^3$ neutrons are created per bin. The observed spreading Δn around the mean of $6666.\overline{66} \cdot 10^3$ neutrons is maximal $\Delta n < 7 \cdot 10^3 \mathrel{\widehat{=}} 0.1\,\%$. The Poissonian standard deviation is given by $\sigma = \sqrt{\Delta n} = 2582$. Thus the deviation from the mean is calculated to be $\Delta n = 2.7\sigma$. The energy distribution can be considered flat.

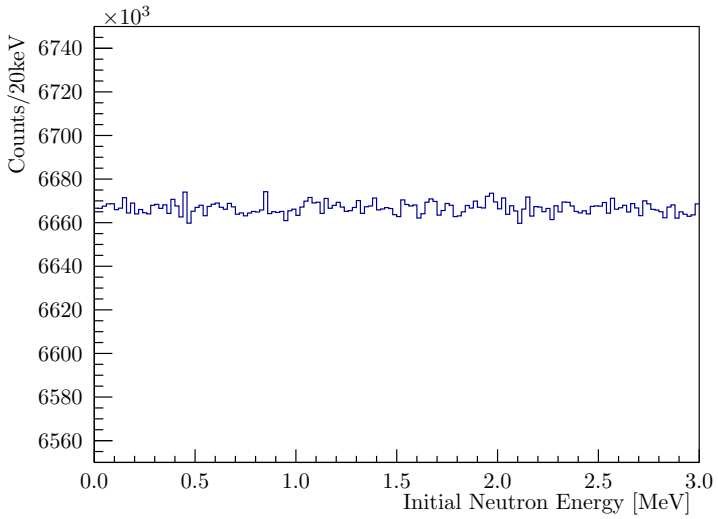

Figure 6.2: Energy distribution of all simulated events. In total, 10^9 neutrons were simulated (Integral over the spectrum is 10^9). With a bin width of 20 keV over an energy range of 3 MeV in average $6666.\overline{66} \cdot 10^3$ neutrons are created. The spreading Δn around the mean is calculated to be maximal $\Delta n < 7 \cdot 10^3 \,\widehat{=}\, 0.1\,\%$. The standard deviation is given by $\sigma = \sqrt{\Delta n} = 2582$. Thus the deviation from the mean is calculated to $\Delta n = 2.7\sigma$. The energy distribution, therefore, can be considered flat.

The sensitivity versus initial neutron energy is shown in figure 6.3. In black, the interaction probability for all simulated neutron-induced processes of neutrons intersecting the LiF crystal is shown as a function of the initial neutron energy. Only neutron events leading to a non-zero energy deposition are included (Left axis). In red, the probability of neutron capture on a ^{6}Li atom as a function of the initial neutron energy is presented (right axis). On average, 50 % of all neutrons entering the crystal are depositing non-zero energy with an increased probability below 500 keV up to 50 %. Most of the interactions are elastic and inelastic scattering processes. The probability of being captured by a ^{6}Li atom is, on average, two orders of magnitude lower. The spectrum shows that the LiF module is most sensitive to neutrons with energies below 500 keV. It is expected that the measured statistic above this value will become small.

6.2.2 Lithium-Fluoride Neutron Response

Different reactions in the lithium-fluoride detector must be considered for the neutron detector response. The main processes are elastic and inelastic scattering on one of the nuclei.

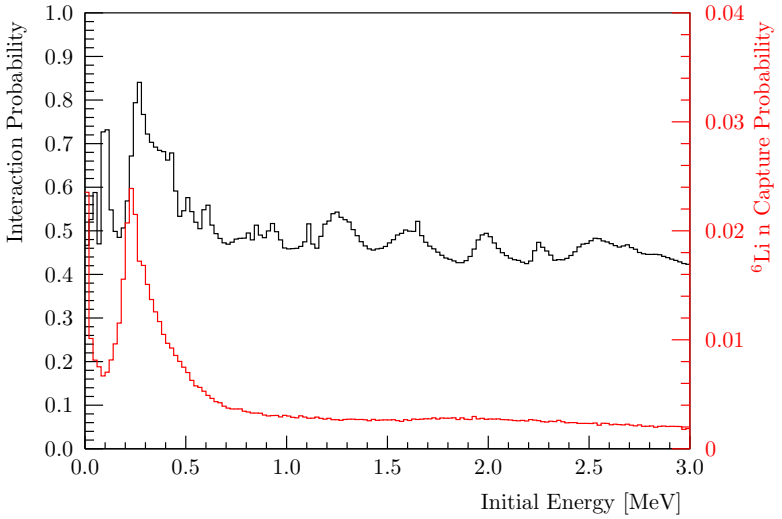

Figure 6.3: *Black:* Interaction probability for all simulated neutron-induced processes of neutrons intersecting the LiF crystal as a function of the initial neutron energy. Shown are neutron events leading to a non-zero energy deposition (Left axis).*Red:* Probability a neutron is captured by a ^{6}Li atom vs initial neutron energy (right axis).

In the case of an elastic neutron scattering process, the incoming neutron scatters off the target nucleus without being absorbed or leading to internal excitations of either the nucleus or the neutron. The momentum of the recoiling nucleus can have any angle concerning the incident direction, and the recoil energy can be energy up to a maximum of:

$$E_R^{max} = 4\frac{m_n \cdot m_t}{(m_n + m_t)^2} E_n \tag{6.1}$$

where m_n is the mass of the incident neutron, m_t the mass of the target nucleus and E_n the incident neutron energy [150].
In the case of inelastic neutron scattering, the neutron is absorbed by the target and re-emitted. During this process, the internal energy of the target nucleus is changed and de-excited via the emission of γs or hadrons. The evaluation of the kinematics in the inelastic neutron scattering process is a more difficult process than elastic scattering since the total kinetic energy is not fixed.
For lithium-fluoride, the excited states of inelastic neutron scattering for the different nuclei are given in table 6.1. The crystal contains only three different nuclei (^{6}Li, ^{7}Li, and ^{19}F) from two elements, lithium, and fluorine. Since the first line of ^{6}Li has an energy of 2186 keV [151] and is observed

very rarely, only gamma lines from ^{7}Li and ^{19}F are taken into account.
When a neutron enters the crystal, several reactions can happen. Often a combination of these reactions occurs, e.g., multi-elastic and inelastic scattering. The following presents a list of possible reactions of neutrons inside the lithium fluoride detector.

1. $^{19}F+n \rightarrow {}^{19}F+n+x\gamma$: Elastic ($x = 0$) and inelastic ($x > 0$) scattering on ^{19}F

2. $^{19}F + n \rightarrow {}^{20}F + x\gamma$: Neutron capture on ^{19}F

3. $^{19}F+n \rightarrow {}^{16}N+\alpha+x\gamma$: Decay to ^{16}N and α by the release of gamma quanta.

4. $^{6}Li + n \rightarrow \alpha +{}^{3}H$: Neutron capture process on ^{6}Li

5. $^{6}Li+n \rightarrow {}^{6}He+p+x\gamma$: Nuclear fission with and without the emission of additional gammas

6. $^{6}Li+n \rightarrow {}^{6}Li+n+x\gamma$: Elastic ($x = 0$) and inelastic ($x > 0$) scattering on ^{6}Li

7. $^{7}Li+n \rightarrow {}^{7}Li+n+x\gamma$: Elastic ($x = 0$) and inelastic ($x > 0$) scattering on ^{7}Li

8. $^{7}Li + n \rightarrow {}^{8}Li + x\gamma$: Neutron capture with or without the emission of gammas

Reactions 3,5, and 8 are comparably rare and are neglected in the following.
The detector neutron response for all interactions of neutrons with the crystal is shown in figure 6.4. In the 2D histogram, two main interaction processes are visible. The first one (1) shows single, multi-elastic, and inelastic scattering on the elements ^{6}Li, ^{7}Li, and ^{19}F. The border of the spectrum is given by elastic scattering processes with a maximum energy deposition according to equation 7.1.

Nuclei	E_{level} [keV]	E_γ [keV]	I(γ) [%]
^{7}Li	477.6	477.6	100
^{19}F	109.9	109.9	100
	197.1	87.3	<0.06
		197.1	100
	1345.67	1148.5	3.2
		1235.8	96.8
	1458.7	113.0	<0.2
		1261.6	10.7
		1348.8	68.8
		1458.7	20.5
	1554.0	95.3	<0.14
		208.4	<0.011
		1356.9	92.6
		1444.2	4.85
		1554.0	2.55

Table 6.1: Relevant gamma energies for the isotopes ^{7}Li and ^{19}F with its branching ratios. Data were taken from [151].

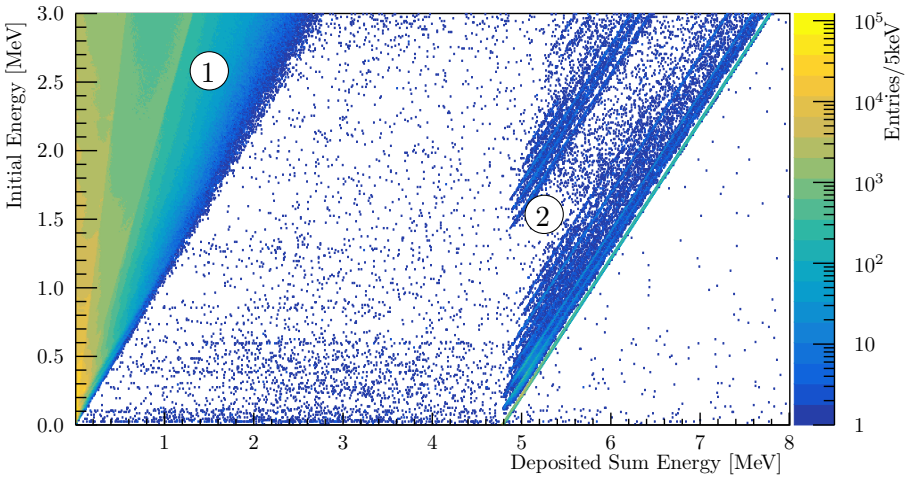

Figure 6.4: Detector neutron response for all neutron interactions in the crystal. There are two different main areas visible. 1: Single and multi elastic an inelastic scattering on ^{6}Li, ^{7}Li and ^{19}F. 2: Neutron capture on ^{6}Li with and without single and multi-elastic and inelastic scattering on ^{6}Li, ^{7}Li, and ^{19}F.

And second (2), the neutron capture process on ^{6}Li with and without single and multi-elastic and inelastic scattering on ^{6}Li, ^{7}Li, and ^{19}F. Figure 6.5 shows a zoom into area 2. Again the detector neutron response for all ^{6}Li

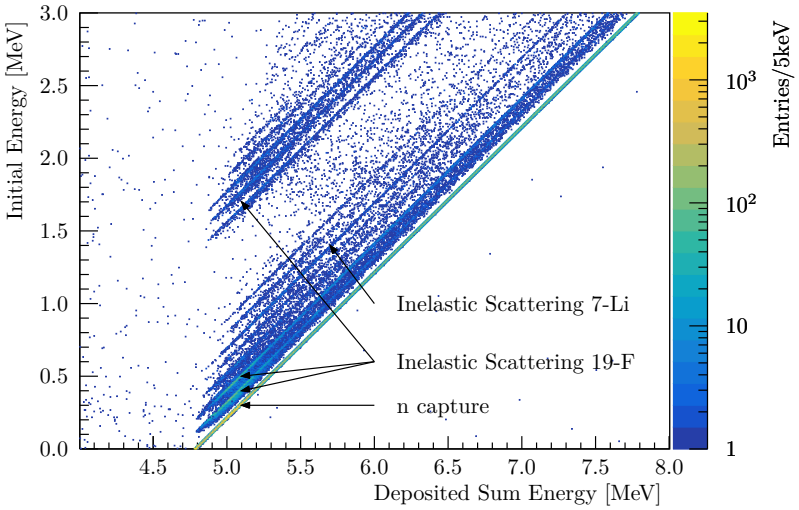

Figure 6.5: Detector neutron response for all ^{6}Li neutron capture interactions in the crystal. Before the capture, there are manifold possibilities for other interactions. For no scattering and pure elastic scattering processes, the deposited sum energy is the initial neutron energy plus 4.78 MeV from the neutron capture. If the sum energy is smaller, then this sum inelastic scattering processes took place according to table 6.1 or arbitrary combinations.

neutron capture interactions in the crystal is presented. Before the capture, there are manifold possibilities for additional interactions of the neutron with the crystal elements. For no scattering or single and multi-elastic scattering processes, the deposited sum energy is the initial neutron energy plus 4.78 MeV from the neutron capture. If the deposited energy is smaller than the sum of capture and initial neutron energy, one or multi-inelastic scattering processes took place with emitted gammas according to table 6.1 and, in addition, arbitrary combinations. The created γs mainly escape the detector with only a little energy deposit in the crystal. Processes for the second-order interactions of γs with the crystal are:

1. *Coherent scattering:* The photon energy is not high enough to liberate the electron from its bound state, and, therefore, no energy is transferred. Only the direction of the scattered photon is changed.

2. *Photoelectric effect:* The photon interacts with an inner shell electron in the atom (photoelectron) and removes it. The photon is completely absorbed from the atom. An outer shell electron fills the vacancy in the inner shell. During this process, an x-ray photon or an Auger electron

is emitted.

3. *Compton scattering:* The photon interacts with free electrons or loosely bound valence shell electrons. The photon is scattered and transfers energy to the electron. Therefore, the wavelength of the scattered photon is different from the initial photon and thus has different energy according to $E = hc/\lambda$. The energy and momentum are conserved. Therefore, the Compton effect is a partial absorption process.

4. *Pair production:* The photon interacts with the strong electric field around the nucleus. The incident photon energy has to be at least 1.022 MeV for the process. The photon is transformed into two particles, an electron and a positron.

For this simulation, the dominant second-order process is Compton scattering, visible in the broadening of the emission bands, especially for low energetic lines of 110 keV and 197 keV with initial neutron energies below 1 MeV.

6.2.3 Initial Neutron Energy Unfolding

Unfolding or deconvolution describes the problem of finding a true and unknown value y from a measured value x. In general, this can be described by solving the mathematical problem [152]

$$f_{\text{meas}}(x) = \int R(x,y) f_{\text{true}}(y) dy \tag{6.2}$$

where $f_{\text{meas}}(x)$ is the measured spectrum, $f_{\text{true}}(y)$ the expected or true specturm, and $R(x,y)$ is the so-called response function that connects both spectrum. Considering that pdfs of x and y are both represented by histograms equation 6.2 can be written as [152]

$$\nu_i = \sum_{j=1}^{M} R_{ij}\mu_j, \qquad i = 1, ..., N, \tag{6.3}$$

where $\mu = (\mu_1, ..., \mu_M)$ corresponds to the expectation values for the histogram of y and $\nu = (\nu_1, ..., \nu_N)$ the expected numbers of events in bins of x. The data are given as a vector $n = (n_1, ..., n_N)$ and can be understood as the observed counts for each histogram bin, which usually differs from the expected values ν. The response function R_{ij} can be interpreted as a conditional probability and can, therefore, be written as $R_{ij} = P(\text{observed in bin } i/ \text{ true value in bin } j)$. The sum over all possible bins of the observed value i leads to [152]

$$\sum_{i=1}^{N} R_{ij} = P(\text{observed anywhere / true value in bin } j) \tag{6.4}$$

Considering a background β relation 6.3 has to be modified by adding an expectation value β_i for the number of entries which are observed in bin i coming from a background event [152]:

$$\nu_i = \sum_{j=1}^{M} R_{ij}\mu_j + \beta_i \tag{6.5}$$

Solving this problem can be done with several methods. Here, two methods are considered for unfolding the measured neutron spectrum to the original neutron energy spectrum.

Method 1: Elastic Only

The first method accounts for a matrix inversion. If $N = M$ and a neglected background equation 6.5 can be written as [152]:

$$\mu_j = \sum_{i=1}^{N} R_{ij}^{-1}(\nu_i - \beta_i) = \sum_{i=1}^{N} R_{ij}^{-1}\nu_i \tag{6.6}$$

The response matrix contains two types of processes. On the diagonal, the elastic scattering processes are taken into account, whereas everywhere else also, the inelastic scatterings are included. For simplicity, only elastic neutron scattering with a final neutron capture process on ^{6}Li only is considered in the following. Thus, inelastic processes are neglected. In this case, the transfer matrix is diagonal. The transfer from the measured to the initial neutron energy spectrum is a simple one-to-one correlation. It includes the information from the capture cross-section combined with the detector geometry. Therefore, a measured event with a summed energy of, e.g., 4.90 MeV implies an initial neutron energy of 120 keV. To resolve the spectrum, the following method is applied. For the simulation, a flat initial spectrum $S(E)$ is given as an input, resulting in a simulated spectrum $S'(E)$, corresponding to the detector's energy deposition. The spectrum $S'(E)$ is folded with the measured energy resolution σ of the detector to the spectrum $S'^{\sigma}(E)$. Therefore, $S'^{\sigma}(E)$ is what one would expect to measure in a LiF detector with resolution σ if a flat initial energy spectrum is present. The initial flux of neutrons S_i for the energy bin i can then be calculated with

$$S_i = S_i^M / S_i'^{\sigma} \cdot f \cdot n_i \tag{6.7}$$

where S_i^M is the i-th bin of the measured spectrum $S^M(E)$, $S_i'^{\sigma}$ the i-th bin of $S'^{\sigma}(E)$, f a normalization factor which includes the measurement time, and the surface of the simulated sphere and, n_i the number of simulated neutrons in the i-th energy bin. To evaluate a systematic error of this method, the inelastic scattering processes have to be considered. Figure 6.6 shows the

x-projection of the neutron response histogram (figure 6.5) subdivided into neutron capture processes without any scattering or with n elastic neutron nucleus scattering processes before the neutron capture (black) and neutron capture processes with m inelastic neutron nucleus scattering events (blue). 20 % of all neutron capture events around the resonance peak have a minimum of one inelastic scattering event. Since the initial energy spectrum is expected to be constant or decrease but not increased with increasing neutron energy, this is expected to be the maximum ratio between elastic and inelastic events. Therefore, this factor is further considered as an upper systematic uncertainty.

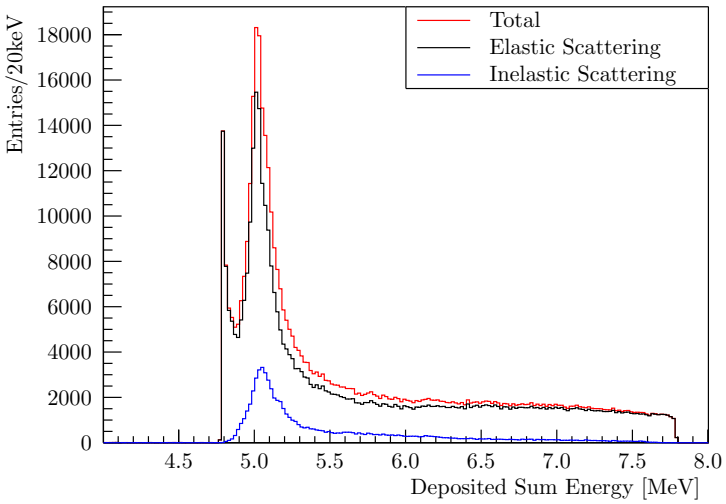

Figure 6.6: Projection to the x-axis of figure 6.5. Shown is the deposited energy in the lithium-fluoride detector. In black, the neutron capture processes without any scattering or with n elastic neutron nucleus scattering processes before the neutron capture. In blue, the neutron capture processes with m inelastic neutron nucleus scattering events.

Method 2: Fit Method

The second method accounts for the neutron capture events with inelastic scattering processes. The idea of the unfolding is to slice figure 6.5 into equal-sized initial neutron energy bins i of 20 keV, which is the resolution of the measured neutron capture peak. The detector response is, therefore, averaged for each bin. The binning of 20 keV allows a statistic large enough for an unfolding. Even though the cross-section (compare figure 3.4 in section 3.2) has an exponential rise in the lowest energy bin, which is expected

to be appropriate for an unfolding. The corresponding deposited energy

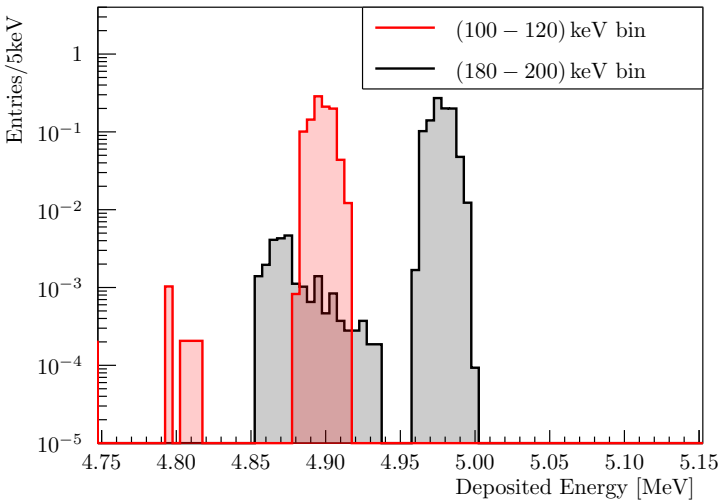

Figure 6.7: Examplary choosen PDFs for the $(100-120)$ keV (red) and $(180-200)$ keV (black) initial neutron energy bin. The PDFs are normalized to a unity integral. Included are all neutron capture events on ^{6}Li.

in the crystal yields a histogram H_i and is normalized to the probability density function (PDF) H_i' for each energy range i (integral = 1). Two selected example PDFs are shown in Figure 6.7. In red for the $(100-120)$ keV and in black for the $(180-200)$ keV neutron energy ranges. Due to the inelastic scattering processes involved, the PDFs overlap. The most prominent peak of the measurement is the thermal neutron peak (see section 5.2.4). Since for the simulated energy range, the thermal neutrons are statistically underrepresented (see section 7.1), a second simulation with only thermal neutrons is included in the deconvolution with an additional PDF H'_{th}.
To deconvolve the spectrum, all generated PDFs are fitted to the measured energy spectrum. For this purpose, each PDF is weighted and summed by a factor f_i. f_i is varied for each PDF according to the minimization of the chi-squared of the measured and simulated data. To account for the measured detector resolution σ, the spectrum is also smeared by a Gaussian factor with $\sigma = 20$ keV. The information about the weighting f_i is correlated with the original neutron flux S_i. In other words, f_i indicates how often the PDF H_i' has to be added to fit the measured data. S_i can be calculated with

$$S_i = n_i/N_i \cdot f_i \cdot f \tag{6.8}$$

with n_i the number of simulated neutrons in the energy bin i, N_i the normalization factor of the PDF H_i', f an additional normalization factor which

includes the measurement time, and the surface of the simulated sphere. In the following, the first method is named Elastic Only Method, and the second Fit Method. The measured spectrum unfolds are described in chapters 7.1 and A.2.

Chapter 7

Result and Discussion of the Unfolding

A little-known background for cryogenic experiments is the neutron background. In particular, the neutron background in the experimental volume often needs to be better studied. It can be very different from the spectrum in the laboratory due to the generation and attenuation of neutrons in the experimental environment. Understanding these backgrounds is becoming increasingly crucial as detector development moves toward lower thresholds and backgrounds. Therefore, neutron scattering from lower energy neutrons is becoming detectable. In experiments with no or low overburden, muons can also be essential in producing an additional neutron background. In this section, the deconvolution of the muon-induced initial neutron energy spectrum in the underground laboratory in Garching is described according to the methods described in chapter 6. Finally, the implications of the results are discussed.

7.1 Muon-Induced Neutron Spectrum

With the measurement described in chapter 4 and the simulation presented in the previous chapter 6, an initial neutron spectrum is calculated. The input spectrum used for the calculations is shown in figure 5.19 in section 5.2.4 and is again presented in figure 7.1.

During the neutron capture process, an α and a tritium particle are released, depositing their energy in the crystal. But also αs from radioactive contaminations are present in the measurement. Due to the light yield, particle discrimination on an event-by-event basis is possible. However, the α and α-tritium bands are very close to each other and overlap. Efficient discrimination is not possible in this case. Though, since αs from radioactive contaminations are not muon-induced events, they can be discriminated by the muon veto coincidence measurement. Therefore, the great benefit of the

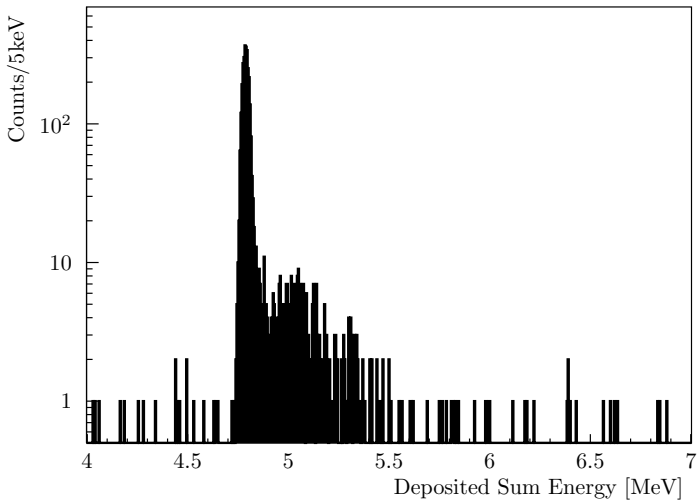

Figure 7.1: Measured energy spectrum after muon veto coincidence cut with the long window in the energy range between 4 MeV and 7 MeV. For the following calculations, this spectrum is used.

coincidence measurement is the reduction of the alpha background. For the analysis, two coincidence windows are applied. A short one of 85 μs and a long window of 1 ms. The short window tags the prompt events, whereas the long window is selected to be short enough not to be dominated by random coincidences but long enough to be sensitive to delayed muon-induced events.

Short Coincidence Window:
First, the 5σ coincidence window (short window) of 85 μs is applied to the data. Figure 7.2 shows the energy spectrum of neutron capture events in this time window. The events coincident with the muon veto are shown in gray, and events not are shown in red. The histogram shows that about one-third of the neutrons in the neutron capture peak at 4.78 MeV are coincidental with the veto. Moreover, most of the higher energy parts of the spectrum (slow and fast neutrons) also coincide with the selected short window. This means that the origin of these events must be in the surrounding material of the cryostat. The neutron capture occurs immediately after the interaction of the muons with the surrounding material.
A distinct peak at 5.3 MeV is observed, which does not coincide with the muon veto. These events are classified as external ^{210}Po contamination. The decay of ^{210}Po is represented by the following equation:

$$^{210}\mathrm{Po} \rightarrow {}^{206}\mathrm{Pb}(103\,\mathrm{keV}) + \alpha(5.3\,\mathrm{MeV})$$

A decay of ^{210}Po sufficiently close to surfaces leads to a release of the full alpha particle energy of 5.3 MeV, whereas the daughter nuclide can escape. The contamination can originate from two main sources. First, surface contamination of the surrounding material or the crystal itself. And, second, the crystal holding. Bronze clamps, similar to the holding of CRESST-II detectors, hold it. Contamination with ^{210}Po was observed too and is, therefore, a well-known background [153].

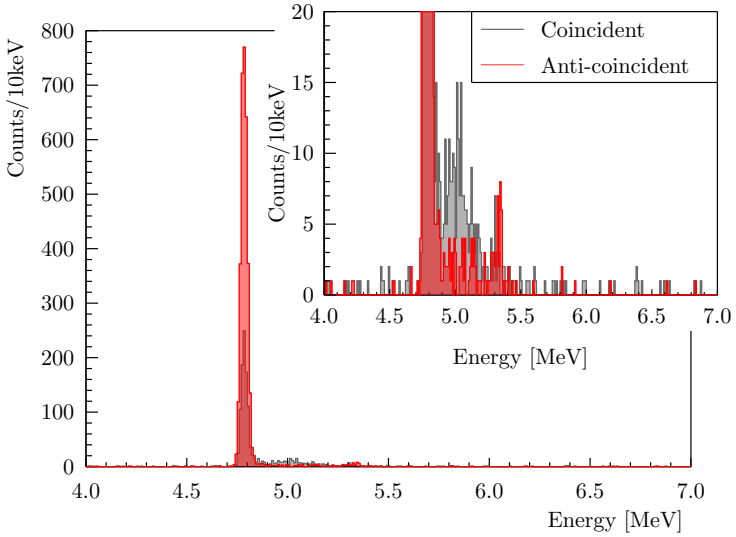

Figure 7.2: Energy spectrum of all assigned neutron captures separated into coincident and anti-coincident events according to short coincidence window (short window) as shown in figure 5.18. *Grey*: Coincident events. *Red:* Anti-coincident events. The analysis shows that about one-third of the neutron captures in the peak are in coincidence with the muon veto. At higher energies, most of the neutrons are in coincidence with the muon veto, indicating that these captures occur close to the muon interaction. There are no processes involved that result in delayed neutron captures in the crystal, such as scattering within the setup. Additionally, a peak at 5.3 MeV is observed, representing events that are not in coincidence and can be attributed to external contamination from ^{210}Po.

Long Coincidence Window:
The application of the larger coincidence window of 1 ms, as shown in Figure 7.3, allows the identification of neutrons that are not immediately captured. Nevertheless, these neutrons are still muon-induced but with a delayed capture. The spectrum shows that two-thirds of the neutrons in the thermal neutron capture peak are coincident with the muon veto. Neutrons with non-thermal energies can scatter strongly in the experimental setup before they

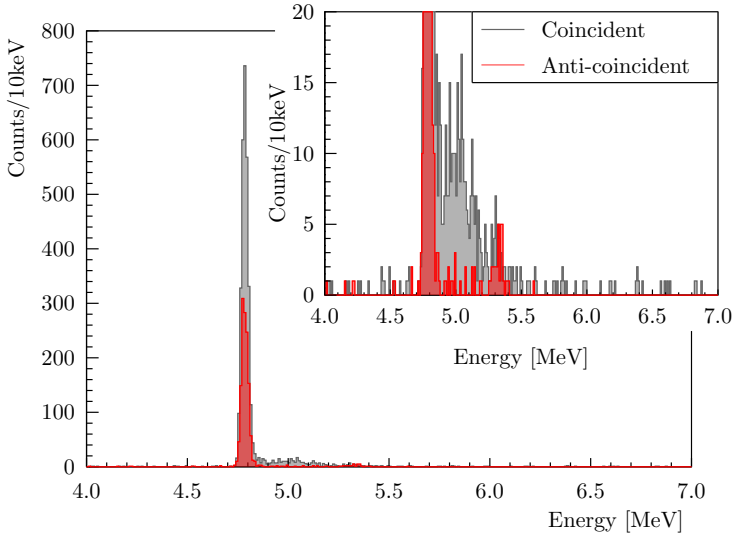

Figure 7.3: Energy spectrum of all assigned neutron captures separated into coincident and anti-coincident events according to long coincidence window (long window) as shown in figure 5.18. *Grey*: Coincident events. *Red:* Anti-coincident events. About two-thirds of the thermal neutron capture events and nearly all of the neutrons at higher energies are in coincidence with the muon veto, as determined using the long time window. The rise in the thermal peak results from muon-induced neutrons with non-thermal energy undergoing scattering and thermalizing in the volume before they are ultimately captured in the crystal. Furthermore, the cross-section for capture increases exponentially as the neutron energy decreases, making capture more likely at lower energies. There is also a peak at 5.3 MeV, which represents events that are not in coincidence with the muon veto (large time window) and are assigned to external contamination of ^{210}Po.

are thermalized and captured in the phonon detector. In addition, the lower the neutron energy, the exponentially increasing the effective cross-section. Capture becomes more likely the lower the neutron energy.
Moreover, the peak at 5.3 MeV is still not coincidental with the muon veto. This confirms the statement of an external ^{210}Po contamination releasing alphas with an energy of 5.3 MeV. A total of $(23.5\pm2.94)\cdot10^{-1}$ counts/keV/kg/day is measured in anticoincidence. This results in a ^{210}Po contamination of $(2.70 \pm 0.34) \cdot 10^{-1}$ mBqkg^{-1}. Using the anticoincidence spectrum with the large coincidence window of 1 ms, upper limits can be obtained for alphas of the natural decay chains ^{232}Th, ^{235}U, and ^{238}U with maximum activities of $< 2.08 \cdot 10^{-2}$ mBqkg^{-1} for ^{232}Th and ^{238}U and $1.70^{+3.30}_{-1.25} \cdot 10^{-2}$ mBqkg^{-1} for the decay of ^{235}U (90 % C.L.). A more detailed discussion of the alpha background can be found in the appendix A.1.

Using the two coincidence windows, a neutron flux is calculated for sub-keV neutrons. A total of 2931 counts for the long 1 ms window and 977 counts for the short window are measured in the thermal and epithermal neutron capture peak coincidence with the muon veto. For the long coincidence window, 24 % of the additional coincidence counts are expected to be random coincidences. Therefore, 2462 counts can be associated with muon-induced thermal neutrons, with neutrons generated within the experimental setup of the UGL cryostat. The resulting measured thermal neutron rate in the 100 g LiF crystal is given by 7.54 ± 0.15 n/h.
In chapter 6, a simulation with a 100 g cylindrical lithium fluoride crystal as used in this measurement is presented. In the simulation, the lithium fluoride neutron reaction is studied, and two methods for deconvolution of the initial neutron spectrum are described.

7.1.1 Method 1: Elastic Only

The first method (elastic-only method) considers all elastic neutron scattering with a final neutron capture process. Therefore, inelastic processes before a neutron capture are all neglected. A detailed description of the method

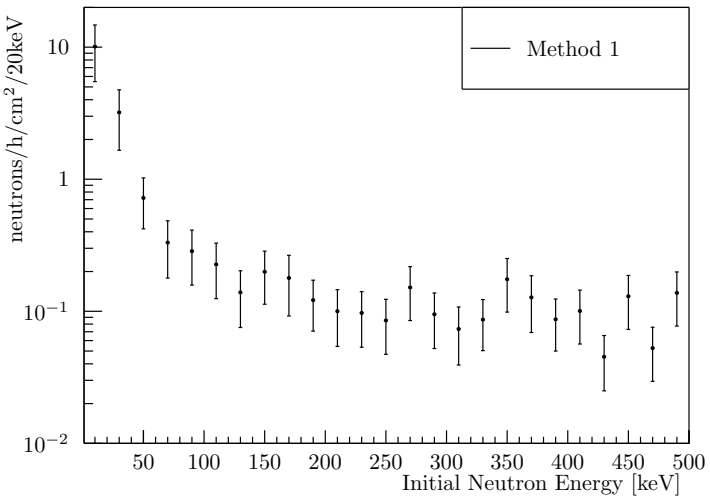

Figure 7.4: Unfolded neutron spectrum up to 500 keV incident neutron energy applying method 1. All inelastic scatterings are neglected. The energy scale is binned in 20 keV steps. Errors are statistical only. Above energies of 100 keV the spectrum is slightly decreasing, whereas the spectrum shows a steep rise for lower energies with a maximum of $(10.1 \pm 4.6)\,\mathrm{h}^{-1}\mathrm{cm}^{-2}(20\mathrm{keV})^{-1}$ in the lowest energy bin.

can be found in the 6.2.3 section. The transfer from the measured to the initial neutron energy spectrum can be simplified to a simple one-to-one correlation. Thus, a measured event with a summed energy x implies an initial neutron energy of $x - 4.78\,\mathrm{MeV}$. Figure 7.7 shows the deconvolved spectrum for the first method according to equation 6.7, including the statistical errors. The chosen bin width corresponds to the detector resolution of 20 keV. The spectrum is slightly decreasing for energies above 100 keV. For lower energies, the spectrum shows a steep increase up to $(10.1 \pm 4.6)\,\mathrm{h}^{-1}\mathrm{cm}^{-2}(20\mathrm{keV})^{-1}$ in the lowest energy bin.
Figure 7.5 shows the simulated initial neutron energy below 10 keV with a binning of 0.01 eV. The figure shows a decrease in simulated events below 100 eV. Events below 1 eV are simulated only with deficient statistics. Neutrons below 1 eV, however, have a drastically increased neutron capture cross section compared to higher energies, and it is known that they are a non-negligible component in the measurement. On average, in the first energy bin ($\sim (0 - 20)\,\mathrm{keV}$), an initial neutron energy of $\sim 10\,\mathrm{keV}$ was simulated with an average effective cross section of $\sim 2.12\,\mathrm{barn}$. This leads to an overestimation and high systematic uncertainty of the neutron flux in at least the three lowest energy bins (below $\sim 60\,\mathrm{keV}$). Thus, it becomes clear that the thermal neutrons must be included and evaluated individually.
The first method is extended by an additional component, a fit of the

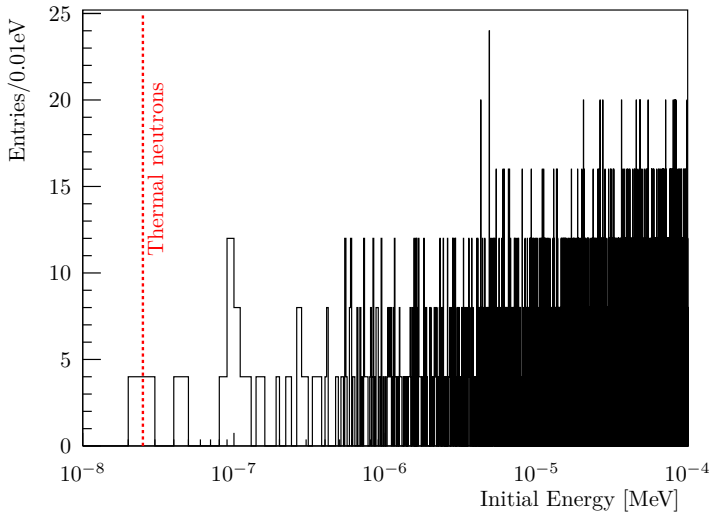

Figure 7.5: Simulated initial neutron energy below 100 eV with a binning of 0.01 eV. The number of simulated neutrons decreases below 100 eV. Thermal neutrons are simulated with a very low statistic. On average an initial neutron energy of $\sim 10\,\mathrm{keV}$ was simulated in the first energy bin ($\sim (0 - 20)\,\mathrm{keV}$) with an average cross-section of $\sim 2.12\,\mathrm{barn}$.

thermal neutron peak, to determine the systematic error. It is assumed that the thermal neutrons are Gaussian distributed. Figure 7.6 (top) shows the measured energy spectrum (black) after the muon veto coincidence cut (long window, see Figure 6.11) in the energy range between 4.7 MeV and 4.86 MeV. To the left of the capture peak, a Gaussian fit is applied (green) with a fixed mean at 4.78 MeV. The fit is compared to the measured energy spectrum (residuals, Figure 7.6 below). According to the residuals, the left part of the peak is well described by the Gaussian fit and thus describes the thermal part of the spectrum very well. Above 4.79 MeV, the discrepancy between fit and data increases, thus the non-thermal component. The calculation by method 1 is repeated, considering the integration of the Gaussian fit.
Figure 7.7 shows the unfolded neutron flux, including the systematic error.

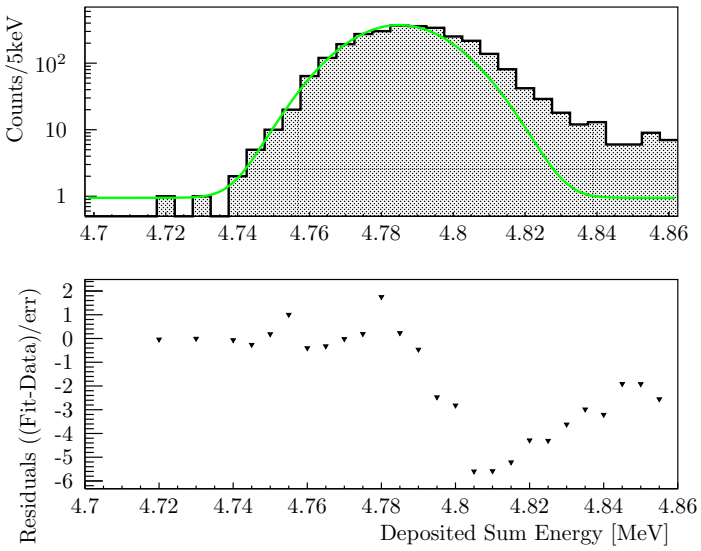

Figure 7.6: *Top:* Measured energy spectrum (black/grey) after muon veto coincidence cut (long window, see figure 7.3) in the energy range between 4.7 MeV and 4.86 MeV. Since the simulation only contains a small number of thermal neutrons, but thermal neutrons are known to be present in the measurement, they have to be evaluated differently. It is considered that thermal neutrons are Gaussian distributed. A Gaussian fit to the left of the spectrum is shown in green. The integral of the Gaussian corresponds to the thermal component. *Bottom:* Residuals (difference of measured data to fit weighted by the error). According to the residuals, the fit works well, and a Gaussian function for the thermal part of the spectrum can describe the peak. The non-thermal component is rising, starting at 4.79 MeV.

The systematic uncertainty is the difference between the flux calculated with method 1 and the flux calculated with the Gaussian fit. Since all neutrons in the peak are assumed to be thermal and because of the large effective

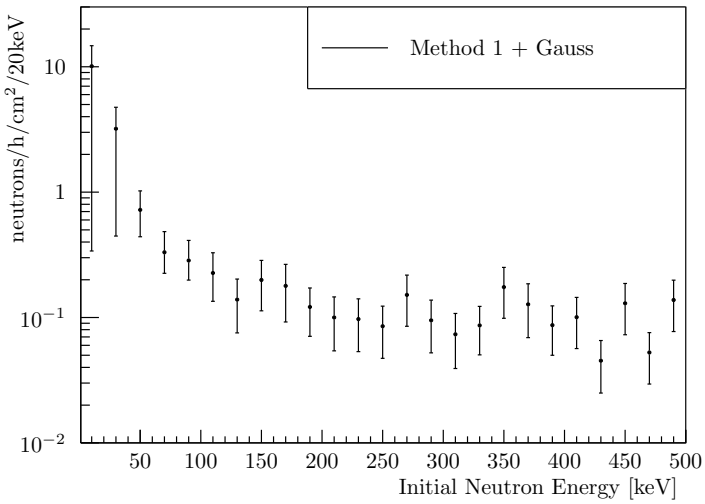

Figure 7.7: Unfolded neutron spectrum up to 500 keV incident neutron energy applying method 1 in combination with a fit of the neutron capture peak. Only neutron capture events with no or n elastic scattering processes are taken into account. All inelastic scatterings before a neutron capture are neglected. The energy scale is binned in 20 keV steps. Statistical uncertainties, as well as systematic uncertainties, are included. In the two lowest energy bins, the systematic error dominates due to the large variation in the neutron capture cross-section. For the lowest energy bin a neutron flux of $(10.1^{+4.6}_{-9.8})\,\mathrm{cm}^{-1}\mathrm{h}^{-1}(20\,\mathrm{keV})^{-1}$ is found.

cross-section of thermal neutrons, the calculation using the Gauss fit represents the minimum possible flux. The flux in the lowest energy bin is calculated to be $(10.1^{+4.6}_{-9.8})\,\mathrm{cm}^{-1}\mathrm{h}^{-1}(20\,\mathrm{keV})^{-1}$. Within the presented measurement, in the energy range up to 500 keV, a total muon-induced neutron flux of $(17.1^{+7.8}_{-14.1})\,\mathrm{cm}^{-1}\mathrm{h}^{-1}(20\,\mathrm{keV})^{-1}$ is found for method 1. Due to the large discrepancy in the neutron capture cross-section, the error in the lowest two bins is huge. An additional method that includes the thermal neutrons and the neutrons with a few keV and weights the two components according to the measured spectrum is needed.

7.1.2 Method 2: Fit Method

Method 1 has shown that the flux in the lowest energy bins depends on the effectively simulated cross-section. The thermal component is simulated with insufficient statistics and must be added when calculating the flux. On the other hand, a complete description of the peak by thermal neutrons seems to underestimate the flux in the lowest energy bins. Therefore, it is necessary

to include the thermal neutrons and the neutrons with a few keV and to fit both components to the measured energy spectrum. The second method (fit method) considers the neutron capture events with inelastic scattering processes and takes a completely different approach. While method 1 calculates the output spectrum directly from the response matrix, method 2 attempts to fit the resulting PDFs of the simulation to the measured spectrum. The advantage of this method is the separation of the contribution of the thermal neutrons to the spectrum. It is even possible to include other contributions, e.g., contributions from α contaminants such as ^{210}Po. As described in section 6.2.3, other processes can occur before the neutron capture at ^{6}Li. Single-elastic, multiple-elastic, and inelastic scattering at ^{6}Li, ^{7}Li, and ^{19}F are possible, with inelastic scattering at ^{19}F being the dominant process. With no scattering or single- and multiple-elastic scattering processes, the deposited sum energy is the initial neutron energy plus 4.78 MeV from neutron capture. If the deposited energy is less than the sum of the deposited energy from the neutron capture process and the initial neutron energy, then inelastic scattering processes occur according to table 6.1 and, in addition, arbitrary combinations of those values. The generated γs mainly escape from the detector with only small energy deposition in the detector. In the simulation performed in this work, the dominant second-order process is found to be Compton scattering, which is evident in the broadening of the emission bands, especially for low-energy lines of 110 keV and 197 keV with initial neutron energies below 1 MeV. The simulation showed that the energy deposition in the crystal by gammas is smaller than 100 keV. Due to the phonon light technique used in the experiment, the additional light is measured according to the light yield. The normalized luminous efficiency for the alpha/tritium band was adjusted to a value of 0.23, while events in the electron/gamma band are defined as light yield 1. According to these values, an event with a deposited sum energy around 5 MeV and a shift in the light yield of at most 0.015 is expected for an energy deposition of 100 keV by gammas. This change is too small to distinguish from neutron capture events where only elastic scattering processes occur. Therefore, the phonon light technique does not exclude these events and must be considered in the deconvolution.

Further, the light detector could detect the gammas created by inelastic scattering. The gammas are not in the visible spectrum and, therefore, are not reflected by the reflecting and scintillating housing. Thus only direct hits in the light detector can lead to an energy deposition and are being vetoed. For geometrical reasons the minimum of detectable gammas are 0.4 % (solid angle of 0.05 sr) and the maximum 1.6 % (solid angle of 0.20 sr). On average, it is expected that 1 % of produced gammas reach the light detector. Given the attenuation length of silicon, [154] only 2 % of gammas with the lowest energy of 110 keV are detected by the silicon light detector. Therefore, the detection efficiency for gammas produced during an inelastic scattering pro-

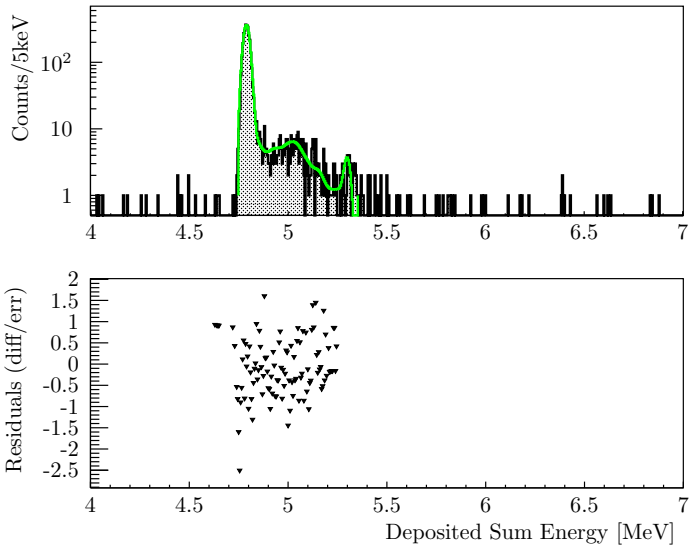

Figure 7.8: *Top:* Measured energy spectrum (filled black histogram) in coincidence with the muon veto (long window). The best-fit model describing the data is shown in green. The selected energy range for the fit is chosen between 4.75 MeV and 5.35 MeV. *Bottom:* Residuals (difference of measured data to fit weighted by the statistical error).

cess is calculated to be $< 0.03\,\%$ and is neglected in the following.

Figure 7.8 (top) shows the measured spectrum in black with the muon veto coincidence cut applied (long window, see figure 7.3) in the energy range between 4 MeV and 7 MeV. The result of the best fit of the simulated data to the measured spectrum is shown in green in the energy range between 4.75 MeV and 5.35 MeV. The energy range is selected from the thermal/epithermal neutron capture peak up to the alpha energy of ^{210}Po. Outside the chosen energy range of 4.7 MeV to 5.3 MeV, the statistics of the measurement are low, and few counts are measured. The fitting is done by minimizing the chi^2 between measurement and simulation as described in section 6.2.3. For the chi^2 calculation, the residuals of the fit (difference between observed and measured spectrum divided by the statistical error) are summed. The residuals for each energy bin are shown in Figure 7.8 at the bottom. Figure 7.9 plots the distribution of the calculated residuals. The spectrum has a Gaussian shape around zero. Thus, the spectrum is well described by the fit.

With the best-fit result shown in Figure 7.10, the initial neutron energy for muon-induced neutrons is calculated according to the equation 6.8 in Section 6.2.3. The result of the fit, and thus the neutron flux as a function of the incident neutron energy, is shown in figure 7.10 in black for method 2

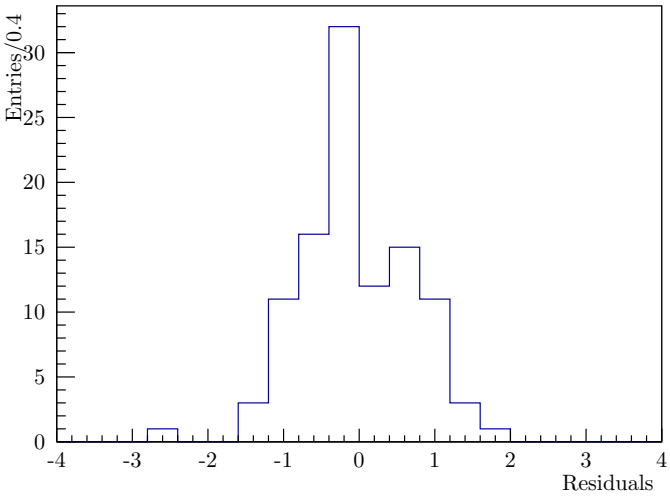

Figure 7.9: Histogram of the residuals from the fitted spectrum to the data (see figure 7.8). The shape is Gaussian-like around zero, indicating that the fit applied can well describe the spectrum.

and, in comparison, the result of the fit with method 1 in red. The incident neutron energy is divided in 20 keV steps between 0 keV and 500 keV. As described in section 6.2.3, the second simulation, where only thermal neutrons are simulated (see section 6.1.2), is used to resolve the thermal neutron peak, which turns out to be the dominant component of the measured energy spectrum. The result represents the best-fit values, including the statistical errors. The marker is located in the middle of the energy bin. Due to the underrepresentation of thermal neutrons in method 1, the first energy bins are overestimated. On the other hand, an additional Gaussian fit in combination with method 1 appears to underestimate the neutron flux in the first energy bin. The unfolded flux for the lowest energy class gives a value of $(7.0 \pm 0.3) \cdot 10^{-1}\,\mathrm{cm}^{-1}\mathrm{h}^{-1}(20\,\mathrm{keV})^{-1}$, which is within the errors of method 1. The calculated values are not within the 1σ errors for the second and third energy bins. This effect is due to the inelastic scattering processes that are not considered. As described in chapter 6, method 2 includes an additional simulation for the thermal neutron peak, while method 1 does not. Neutron events with an initial energy of x_1 can reduce their energy to the energy x_2 by inelastic scattering processes. These neutrons can then be captured by a ^{6}Li nuclide. When measured, they are detected as neutrons with energy x_2 rather than their original energy x_1. The lower energy bins are therefore overestimated. This is not the case in method 2, so the discrepancy occurs in the second and third energy bins. For energies above the 50 keV bin, the spectra show a very similar shape within the errors. For method 2, a total

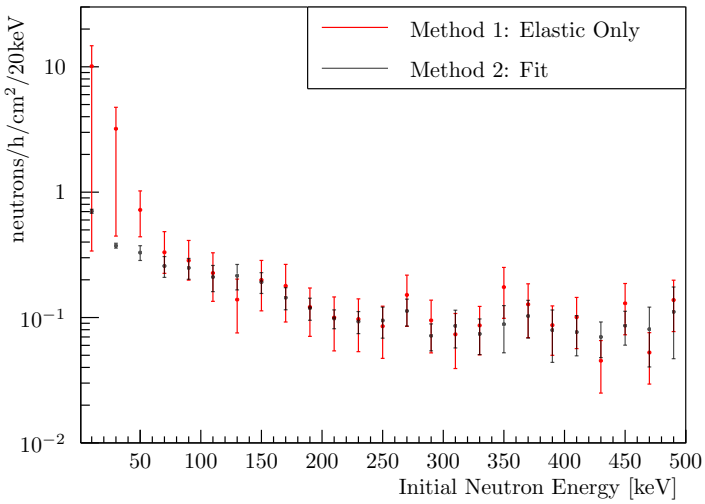

Figure 7.10: Comparison of neutron flux as a function of the initial neutron energy for muon-induced neutrons. *Black*: Unfolding with method 2 (Fit Method). The energy is binned in 20 keV steps between 0 keV and 500 keV (right). Since for thermal neutrons, single energy of 0.025 eV was simulated to resolve the neutron peak. The unfolded flux for the lowest energy bin gives a value of $(7.0 \pm 0.3) \cdot 10^{-1}\,\mathrm{cm}^{-1}\mathrm{h}^{-1}(20\,\mathrm{keV})^{-1}$. The result represents the best-fit values and includes statistical errors. The marker is placed in the center of the energy bin. *Red*: Unfolding with method 1 (Elastic Only Method). Only neutron capture events with no or multiple elastic scattering processes are considered. Statistical and systematic errors are included. With method 1, a neutron flux for the lowest energy bin is calculated to be $(10.1^{+4.6}_{-9.8})\,\mathrm{cm}^{-1}\mathrm{h}^{-1}(20\,\mathrm{keV})^{-1}$. Chapter 6 describes the method 2 unfoldings and includes an additional simulation for the thermal neutron peak. In method 1, the thermal neutrons are underrepresented, leading to an overestimation in the first energy bins. An additional Gaussian fit in combination with method 1 seems to underestimate the neutron flux in the first energy bin. Method 1 includes statistical and systematic errors. For the lowest energy bins, the systematic error is dominating. Method 2 considers statistical errors only, and the systematic error could not be accessed. The systematic error in method 2 can be in the same range as the systematic error in method 1. Therefore, the two methods should be perceived as comparable in terms of precision.

neutron flux of $(4.2 \pm 0.8)\,\mathrm{cm}^{-1}\mathrm{h}^{-1}(20\,\mathrm{keV})^{-1}$ up to 500 keV is found, which is consistent with the total flux of method 1. Method 1 and Method 2 differ in their approach to potential sources of error, with Method 1 accounting for both statistical and systematic errors, while Method 2 considers only statistical errors. For the lowest energy bins, the systematic error in Method 1 is significant relative to the statistical error. Conversely, Method 2 only accounts for statistical error and cannot access the systematic error. Notwithstanding, the systematic error in Method 2 may still fall within the same range as that of Method 1. As such, both methods should be regarded as roughly equivalent in terms of precision. A comparison of the results for the deconvolution of the original neutron spectrum with method 1 (elastic only) and method 2 (fit) is shown in Table 7.1. The results show that the errors of the unfolding can be reduced with a simulation compared to a simple back-calculation with the cross-section of the capture process.

Energy bin	Flux Method 1 $[h^{-1}cm^{-2}(20keV)^{-1}]$	Flux Method 2 $[h^{-1}cm^{-2}(20keV)^{-1}]$
10 keV	$10.10^{+4.62}_{-9.76}$	0.70 ± 0.03
30 keV	$3.20^{+1.55}_{-2.76}$	0.37 ± 0.02
50 keV	$0.72^{+0.30}_{-0.28}$	0.33 ± 0.04
70 keV	$0.33^{+0.15}_{-0.11}$	0.26 ± 0.05
90 keV	$0.28^{+0.13}_{-0.09}$	0.25 ± 0.05
110 keV	$0.23^{+0.10}_{-0.09}$	0.21 ± 0.05
130 keV	$0.14^{+0.06}_{-0.06}$	0.22 ± 0.05
150 keV	$0.20^{+0.09}_{-0.09}$	0.19 ± 0.04
170 keV	$0.18^{+0.09}_{-0.09}$	0.14 ± 0.03
190 keV	$0.12^{+0.05}_{-0.05}$	0.12 ± 0.02
210 keV	$0.10^{+0.05}_{-0.05}$	0.10 ± 0.02
230 keV	$0.10^{+0.04}_{-0.04}$	0.09 ± 0.02
250 keV	$0.09^{+0.04}_{-0.04}$	0.09 ± 0.03
270 keV	$0.15^{+0.07}_{-0.07}$	0.11 ± 0.03
290 keV	$0.09^{+0.04}_{-0.04}$	0.07 ± 0.02
310 keV	$0.07^{+0.03}_{-0.03}$	0.09 ± 0.03
330 keV	$0.09^{+0.04}_{-0.04}$	0.07 ± 0.02
350 keV	$0.17^{+0.08}_{-0.08}$	0.09 ± 0.04
370 keV	$0.13^{+0.06}_{-0.06}$	0.10 ± 0.03
390 keV	$0.09^{+0.04}_{-0.04}$	0.08 ± 0.04
410 keV	$0.10^{+0.04}_{-0.04}$	0.08 ± 0.03
430 keV	$0.05^{+0.02}_{-0.02}$	0.10 ± 0.03
450 keV	$0.13^{+0.06}_{-0.06}$	0.09 ± 0.03
470 keV	$0.05^{+0.02}_{-0.02}$	0.08 ± 0.04
490 keV	$0.14^{+0.06}_{-0.06}$	0.11 ± 0.06
Total:	$17.1^{+7.8}_{-14.1}$	4.2 ± 0.8

Table 7.1: Results for the unfolding of the initial neutron spectrum with method 1 (elastic only) and method 2 (fit). Method 1 includes statistical and systematic errors, whereas method 2 considers statistical errors only. The systematic error of method 2 could not be accessed and can be in the same range as the systematic error in method 1. The two methods are comparable in terms of precision.

7.2 Discussion and Impact of Results

The following discussion about limiting factors and perspectives of the measurement is presented. Further, the impact of the results for the Dark Matter experiment CRESST as well the coherent neutrino-nucleus scattering experiment NUCLEUS is discussed.
In recent years, the development of cryogenic detectors has focused on lowering thresholds and, thus, increasing detection sensitivity. The CRESST experiment, for example, achieves thresholds down to 30.1 eV and is a leader in the low-mass dark matter field. At such low thresholds, the detectability of lower energy neutrons must be considered. The maximum energy transferred in a head-to-head collision can be determined with

$$E_R^{max} = 4\frac{m_n \cdot m_N}{(m_n + m_N)^2} E_n \tag{7.1}$$

where m_n is the mass of the incident neutron, m_N is the mass of the nucleus, and E_n is the energy of the incident neutron. $CaWO_4$ crystals are mainly used for the CRESST experiment. Figure 7.11 shows the maximum transferred energy of a neutron to one of the three isotopes oxygen (O_2, blue), calcium (Ca, green), and tungsten (W, red) as a function of the incident neutron energy. A typical threshold for a standard CRESST detector is in the range of 50 eV and is highlighted in black in the figure. Neutrons with energies of > 200 eV are a possible background for the CRESST experiment. Compared to the measurement presented in this work, neutrons in the first energy bin already contribute to a potential background, while thermal neutrons do not.
Muon-induced neutrons can be an extensive background for above-ground or shallow underground experiments only where the muon rate is sufficiently high. The CRESST experiment is located in the laboratori nazionali del Gran Sasso (LNGS) with ~ 3300 m.w.e.. There, a muon-flux was measured of $(3.31 \pm 0.03) \cdot 10^{-4}\,\mathrm{m^{-2}s^{-1}}$ [155] which is six orders of magnitude lower than above ground. Therefore, muon-induced neutrons play a subdominant role in the creation of neutrons. Table 7.2 shows a compilation of former neutron flux measurements in the underground laboratory below the Gran Sasso massive. The measured flux of the thermal part of the neutron spectrum varies between $(0.3-1.1) \cdot 10^{-3}\,\mathrm{cm^{-2}h^{-1}}$ [156][157][158], depending on the location the measurement was done. In section 7.1.2, the neutron flux for muon-induced neutrons is calculated to be $(2.7 \pm 0.2) \cdot 10^{-1}\,\mathrm{cm^{-2}h^{-1}}$ for the thermal component of the spectrum and a total flux of $(4.0 \pm 0.2)\,\mathrm{cm^{-1}h^{-1}(20\,keV)^{-1}}$ up to 500 keV. In section A.2, the flux of all measured neutrons is calculated using method 2 as described before. Figure 7.1 is used as input spectrum but without subsequent muon veto cut. There, a total flux of $(5.62 \pm 0.93)\,\mathrm{cm^{-1}h^{-1}(20\,keV)^{-1}}$ to 500 keV and a neutron flux of $(1.71 \pm 0.04)\,\mathrm{cm^{-1}h^{-1}(20\,keV)^{-1}}$ in the first energy bin are calculated. The measurement in Hall A [156] shows

Energy Range in MeV	Neutron flux in $10^{-6}\,\mathrm{cm}^{-2}\mathrm{s}^{-1}$				
	[156]	[157]	[158]	[160]	[161]
$0 - 50 \cdot 10^{-9}$	1.08(2)	0.54(13)	0.32(13)		
$50 \cdot 10^{-9} - 10^{-3}$	1.84(20)				
$10^{-3} - 1$	0.54(1)				
$1 - 2.5$				0.14(12)	
$2.5 - 5$	0.27(14)			0.13(4)	0.78(3)
$5 - 10$	0.05(1)			0.15(4)	
$10 - 15$	$6(2)10^{-4}$			$4(4)10^{-4}$	
$15 - 25$	$5(30)10^{-7}$				

Table 7.2: Compilation of several neutron background measurements at different locations in the LNGS (hall A [156], next to hall A [158], hall C [160][161], and between hall A and B [157]). The CRESST experiment is located in hall A.

a value about two orders of magnitude lower than the thermal neutron flux of all measured neutrons. For neutrons up to 1 keV, [156] measured a neutron rate of $(6.6 \pm 0.7) \cdot 10^{-3}\,\mathrm{cm}^{-1}\mathrm{h}^{-1}$. Assuming the neutron flux calculated in this work to be constant in the first energy bin, the neutron flux is $(4.5 \pm 0.1) \cdot 10^{-2}\,\mathrm{cm}^{-1}\mathrm{h}^{-1}$ for neutrons up to 1 keV. This value is ten times smaller. At such low fluxes, alpha contamination in the neutron capture peak region must be considered. However, the presented measurement shows shallow alpha contamination in LiF with maximum activities of $< 2.08 \cdot 10^{-2}\,\mathrm{mBqkg}^{-1}$ for ^{232}Th and ^{238}U and $1.70^{+3.30}_{-1.25} \cdot 10^{-2}\,\mathrm{mBqkg}^{-1}$ for the decay of ^{235}U (90 % C.L.). The neutron capture peak, in this case, is expected to be an order of magnitude higher than the alpha background. In [159], the neutron flux within the CRESST setup was simulated by passing a measured neutron spectrum through the CRESST setup. Near the detectors, the flux is in the order of $10^{-5}\,\mathrm{cm}^{-2}\mathrm{h}^{-1}$, and the alpha background is expected to be in the same range as the neutron capture peak. In this case, the αs dominate, and reliable measurement is difficult. Nevertheless, with increased light yield, effective discrimination is possible. The LiF neutron monitor is, therefore, a promising tool for in situ measurement of the neutron background in the CRESST facility and can provide important information for the simulation team.

NUCLEUS aims to detect coherent-neutrino nucleus scattering (CEνNS), which would open the door for new physics within and beyond the Standard Model of Particle Physics. NUCLEUS is an under-construction neutrino experiment at the Chooz (France) nuclear power reactor that allows for precision measurements with cryogenic gram-scale detectors based on CRESST technology. The design goal for the experiment is a threshold below 20 eV with $CaWO_4$ and Al_2O_3 detector arrays. For such experiments, the muon-

induced background becomes highly relevant since they are only located at $\sim$ 3 m.w.e.. With a threshold of 10 eV NUCLEUS would become sensitive to neutrons with energies of $\sim$ 90 eV for $CaWO_4$ and Al_2O_3. A well-known neutron background is, therefore, crucial for the experiment. Simulations of the expected background in the NUCLEUS experiment showed that atmospheric neutrons with energies above 10 MeV could cause secondary neutrons of 1 MeV due to spallation reactions in the lead layer of the shielding. The PE and the Ge of the shielding slow down those neutrons. They reach the detectors with energies below 10 keV and produce recoils in the region of interest of NUCLEUS between 10 eV and 100 eV [162]. For NUCLEUS, it is important to measure the neutron flux below 10 keV. Plans in the near future of NUCLEUS foresee a measurement with the neutron monitoring system developed in the framework of this thesis. This measurement has the potential to deliver a robust background model for the NUCLEUS experiment.

As mentioned earlier, the results shown in this chapter have some limitations

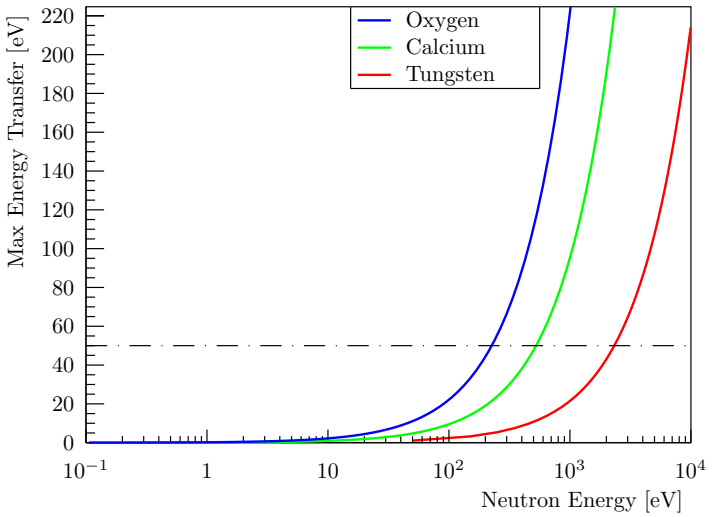

Figure 7.11: Maximum energy a neutron transfers by a head-to-head collision with a nucleus (Oxygen in blue, Calcium in green, and Tungsten in red) in a $CaWO_4$ crystal. The black dashed line indicates the detection threshold of a standard CRESST detector with $\sim$ 50 eV. To transfer a detectible amount of energy, a minimum initial neutron energy of 200 eV is needed.

and should be taken as proof of principle for the method developed in this thesis. First, the separation of neutron capture and alpha events needs to be improved. Since neutron capture releases a tritium atom in addition to the alpha atom, the light yield is different from that of alpha. Due to the

low light output of lithium fluoride in combination with a non-optimized light detector, the light yield of the two event classes is very similar. Due to operating temperature constraints in the UGL, a light detector had to be used with a transition temperature above 30 mK. Standard CRESST light detectors are operated around $15 - 20$ mK. The use of such a light detector would already improve the measurement significantly. Further, the light output of the LiF could be increased by doping the crystal with other elements, e.g., Europium (Eu) and Titanium (Ti). However, to be used underground, it is important to keep the level of radiopurity low and not introduce impurities due to the doping process due to impurities in raw materials.
Since the measured energy of the neutron capture peak is in the alpha region, the energy resolution of the unfolded energy spectrum depends on the resolution of the alphas. This work achieves a resolution of 20 keV. However, it was already shown that detectors of this type could reach energy resolutions well below 10 keV[163]. This goal can be achieved by further investigating the detector noise and the thermal sensor. A lower energy resolution would also allow for a better resolution of the initial neutron energy. In particular, in the lowest energy bin, a smaller binning would help for better unfolding results.
Further, a study of the systematic uncertainties of the simulation should be done in the future. For that, the statistic in the measurement and the statistic in the simulation have to be increased. In particular, neutron energies down to thermal neutrons must be included in the simulation. The low statistic in the simulation can be fixed by making some changes in the simulation software ImpCRESST. By now, it is only possible to store a huge amount of information which enlarges the simulation files drastically. A selection of stored parameters would minimize the data files and do a more extended simulation. Work for this is beyond the scope of this thesis.

Chapter 8

Summary and Outlook

The direct dark matter search experiment CRESST (Cryogenic Rare Event Search with Superconducting Thermometers) aims at detecting dark matter (DM) particles by their elastic scattering from nuclei in scintillating $CaWO_4$ single crystals. Each detector consists of a $\sim 25\,\mathrm{g}$ $CaWO_4$ crystal operated as a cryogenic detector at millikelvin temperatures. A particle interaction in the target crystal results in a phonon signal measured by a transition edge sensor (TES) and a light signal detected by a separate cryogenic light detector. The readout of the phonon signal and the light signal enables event-based particle discrimination, which is used for background suppression. This detection principle is referred to as the phonon-light technique. Neutrons are the ultimate and fundamental background for CRESST and other low-threshold experiments worldwide. Since neutrons have no charge, a scattering process results in a signal similar to an expected DM signal. In particular, only passive neutron shielding can be used to attenuate neutrons to energies below the threshold. Active discrimination between neutron scattering events and possible DM events is not possible. However, neutrons, especially muon-induced neutrons, can also be a dangerous background for surface experiments searching for rare events, such as NUCLEUS, which aims to detect coherent neutrino nuclear scattering (CEνNS). Therefore, knowledge of their spectral shape and rate is important for such experiments. During the last DM run of the CRESST experiment, a new background was observed, the so-called Low Energy Excess (LEE), an exponentially increasing signal that cannot be attributed to a specific type of particle interaction. This new background is observed not only by the CRESST experiment but also by other low-threshold cryogenic experiments. Partially, the signal could be related to elastic neutron scattering from epithermal slow and fast neutrons.
In this work, a cryogenic in-situ neutron monitoring system was designed, constructed, and built to measure neutron flux within the experimental volume of cryogenic experiments. The neutron monitor takes advantage of the multi-target phonon light technique, which provides the ability to match the selec-

tion of the target crystal to the physical targets. The operating principle of the detector is based on neutron capture at ^{6}Li ($^6\mathrm{Li} + n \rightarrow \alpha + {}^3\mathrm{H} + 4.78\,\mathrm{MeV}$) in a 100 g cylindrical lithium fluoride (LiF) crystal, which is a weakly scintillating material. Lithium fluoride is a well-suited material for a neutron monitor because it contains a lot of lithium ($\sim 27\,\%$), and large single crystals with low radioactive contamination are commercially available. To distinguish neutron events from background events, e.g., electron/gamma events or alphas, the scintillation light is read out from a special cryogenic light detector made of silicon.

To test the LiF neutron monitor, a particular cryogenic setup was realized in this work. An experimental setup based on a ^{3}He-^{4}He dilution refrigerator with a base temperature of 10 mK was built in the shallow underground laboratory in Garching (UGL). Three new SQUIDs were added to the experimental setup, and the readout electronics were optimized. An active muon veto with a near 4π coverage was added and synchronized with the cryogenic data acquisition.

A four-month measurement campaign was conducted with the realized LiF detector. The campaign consisted of a three-month background run and a one-month calibration run with a ^{147}Sm alpha source. In this work, the data set was thoroughly evaluated to measure the neutron capture spectrum and calculate the energy-dependent initial neutron flux. The result shows that the neutron capture events can obtain a measured neutron energy spectrum. In addition, two contributions to the neutron flux in the UGL facility were found: Ambient neutrons and muon-induced neutrons in the cryogenic setup itself. With the muon veto, it was possible to distinguish between the two sources. The muon-induced neutrons could serve as a perfect benchmark scenario for the neutron monitor. Most neutrons are expected to be induced by cosmic muons within the cryostat shielding (Pb) through spallation. They, therefore, are consistent with the muon veto, as opposed to non-muon-induced events such as alphas or ambient neutrons. For the LiF detector 100 g, a muon-induced neutron rate of 7.54 ± 0.15 n/h was measured and, for the first time, an initial neutron energy spectrum in the cryogenic UGL setup was calculated by back-calculation with the energy-dependent effective cross-section of the neutron capture process.

The initial neutron spectrum was deconvolved from the measured neutron energy spectrum to obtain a more accurate value and reduce systematic errors. For this purpose, a special simulation was developed to study the neutron reaction in lithium fluoride, taking into account multiple scattering and inelastic processes in the detector, as opposed to the simple capture cross-section. Using the Geant4 and ImpCRESST simulation software tools, a 100 g LiF crystal was implemented within a vacuum sphere. A flat neutron spectrum between 0 MeV and 3 MeV was isotropically shot onto the crystal. The simulation showed that most of the neutrons underlie single or multiple scattering processes. Some of the neutrons are then captured

by ^{6}Li. It was shown that the LiF module is most sensitive to initial neutron energies below 500 keV. In the case of multiple processes, the sum of the energy deposited by the scattering process and the capture process is detected as a single event in the detector. Two different methods for deconvolution have been presented. The first method considers only elastic scattering processes in combination with neutron capture. It is calculated via matrix inversion, while the second method also considers inelastic scattering processes and the simulation is fitted to the measured data. The simulation results were applied to the measured data and provided for the first time an energy characterization of the neutron background of the cryogenic setup in the UGL with neutron fluxes of $(10.1^{+4.6}_{-9.8})\,\mathrm{cm}^{-1}\mathrm{h}^{-1}(20\,\mathrm{keV})^{-1}$ (method 1) and $(7.0 \pm 0.3) \cdot 10^{-1}\,\mathrm{cm}^{-1}\mathrm{h}^{-1}(20\,\mathrm{keV})^{-1}$ (method 2) in the lowest energy bin. Method 1 considers both statistical and systematic errors, with a dominating systematic error. In contrast, method 2 cannot evaluate systematic error but only statistical error but may still fall within the range of method 1's systematic error. Method 1 and method 2 give total neutron fluxes of $(17.1^{+7.8}_{-14.1})\,\mathrm{cm}^{-1}\mathrm{h}^{-1}(20\,\mathrm{keV})^{-1}$, and $(4.2 \pm 0.8)\,\mathrm{cm}^{-1}\mathrm{h}^{-1}(20\,\mathrm{keV})^{-1}$ up to 500 keV are found. This is the first characterization of the muon-induced neutron background and a first deconvolution of a cryogenically measured neutron spectrum. This is proof of principle for developing a neutron monitor based on the technology presented in this work.

Nevertheless, there is room for improvement. First, the separation of neutron capture and alpha events needs to be improved. To do this, the light output of the LiF could be increased. A common method is to dope the crystal with other elements, e.g., europium (Eu) and titanium (Ti). In addition, the performance of the light detector can be improved. The light detector used in this work has a relatively high critical temperature of 34 mK due to the limitations of the cryostat. Lowering the transition temperature would result in better performance. In addition, the TES design itself can be optimized for this measurement. In addition, due to the low statistics of the simulation for initial neutron energies in the sub-keV energy range and too low statistics on the experimental side, no statistical analysis could be performed. The best-fit value was chosen for the initial neutron spectrum estimate. A solution for the low statistics in the simulation could lie in major changes in the data storage of the simulation software ImpCRESST. Currently, storing a large amount of information is only possible by drastically increasing the simulation files' size. A selection of stored parameters would help to minimize the amount of data and perform a more comprehensive simulation. Work in this regard is already proceeding.

In particular, a measurement with this detector as part of the CRESST experiment will provide valuable input to the CRESST experiment simulation team. With the result, it would be possible to decipher the neutron fraction from the LEE background. The result presented in this work is relevant to all experiments searching for signals induced by nuclear recoils. With

the understanding and monitoring of the neutron background, experiments searching for rare events can drastically benefit their sensitivity. The detector principle developed in this work will be a powerful tool for characterizing the neutron background in cryogenic direct DM experiments (such as CRESST) and other experiments searching for rare events influenced by the neutron background, such as coherent neutrino nuclear scattering (CEνNS). Understanding and monitoring the neutron background can significantly impact rare event search experiments to improve sensitivity.

Appendices

Appendix A

Alpha and Neutron Background in the UGL

In the scope of this thesis, it was possible to discriminate muon-induced neutron events from other backgrounds like alphas and other neutron sources. Nevertheless, it is crucial to understand these different backgrounds. Alphas are harmful in this sense for two reasons. First, they release energies in the range of the neutron capture of ^{6}Li. And second, there can be an additional neutron background due to (α, n) reactions. In the following, an estimation of the alpha background is described. In addition, neutrons originating from the walls and environment are taken into account, and a neutron spectrum of all neutrons in the UGL is shown.

A.1 Alpha Particle Discrimination

The presence of alpha particles due to radioactive decay chains can be a harmful background in the region of interest. Lithium-fluoride is a very clean material just by the rules of crystal growth. The LiF material contains only light elements, lithium, and fluorine. Therefore, the amount of heavy atoms brought inside the crystal lattice is small compared to other crystal materials, e.g., $CaWO_4$. For completeness, an evaluation of the alpha background is presented in the following.

The discrimination between alpha events and alpha/tritium events is, in principle, possible by comparing the light yields of these two event classes. Due to the additional tritium in the capture process, more energy is released in the light channel for a capture process than for an alpha event. Figure A.1 shows the normalized light yield plot for the background measurement of run22. In addition, the band for all three event classes, the electron/gamma, alpha, and alpha/tritium bands, are drawn. For the alpha band, the alpha measurement run23 is used. The light yield is normalized for both run22 and run23 in the same way. The light yield of the electron/gamma band between

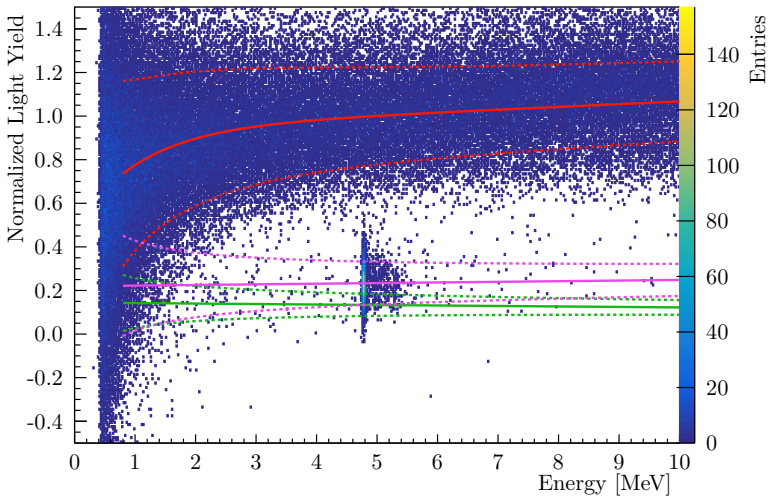

Figure A.1: Normalised light yield for the background measurement of run22. In addition, the band for all three event classes, the electron/gamma, alpha, and alpha/tritium band, are drawn. For the alpha band, the alpha measurement run23 is used. The light yield is normalized for both run22 and run23 in the same way. The light yield of the electron/gamma band between 4 MeV and 6 MeV is selected, and a gaussian is fitted to both spectra. The mean value is referred to be 1. Since the noise conditions are comparable, it is assumed that the light yield is the same for both measurements.

4 MeV and 6 MeV is selected, and a gaussian is fitted to both spectra. The mean value of the electron/gamma band is normalized to 1. Since the noise conditions are comparable, the light yield is assumed to be the same for the same class of events for both measurements. Figure A.1 shows a large overlap of the alpha band with the alpha/tritium band. Discrimination between alphas and the alpha/tritium band events is, therefore, not sufficient. The increased light output of the crystal and a further optimized light detector are necessary to distinguish the two event classes successfully in the future. Nonetheless, a calculation is presented to estimate the alpha background. The activity of a decaying radioactive isotope is given by

$$A = -\frac{dN}{dt} = \lambda N_0 e^{-\lambda t} \tag{A.1}$$

where N_0 is the original number of nuclei of the isotope, the decay constant $\lambda = \frac{ln(2)}{t_{1/2}}$ and the half-life $t_{1/2}$ for the decaying isotope [164]. This equation is valid for a single decaying radioactive source. For a chain of two decays, equation A.1 changes to

$$\frac{dN_B}{dt} = -\lambda_B N_B + \lambda_A N_{A0} e^{-\lambda_A t} \tag{A.2}$$

where nuclei A decays to nuclei B and B finally to C (A $\rightarrow$ B $\rightarrow$ C). The decay of A increases the number of B since A decays into B before B decays into C. In other words, the number of nuclei B increases due to the decay of nuclei A and decreases due to its own decay into nuclei C [164]. In nature, all materials are contaminated with radioactive material following the three natural decay chains of ^{232}Th, ^{235}U, and ^{238}U. Due to the shorter live time of daughter nuclei with respect to the mother nuclei, these three decay chains are in equilibrium, meaning that the activity for all chain nuclei is the same.

For a further analysis of the alpha decays, the anti-coincidence spectra of figures 7.3 and 7.2 are used since alphas are not expected to be in coincidence with the muon veto. The anti-coincident spectra with the long coincidence window is shown in figure A.2. For radioactive contamination, the three natural decay chains of ^{232}Th, ^{235}U, and ^{238}U are expected to be introduced during crystal growth via the natural contamination of the raw materials. A detailed picture of those decay chains can be found in the appendix B. According to the anti-coincidence spectrum of figure 7.3, only 8 ± 4.5 alpha counts are observed in the energy region between 4.0 MeV and 4.7 MeV. Due to the very low statistics, the statistical analysis of Feldman [165] was used to estimate the activity of the primordial nuclides of the naturally occurring decay chains. The following limits can be set: for ^{232}Th and ^{238}U $< 2.08 \cdot 10^{-2}$ mBq/kg and $1.70^{+3.30}_{-1.25} \cdot 10^{-2}$ mBq/kg for the decay of ^{235}U with 90 % C.L.

Following the decay scheme, some decays could be hidden below the neutron

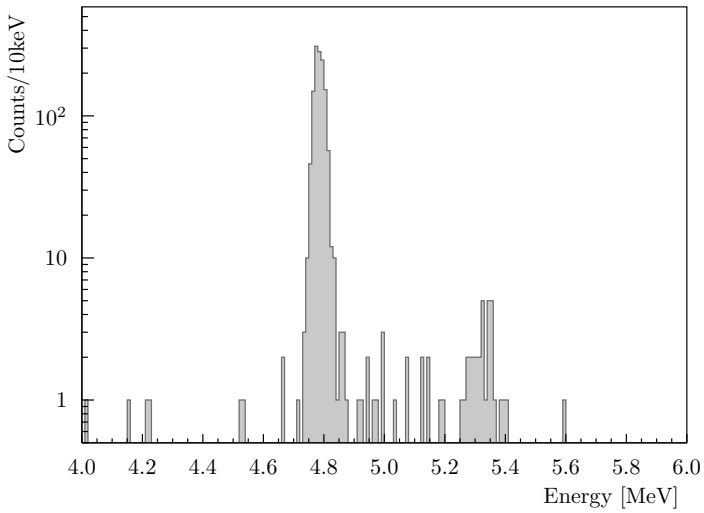

Figure A.2: Energy spectrum of all events which are not in coincidence with the muon veto for a long coincidence window of 1 ms between 4.0 MeV and 6.0 MeV (Compare to section 5.2.4).

capture peak at 4.78 MeV. In the ^{238}U decay chain, the following sequence can be found that would fit the energy range of the neutron capture peak.

$$^{234}\mathrm{U} \xrightarrow[2.46E5\,\mathrm{a}]{4775\,\mathrm{keV}} {}^{230}\mathrm{Th} \xrightarrow[7.54E4\,\mathrm{a}]{4687\,\mathrm{keV}} {}^{226}\mathrm{Ra} \xrightarrow[1600\,\mathrm{a}]{4784\,\mathrm{keV}} {}^{222}\mathrm{Rn} \xrightarrow[3.82\,\mathrm{d}]{5490\,\mathrm{keV}} {}^{218}\mathrm{Po}$$

Because of the low counting for the primordial elements ^{232}Th, ^{235}U, and ^{238}U, a further statement on the alpha rate for daughter nuclei is not possible. It cannot be assumed that the secular equilibrium of the natural decay chains is not broken. As secular equilibrium describes a constant quantity of a radioactive isotope because its production rate is equal to its decay rate. This can only happen if the half-life of the daughter nuclei is much shorter than the half-life of the parent nuclei. The activity is, therefore, constant for all nuclei in the decay chain [166].
An additional peak at 5.3 MeV is observed, corresponding to a ^{210}Po surface contamination with in total $23.5 \pm 2.94 \cdot 10^{-1}$ counts/keV/kg/day. The decay of ^{210}Po is given by the following equation:

$$^{210}\mathrm{Po} \rightarrow {}^{206}\mathrm{Pb}(103\,\mathrm{keV}) + \alpha(5.3\,\mathrm{MeV})$$

If the decay occurs sufficiently close to surfaces, the full alpha particle energy of 5.3 MeV is detected, whereas the daughter nuclide can escape the crystal. In total an activity of $2.70 \pm 0.34 \cdot 10^{-1}$ mBq/kg is found. The contamination can also originate from surface contamination of the surrounding material.

Bronze clamps, similar to the holding of CRESST-II detectors, hold the crystal. Also there a contamination with ^{210}Po was observed [153].
Those calculations are upper limits. An event not in coincidence with the muon veto does not imply to be an alpha event and not a neutron capture event but can also not be excluded.

A.2 Neutron Spectrum in the Experimental Volume in the UGL

Similar to section 7.1, a neutron spectrum is calculated for all events in the alpha tritium band. Figure A.3 shows on the top in grey the measured

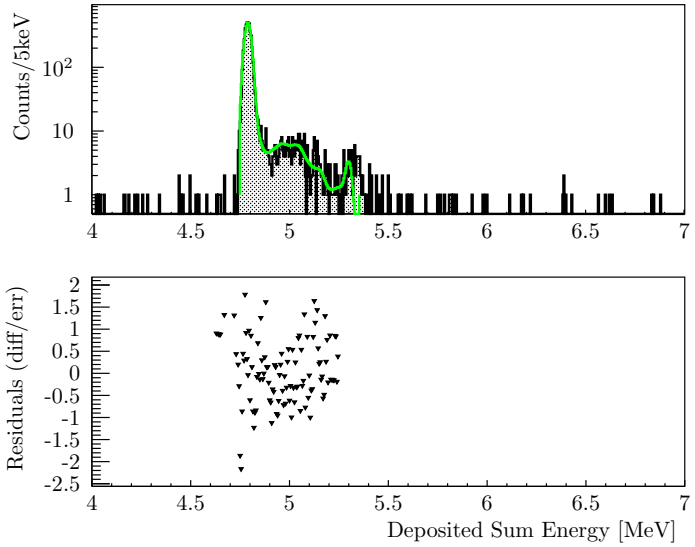

Figure A.3: *Top:* Measured energy spectrum (black/grey) after muon veto coincidence cut with the long window (see figure 7.3). The result of the fit with the simulated spectra is shown in green. The selected energy range for the fit is chosen between 4.75 MeV and 5.35 MeV. *Bottom:* Residuals (difference of measured data to fit weighted by the error). The fit is searching for a minimum of the absolute sum of residuals.

spectrum with the fitted spectrum from the unfolding method 2 in green in the energy range between 4 MeV and 7 MeV. The fit is applied for the energy range between 4.75 MeV and 5.35 MeV. The energy range is selected from the thermal/epithermal neutron capture peak up to the alpha energy of ^{210}Po. The measurement statistic is low outside the selected range, and only a few counts are measured. The residuals (difference fit measured data weighted by the statistical error) are shown at the bottom. Again the best fit is chosen, and statistical errors are included. The distribution of the residuals

is shown in figure A.4. Also, here a gaussian shape around zero is observed. With the best-fit result presented in figure A.3, the initial neutron energy

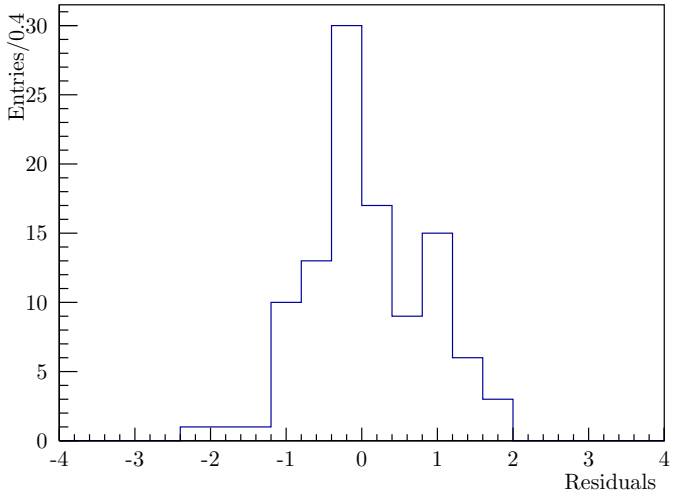

Figure A.4: Histogram of the residuals from the fitted spectrum to the data (see figure A.3). The shape is Gaussian-like around zero, indicating that the fit applied can well describe the spectrum.

for muon-induced neutrons is calculated according to equation 6.8 in section 6.2.3. Figure A.5 presents the neutron flux versus the initial neutron spectrum of the measured data for all events in the capture band (black) and muon-induced events (red). The energy is binned in 20 keV steps between 0 keV and 500 keV. Since for thermal neutrons, single energy of 0.025 eV was simulated to resolve the thermal neutron peak, which is the dominant component of the spectrum. The result represents the best-fit values with statistical errors included. The marker is placed in the center of the energy bin. Compared to spectrum 7.10, the energy region above 50 keV of initial neutron energy is very similar. Below that value, a rise in the neutron flux is observed. The calculated flux in the lowest energy bin gives a value of $(17.1 \pm 0.4) \cdot 10^{-1}\,\mathrm{cm}^{-1}\mathrm{h}^{-1}(20\,\mathrm{keV})^{-1}$ and is, therefore, 150 % higher than for muon-induced events only. A total neutron flux $(5.6 \pm 0.9)\,\mathrm{cm}^{-1}\mathrm{h}^{-1}(20\,\mathrm{keV})^{-1}$ up to 500 keV is found.

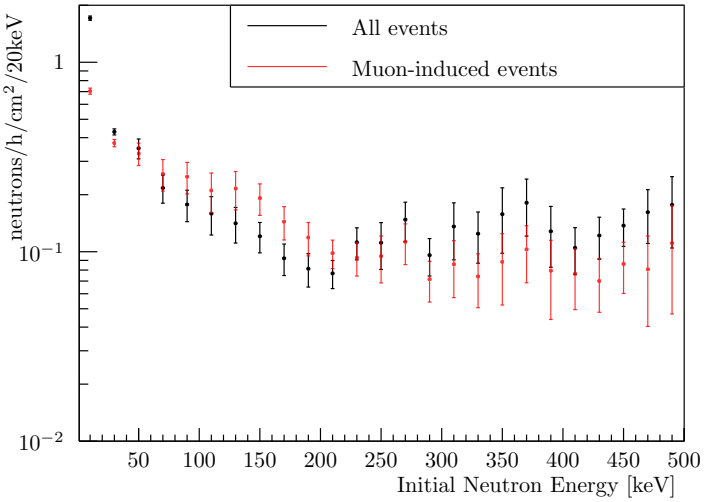

Figure A.5: Neutron flux versus initial neutron spectrum of the measured data for muon-induced neutrons (red) and all neutron events (black). The energy is binned in 20 keV steps between 0 MeV and 500 keV. The result represents the best-fit values and includes statistical errors. The marker is placed in the center of the energy bin. The calculated flux in the lowest energy bin is found to bef $(17.1 \pm 0.4) \cdot 10^{-1}\,\mathrm{cm}^{-1}\mathrm{h}^{-1}(20\,\mathrm{keV})^{-1}$ and is, therefore, 150 % higher than for muon-induced events only. A total neutron flux $(5.6 \pm 0.9)\,\mathrm{cm}^{-1}\mathrm{h}^{-1}(20\,\mathrm{keV})^{-1}$ up to 500 keV is found.

Appendix B

Decay Chains of ^{232}Th, ^{235}U and ^{238}U

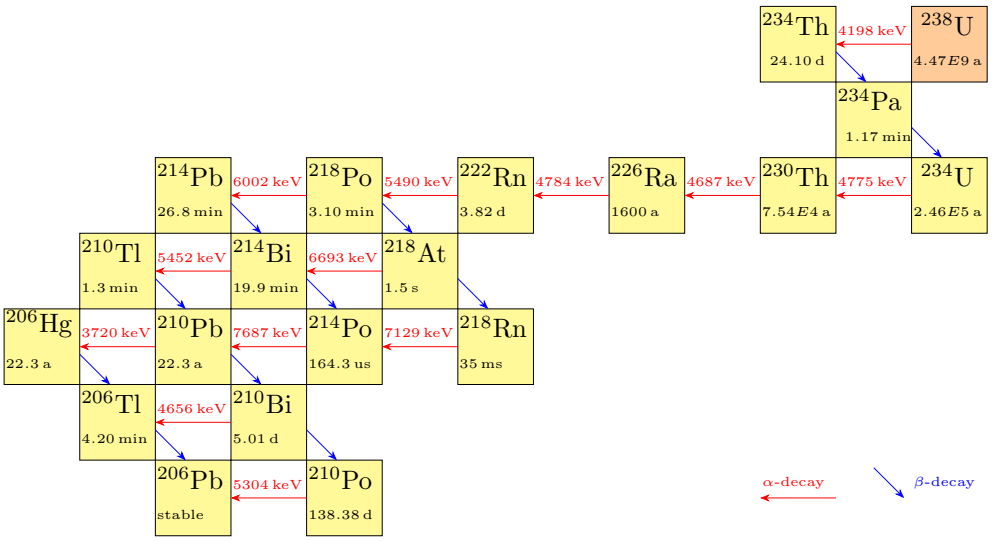

Figure B.1: Decay chain of the mother nuclide ^{238}U (uranium series). Data taken from [167][168].

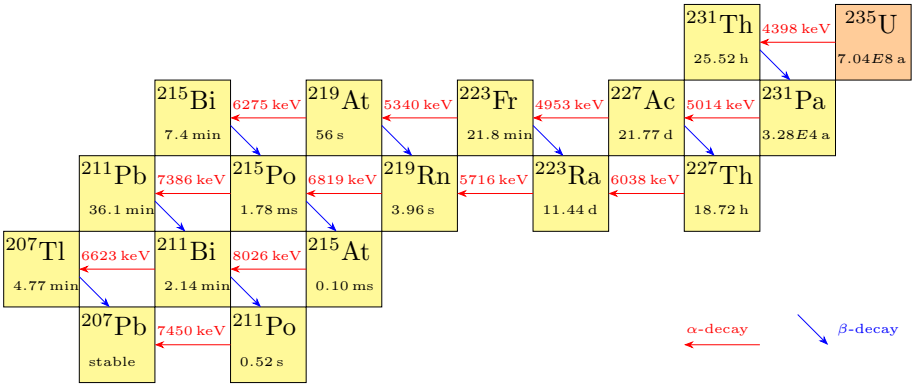

Figure B.2: Decay chain of the mother nuclide ^{235}U (actinium series). Data taken from [167][168].

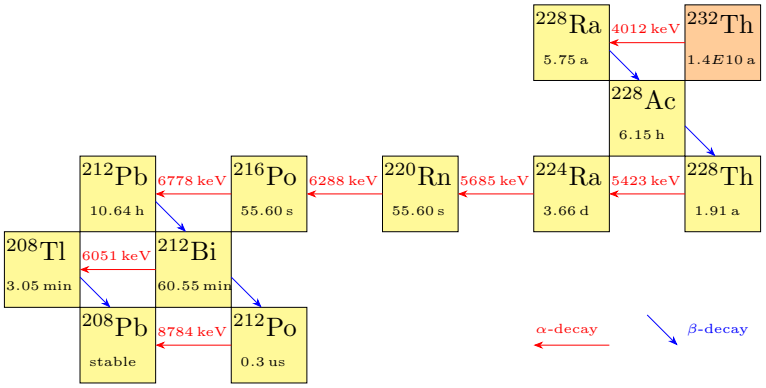

Figure B.3: Decay chain of the mother nuclide ^{232}Th (thorium series). Data taken from [167][168].

Bibliography

[1] W. Kelvin, *Baltimore Lectures on Molecular Dynamics and the Wave Theory of Light*, Cambridge University Press (1904)

[2] H. Poincaré, *The milky way and the theory of gases*, Popular Astronomy **14**, 475 (1906)

[3] H. Poincaré, et al., *Leçons sur les hypothèses cosmogoniques: professées à la Sorbonne* (1911)

[4] J. H. Oort, *The force exerted by the stellar system in the direction perpendicular to the galactic plane and some related problems*, Bulletin of the Astronomical Institutes of the Netherlands **6**, 248 (1932)

[5] J. H. Jeans, *The Motions of Stars in a Kapteyn- Universe*, Mon. Not. R. Astron. Soc. **82**, 122 (1922)

[6] Lindblad, Uppsala Meddelanden **11**, 30 (1926)

[7] E. Öpik, *Selective absorption of light in space, and the dynamics of the Universe*, Bull. de la Soc. Astr. de Russie **21**, 150 (1915)

[8] F. Zwicky, *Die Rotverschiebung von extragalaktischen Nebeln*, Helvetica Physica Acta (1933)

[9] G. Bertone, et al., *History of dark matter*, Reviews of Moderne Physics **90**, 045002 (2018)

[10] P. D. Group, *Review of Particle Physics*, Chin. Phys. C **38** (2014)

[11] E. Corbelli, et al., *The Extended Rotation Curve and the Dark Matter Halo of M33*, Mon. Not. R. Astron. Soc. (1999)

[12] R. Sancisi, et al., *Dark Matter*, in A. Hewitt, et al. (editors), *Observational Cosmology*, volume 124, 699 (1987)

[13] K. Begeman, et al., *Extended rotation curves of spiral galaxies - Dark haloes and modified dynamics*, Mon. Not. R. astr. Soc. (1991)

[14] V. C. Rubin, et al., *Extended rotation curves of high-luminosity spiral galaxies*, Astrophys. J. **225** (1978)

[15] G. W. Angus, et al., *X-ray Group and cluster mass profiles in MOND: Unexplained mass on the group scale*, Mon. Not. R. Astron. Soc. (2007)

[16] D. Clowe, et al., *Weak lensing mass reconstruction of the interacting cluster 1E0657-588: Direct evidence for the existence of dark matter*, Astrophys. J. **604**, pp. 596 (2004)

[17] D. Clowe, et al., *A Direct Empirical Proof of the Existence of Dark Matter*, Astrophys. J. **648** (2006)

[18] E. Gawiser, et al., *The Cosmic Microwave Background Radiation*, Phys. Rep. **333**, pp. 245 (2000)

[19] P. Ade, et al., *Planck 2013 results. XVI. Cosmological parameters*, Astronomy & Astrophysics **571** (2014)

[20] A. N., et al., *Planck 2018 results - I. Overview and the cosmological legacy of Planck*, Astronomy & Astrophysics (2020)

[21] J. L. Feng, *Dark Matter Candidates from Particle Physics and Methods of Detection* (2010)

[22] L. Bergström, *Dark matter candidates* (2009)

[23] M. Aker, et al., *Direct neutrino-mass measurement with sub-electronvolt sensitivity*, Nature Physics **18**, 160 (2022)

[24] S. Hannestad, *Neutrinos in cosmology*, New J. Phys. **6**, pp. 108 (2004)

[25] R. D. Peccei, et al., CP *Conservation in the Presence of Pseudoparticles*, Phys. Rev. Lett. **38**, 1440 (1977)

[26] A. Browman, et al., *Decay Width of the Neutral π Meson*, Phys. Rev. Lett. **33**, 1400 (1974)

[27] G. G. Raffelt, *Astrophysical Axion Bounds*, 51–71, Springer Berlin Heidelberg, Berlin, Heidelberg (2008)

[28] B. W. Lee, et al., *Cosmological Lower Bound on Heavy-Neutrino Masses*, Phys. Rev. Lett. **39**, pp. 165 (1977)

[29] K. Petraki, et al., *Review of asymmetric dark matter*, Int. J. Mod. Phys. A **28** (2013)

[30] K. M. Zurek, *Asymmetric Dark Matter: Theories, Signatures, and Constraints*, Phys. Rev. Lett. (2013)

[31] ATLAS Collaboration, *Search for dark matter in events with heavy quarks and missing transverse momentum in pp collisions with the ATLAS detector*, Eur. Phys. J. C (2015)

[32] CMS Collaboration, *Search for dark matter, extra dimensions, and unparticles in monojet events in proton-proton collisions at sqrt(s) = 8 TeV*, Eur. Phys. J. C (2015)

[33] M. Klasen, et al., *Indirect and direct search for dark matter*, Progress in Particle and Nuclear Physics **85**, 1 (2015)

[34] O. Adriani, et al., *The PAMELA Mission: Heralding a new era in precision cosmic ray physics*, Phys. Rep. **544**, pp. 323 (2014)

[35] M. R. Buckley, et al., *Search for Gamma-ray Emission from Dark Matter Annihilation in the Large Magellanic Cloud with the Fermi Large Area Telescope*, Phys. Rev. D **91** (2015)

[36] E. Armengaud, et al., *Search for low-mass WIMPs with EDELWEISS-II heat-and-ionization detectors*, Phys. Rev. D **86** (2012)

[37] R. Agnese, et al., *Search for Low-Mass Weakly Interacting Massive Particles with SuperCDMS*, Phys. Rev. Lett. **112** (2014)

[38] R. Agnese, et al., *WIMP-Search Results from the Second CDMSlite Run*, Phys. Rev. Lett. (2015)

[39] R. Agnese, et al., *Search for Low-Mass Weakly Interacting Massive Particles Using Voltage-Assisted Calorimetric Ionization Detection in the SuperCDMS Experiment*, Phys. Rev. Lett. **112** (2014)

[40] R. Agnese, et al., SuperCDMS Collaboration, *Search for low-mass dark matter with CDMSlite using a profile likelihood fit*, Phys. Rev. D **99**, 062001 (2019)

[41] SuperCDMS Collaboration, et al., *A Strategy for Low-Mass Dark Matter Searches with Cryogenic Detectors in the SuperCDMS SNOLAB Facility* (2022)

[42] D. Akerib, et al., *The Large Underground Xenon (LUX) experiment*, Nuclear Instruments and Methods in Physics Research, Section A: Accelerators, Spectrometers, Detectors and Associated Equipment **704**, 111 (2013)

[43] E. Aprile, et al., *Dark Matter Results from 225 Live Days of XENON100 Data*, Phys. Rev. Lett. **109** (2012)

[44] E. Aprile, et al., *Physics reach of the XENON1T dark matter experiment.*, Journal of Cosmology and Astroparticle Physics **2016**, 027, URL https://doi.org/10.1088/1475-7516/2016/04/027 (2016)

[45] H. Zhang, et al., *Dark matter direct search sensitivity of the PandaX-4T experiment*, Science China Physics, Mechanics & Astronomy **62**, 31011 (2018)

[46] S. Cebrian, et al., *First results of the ROSEBUD dark matter experiment*, Astropart. Phys. **15**, 79 (2001)

[47] G. Angloher, et al., *A CsI low-temperature detector for dark matter search*, Astroparticle Physics **84**, 70 (2016)

[48] A. H. Abdelhameed, et al., CRESST Collaboration, *First results from the CRESST-III low-mass dark matter program*, Phys. Rev. D **100**, 102002 (2019)

[49] G. Angloher, et al., *Probing low WIMP masses with the next generation of CRESST detectors* (2015)

[50] G. Angloher, et al., *Results on MeV-scale dark matter from a gram-scale cryogenic calorimeter operated above ground*, Eur. Phys. J. C **77** (2017)

[51] H. Jiang, et al., CDEX Collaboration, *Limits on Light Weakly Interacting Massive Particles from the First* 102.8 $kg \times day$ *Data of the CDEX-10 Experiment*, Phys. Rev. Lett. **120**, 241301, URL https://link.aps.org/doi/10.1103/PhysRevLett.120.241301 (2018)

[52] A. Aguilar-Arevalo, et al., *Results on Low-Mass Weakly Interacting Massive Particles from an 11 kg-day Target Exposure of DAMIC at SNOLAB*, Phys. Rev. Lett. **125**, 241803 (2020)

[53] L. Hehn, et al., *Improved EDELWEISS-III sensitivity for low-mass WIMPs using a profile likelihood approach*, Eur. Phys. J. C **76**, 548, URL https://doi.org/10.1140/epjc/s10052-016-4388-y (2016)

[54] E. Armengaud, et al., *Searching for low-mass dark matter particles with a massive Ge bolometer operated above-ground*, Phys. Rev. D **99**, 082003, URL http://arxiv.org/abs/1901.03588 (2019), arXiv: 1901.03588

[55] SuperCDMS Collaboration, et al., *Light Dark Matter Search with a High-Resolution Athermal Phonon Detector Operated above Ground*, Phys. Rev. Lett. **127**, 061801, URL https://link.aps.org/doi/10.1103/PhysRevLett.127.061801 (2021), publisher: American Physical Society

[56] R. Ajaj, et al., DEAP Collaboration, *Search for dark matter with a 231-day exposure of liquid argon using DEAP-3600 at SNOLAB*, Phys. Rev. D **100**, 022004, URL https://link.aps.org/doi/10.1103/PhysRevD.100.022004 (2019), publisher: American Physical Society

[57] C. E. CoGeNT Collaboration, Aalseth, et al., Phys. Rev. D (2013)

[58] P. Agnes, et al., DarkSide Collaboration, *Low-Mass Dark Matter Search with the DarkSide-50 Experiment*, Phys. Rev. Lett. **121**, 081307, URL https://link.aps.org/doi/10.1103/PhysRevLett.121.081307 (2018)

[59] D. Akerib, et al., LUX Collaboration, *Results from a Search for Dark Matter in the Complete LUX Exposure*, Phys. Rev. Lett. **118**, 021303, URL http://link.aps.org/doi/10.1103/PhysRevLett.118.021303 (2017)

[60] X. Cui, et al., PandaX-II Collaboration, *Dark Matter Results from 54-Ton-Day Exposure of PandaX-II Experiment*, Phys. Rev. Lett. **119**, 181302, URL https://link.aps.org/doi/10.1103/PhysRevLett.119.181302 (2017)

[61] E. Aprile, et al., XENON Collaboration, *Dark Matter Search Results from a One Ton-Year Exposure of XENON1T*, Phys. Rev. Lett. **121**, 111302, URL https://link.aps.org/doi/10.1103/PhysRevLett.121.111302 (2018)

[62] E. Aprile, et al., Xenon Collaboration, *Light Dark Matter Search with Ionization Signals in XENON1T*, arXiv:1907.11485 [astro-ph, physics:hep-ex] URL http://arxiv.org/abs/1907.11485 (2019), arXiv: 1907.11485

[63] G. Adhikari, et al., *Strong constraints from COSINE-100 on the DAMA dark matter results using the same sodium iodide target*, Sci. Adv. **7**, eabk2699, URL https://www.science.org/doi/10.1126/sciadv.abk2699 (2020), publisher: American Association for the Advancement of Science

[64] J. Collar, *Search for a nonrelativistic component in the spectrum of cosmic rays at Earth*, Phys. Rev. D **98**, 023005, URL https://link.aps.org/doi/10.1103/PhysRevD.98.023005 (2018)

[65] Q. Arnaud, et al., *First results from the NEWS-G direct dark matter search experiment at the LSM*, Astropart. Phys. **97**, 54, URL http://www.sciencedirect.com/science/article/pii/S0927650517301871 (2018)

[66] K. Abe, et al., *A direct dark matter search in XMASS-I*, Physics Letters B **789**, 45, URL https://www.sciencedirect.com/science/article/pii/S0370269318309262 (2019)

[67] C. Amole, et al., PICO Collaboration, *Dark matter search results from the complete exposure of the PICO-60* C_3F_8 *bubble chamber*, Phys. Rev. D **100**, 022001, URL https://link.aps.org/doi/10.1103/PhysRevD.100.022001 (2019), publisher: American Physical Society

[68] A. Gütlein, et al., *Impact of Coherent Neutrino Nucleus Scattering on Direct Dark Matter Searches based on* $CaWO_4$ *Crystals*, Astropart. Phys. **69**, 44, URL http://arxiv.org/abs/1408.2357 (2015)

[69] F. Reindl, *Private communication* (2022)

[70] G. Angloher, et al., *Commissioning run of the CRESST-II dark matter search*, Astropart. Phys. **31**, pp. 270 (2009)

[71] *Homepage of the CRESST experiment*, URL http://www.cresst.de (accessed November 23, 2021)

[72] *Homepage of the Grand Sasso National Laboratory*, URL www.lngs.infn.it (accessed January 14, 2022)

[73] M. Haffke, et al., *Background measurements in the Gran Sasso Underground Laboratory*, Nucl. Instr. Meth. Phys. Res. A **643**, pp. 36 (2011)

[74] F. Bellini, et al., *Monte Carlo evaluation of the external gamma, neutron and muon induced background sources in the CUORE experiment*, Astroparticle Physics **33**, 169, URL https://www.sciencedirect.com/science/article/pii/S092765051000023X (2010)

[75] G. Bellini, et al., *Cosmic-muon flux and annual modulation in Borexino at 3800 m water-equivalent depth*, Journal of Cosmology and Astroparticle Physics **2012**, 015, URL https://doi.org/10.1088/1475-7516/2012/05/015 (2012)

[76] M. Ambrosio, et al., *Vertical muon intensity measured with MACRO at the Gran Sasso laboratory*, Phys. Rev. D **52**, 3793, URL https://link.aps.org/doi/10.1103/PhysRevD.52.3793 (1995)

[77] R. Lang, *Search for Dark Matter with the CRESST Experiment*, Ph.D. thesis, Technische Universität Münchem (2008)

[78] G. Angloher, et al., *Results from 730 kg days of the CRESST-II Dark Matter search*, Eur. Phys. J. C (2012)

[79] G. Angloher, et al., *Results on low mass WIMPs using an upgraded CRESST-II detector*, Eur. Phys. J. C (2014)

[80] A. Münster, et al., *Radiopurity of $CaWO_4$ crystals for direct dark matter search with CRESST and EURECA*, Journal of Cosmology and Astroparticle Physics **2014**, 018 (2014)

[81] A. Erb, et al., *Growth of high-purity scintillating $CaWO_4$ single crystals for the low-temperature direct dark matter search experiment CRESST-II and EURECA*, CrystEngComm **15**, pp. 2301 (2013)

[82] G. Angloher, et al., *Results on light dark matter particles with a low-threshold CRESST-II detector* (2016)

[83] *Homepage of 3M Deutschland*, URL `http://www.3mdeutschland.de` (accessed February 21, 2016)

[84] M. Kiefer, *Improving the Light Channel of the CRESST-II Dark Matter Detectors*, Ph.D. thesis, Technische Universität München (2012)

[85] S. B. Roth, *The Potential of Neganov-Luke Amplified Cryogenic Light Detectors and the Scintillation-Light Quenching Mechanism in CaWO 4 Single Crystals in the Context of the Dark Matter Search Experiment CRESST-II*, Ph.D. thesis, Technische Universität München (2013)

[86] R. Strauß, *Energy-Dependent Quenching Factor Measurements of CaWO 4 Crystals at mK Temperatures and Detector Prototypes for Direct Dark Matter Search with CRESST*, Ph.D. thesis, Technische Universität München (2013)

[87] R. Strauss, et al., *Energy-dependet light quenching in $CaWO_4$ crystals at mK temperatures*, European Physical Journal C **74** (2014)

[88] P. Adari, et al., *EXCESS workshop: Descriptions of rising low-energy spectra*, URL `https://arxiv.org/abs/2202.05097` (2022)

[89] P. Bauer, *Data Analysis for the CRESST Experiment: New Methods, improved Alpha Analysis, and Results on Light Dark Matter and Backgrounds*, Ph.D. thesis, Technische Universität München (2020)

[90] M. Stahlberg, *Probing Low-Mass Dark Matter with CRESST-III - Data Analysis and First Results*, Ph.D. thesis, Technische Universität Wien (2020)

[91] M. Bowles, *Minimizing Backgrounds for the SuperCDMS SNOLAB Dark-Matter Experiment*, Ph.D. thesis, South Dakota School of Mines and Technology Rapid City (2019)

[92] G. Heusser, *Low-Radioactivity Background Techniques* **45**, 543, URL `https://doi.org/10.1146/annurev.ns.45.120195.002551` (1995)

[93] G. Angloher, et al., *Exploring CEvNS with NUCLEUS at the Chooz Nuclear Power Plant* (2019)

[94] A. Langenkämper, et al., *A Cryogenic Detector Characterization Facility in the Shallow Underground Laboratory at the Technical University of Munich*, Journal of Low Temperature Physics **193** (2018)

[95] R. Strauss, et al., *A prototype detector for the CRESST-III low-mass dark matter search* (2016)

[96] R. Burkhardt, *Abschätzung der Abschirmwirkung des Garchinger Untergrundlabors (UGL) durch die Messung des Myonen-Flusses inner- und ausserhalb des UGLs*, Bachelor's thesis, Technische Universität München (2012)

[97] J. C. Lanfranchi, *Development of a New Composite Cryogenic Detection Concept for a Radiochemical Solar Neutrino Experiment*, Ph.D. thesis, Technische Universität München (2005)

[98] M. Agostini, et al., *Upgrade for Phase II of the Gerda experiment*, The European Physical Journal C **78**, 388, URL `https://doi.org/10.1140/epjc/s10052-018-5812-2` (2018)

[99] N. Abgrall, et al., *LEGEND-1000 Preconceptual Design Report*, Physics - Instrumentation and Detectors, Nuclear Experiment (2021)

[100] T. Adam, et al., *JUNO Conceptual Design Report* URL `https://arxiv.org/abs/1508.07166` (2015)

[101] A. R. Münster, *High-Purity $CaWO_4$ Single Crystals for Direct Dark Matter Search with the CRESST Experiment*, Ph.D. thesis, Technische Universität München (2017)

[102] A. Kinast, *PhD thesis in preparation*, Ph.D. thesis, Technische Universität München

[103] L. H., *Proceedings at International Conference on Low Temperature Physics* 157 (1951)

[104] P. Das, et al., *A Realization of a London-Clarke-Mendoza Type Refrigerator*, in *Low Temperature Physics LT9*, 1253–1255, Springer US, Boston, MA (1965)

[105] D. Cousins, et al., *An advanced dilution refrigerator designed for the new lancaster microkelvin facility.*, Journal of Low Temperature Physics **114**, 547 (1999)

[106] H. Abe, et al., *Visual observation of the bubble dynamics in normal ^{4}He, superfluid ^{4}He and superfluid ^{3}He/^{4}He mixtures*, Journal of Fluid Mechanics **619**, 261 (2009)

[107] C. Enss, et al., *Low-Temperature Physics*, Springer Berlin Heidelberg (2005)

[108] J. Wilks, et al., *The Properties of Liquid and Solid Helium*, Physics Today **21**, 72 (1967)

[109] L. Klinkenberg, *Commissioning of an Active Muon-Veto to Study Muon-Induced Background at Sub-keV Energies*, Masters thesis, Technische Universität München (2021)

[110] C. Isaila, *Development of Cryogenic Light Detectors with Neganov-Luke Amplification for the Dark Matter Experiments CRESST and EURECA*, Ph.D. thesis, Technische Universität München (2010)

[111] e. a. X. Defay, *Cryogenic Silicon Detectors with Implanted Contacts for the Detection of Visible Photons Using the Neganov-Trofimov-Luke Effect*, Journal of Low Temperature Physics **183** (2016)

[112] *Homepage of Pfeiffer Vacuum*, URL `https://www.pfeiffer-vacuum.com/` (accessed April 05, 2022)

[113] *Homepage of hyco Vakuumtechnik GmbH*, URL `https://www.hyco.de/` (accessed April 05, 2022)

[114] *Homepage of GVL Cryoengineering GmbH*, URL `http://www.gvl-cryoengineering.de` (accessed April 13, 2022)

[115] *Homepage of Magnicon GMBH ; SQUID supplier*, URL `http://www.magnicon.com/` (accessed April 08, 2022)

[116] C. Kittel, *Introduction to Solid State Physics*, volume 7, Wiley, New York (1996)

[117] *Homepage of Lakeshore cryotronics*, URL `https://www.lakeshore.com` (accessed March 12, 2022)

[118] *Homepage of Bluefors*, URL `https://www.bluefors.com/` (accessed April 07, 2022)

[119] T. Lachenmaier, *Messungen mit untergrundarmen Tieftemperaturdetektoren zum hocheffizienten Nachweis des ^{71}Ge-Zerfalls*, Ph.D. thesis, Technische Universität München (2005)

[120] M. Willers, *Background Suppression in TeO_2 Bolometers with Neganov-Luke Amplified Cryogenic Light Detectors*, Ph.D. thesis, Technische Universität München (2015)

[121] *Homepage of Struck Innovative Systeme GmbH*, URL `https://www.struck.de` (accessed June 20, 2022)

[122] M. Schwarz, *PhD thesis in preparation*, Ph.D. thesis, Technische Universität München

[123] F. Pröbst, et al., *Model for cryogenic particle detectors with superconducting phase transition thermometers*, Journal of Low Temperature Physics **100**, 69 (1995)

[124] C. V. Briscoe, et al., *Elastic Constants of LiF from 4.2°K to 300°K by Ultrasonic Methods*, Phys. Rev. **106**, 1175 (1957)

[125] S. Roth, *Sputtered Tungsten Thin Films and Composite Detectors for the Application in the Dark Matter Experiments CRESST and EURECA*, Diploma thesis, Technische Universität München (2007)

[126] P. N. Peplowski, et al., *Position-dependent neutron detection efficiency loss in 3He gas proportional counters*, Nuclear Instruments and Methods in Physics Research Section A: Accelerators, Spectrometers, Detectors and Associated Equipment 164574

[127] L. N. D. Search, *Table of Radioactive Isotopes*, URL `http://nucleardata.nuclear.lu.se/toi/` (accessed February 02, 2022)

[128] H. Yanagie, et al., *Application of drug delivery system for boron neutron capture therapy Basic research toward clinical application*, Hoshasen **35**, 193 (2010)

[129] *Homepage of CIAAW*, URL `https://ciaaw.org/` (accessed April 05, 2022)

[130] M. Mancuso, *Private communication* (2021)

[131] *Homepage of Gössl und Pfaff*, URL `https://www.goessl-pfaff.de/` (accessed March 24, 2022)

[132] K. D. Irwin, *SQUIDs and Transition-Edge Sensors*, Journal of Superconductivity and Novel Magnetism **34**, 1601 (2021)

[133] *Homepage of tpt wirebonder*, URL `https://www.tpt.de` (accessed March 02, 2022)

[134] A. I. B. J. Clarke, *The SQUID Handbook Vol. I Fundamentals and Technology of SQUIDs and SQUID Systems*, WILEY VCH Verlag GmbH & Co. KGaA (2004)

[135] R. C. Jaklevic, et al., *Quantum interference effects in josephson tunneling*, Phys. Rev. Lett. **12**, pp. 159 (1964)

[136] R. e. a. Brun, *ROOT: An object oriented data analysis framework*, Nuclear Instruments and Methods in Physics Research Section A: Accelerators, Spectrometers, Detectors and Associated Equipment **A389** (1997)

[137] D. Schmiedmayer, *Calculation of Dark-Matter Exclusion-Limits using a Maximum Likelihood Approach*, Diploma thesis, Technische Universität Wien (2019)

[138] J. Bezanson, et al., *Julia: A fresh approach to numerical computing*, SIAM review **59**, 65, URL `https://doi.org/10.1137/141000671` (2017)

[139] E. Gatti, et al., *Processing the signals from solid-state detectors in elementary-particle physics*, La Rivista del Nuovo Cimento (1978-1999) **9** (1986)

[140] N. I. Ferreiro, *Increasing the sensitivity to low mass dark matter in CRESST-III with a new DAQ and signal processing*, Ph.D. thesis, Technische Universität München (2018)

[141] J. Shultis, et al., *Calculation of ion energy-deposition spectra in silicon, lithium-fluoride, boron and boron carbide* (2004)

[142] M. Safari, et al., *Differentiation method for localization of Compton edge in organic scintillation detectors* (2016)

[143] A. R. Münster, *Absolute α-Radioactivity Determination of Scintillating $CaWO_4$ Crystals for Direct Dark Matter Search*, Diploma thesis, Technische Universität München (2013)

[144] C. e. a. Arnaboldi, *$CdWO_4$ scintillating bolometer for Double Beta Decay: Light and heat anticorrelation, light yield and quenching factors*, Astroparticle Physics **34** (2010)

[145] I. Ogawa, et al., *Alpha decay of Gd150*, Nuclear Physics **66**, 119, URL `https://www.sciencedirect.com/science/article/pii/0029558265901367` (1965)

[146] M. Poneder, *Detector response of lithium aluminate to incident neutrons*, Projektarbeit, Technische Universität Wien (2019)

[147] M. Poneder, *Reconstruction of the incident neutron spectra from lithium aluminate detector measurements*, Projektarbeit, Technische Universität Wien (2019)

[148] B. Fisher, et al., *Fast neutron detection with 6Li-loaded liquid scintillator*, Nuclear Instruments and Methods in Physics Research Section A: Accelerators, Spectrometers, Detectors and Associated Equipment **646**, 126 (2011)

[149] S. Agostinelli, *Geant4 - a simulation toolkit*, Nucl. Instr. Meth. A **506** (2003)

[150] S. Scholl, *Neutron Background Simulation for the CRESST-II Experimen*, Ph.D. thesis, Technische Universität Tübingen (2011)

[151] *Homepage of NNDC*, URL `https://www.nndc.bnl.gov/nudat3/` (accessed March 24, 2022)

[152] G. Cowan, *Statistical Data Analysis*, Oxford science publications, Clarendon Press (1998)

[153] Strauss, R., et al., *A detector module with highly efficient surface-alpha event rejection operated in CRESST-II Phase 2*, Eur. Phys. J. C **75**, 352 (2015)

[154] *Homepage of NIST*, URL `https://physics.nist.gov` (accessed March 24, 2022)

[155] N. Y. Agafonova, et al., *Analysis of seasonal variations of the cosmic ray muon flux and neutrons produced by muons in the LVD detector*, Bulletin of the Russian Academy of Sciences: Physics **75**, 427, URL `https://doi.org/10.3103/S1062873811030063` (2011)

[156] P. Belli, et al., *Deep Underground Neutron Flux Measurement With Large Bf-3 Counters*, Nuovo Cim. A **101**, 959 (1989)

[157] Z. Dębicki, et al., *Thermal neutrons at Gran Sasso*, Nuclear Physics B - Proceedings Supplements **196**, 429 (2009), proceedings of the XV International Symposium on Very High Energy Cosmic Ray Interactions (ISVHECRI 2008)

[158] A. Best, et al., *Low energy neutron background in deep underground laboratories*, Nuclear Instruments and Methods in Physics Research Section A: Accelerators, Spectrometers, Detectors and Associated Equipment **812**, 1 (2016)

[159] A. Fuss, *Simulation based Neutron Background Studies for the CRESST and COSINUS Dark Matter Search Experiments*, Ph.D. thesis, Technische Universität Wien (2022)

[160] F. Arneodo, et al., *Neutron background measurements in the Hall C of the Gran Sasso Laboratory*, Nuovo Cim. A **112**, 819 (1999)

[161] R. Aleksan, et al., *Measurement of fast neutrons in the Gran Sasso laboratory using a 6Li doped liquid scintillator*, Nuclear Instruments and Methods in Physics Research Section A: Accelerators, Spectrometers, Detectors and Associated Equipment **274**, 203 (1989)

[162] C. Goupy, *Private communication* (2023)

[163] E. Bertoldo, et al., *Lithium-Containing Crystals for Light Dark Matter Search Experiments*, Journal of Low Temperature Physics **199**, 510, URL https://doi.org/10.1007/s10909-019-02287-3 (2020)

[164] K. S. Krane, *Introductory nuclear physics*, Wiley, New York, NY (1988)

[165] G. J. Feldman, et al., *A Unified Approach to the Classical Statistical Analysis of Small Signals*, Phys. Rev. D **57** (1998)

[166] *Handbook of Nuclear Chemistry*, Springer US, Boston, MA (2004)

[167] *Nuclear and Radiochemistry*, Elsevier, Oxford (2012)

[168] E. Browne, et al., *Table of radioactive isotopes* (1986)

Danksagung

Zum Abschluss möchte ich noch allen Personen danken, welche mich auf meinem langen, und manchmal nicht ganz einfachen Weg begleitet haben und ohne die diese Arbeit nicht möglich gewesen wäre.
Zunächst möchte ich mich bei meinem Doktorvater Prof. Dr. Stefan Schönert bedanken, für die Möglichkeit meine Doktorarbeit bei Ihm anzufertigen sowie für die Betreuung und dem Interesse an meiner Arbeit. Zusammen mit Prof. Dr. Lothar Oberauer trägst du massgeblich zum angenehme Arbeitsumfeld am Lehrstuhl E15 bei. Vielen Dank.
Weiter möchte ich mich bei Dr. Raimund Strauss für sein unermüdliches Engagement für meine Arbeit bedanken, sowie für die vielen Ideen und Diskussionen. Das Thema zur Untersuchung des Neutronen Hintergrundes hat erst mit dir begonnen. Ich verdanke dir sehr viel, vielen Dank für alles!
I would like to thank Dr. Michele Mancuso for his great support and friendship over the last few years, for your advice, and for always trusting in me in times when I did not. Our fruitful discussions and your help in physics significantly contributed to this work's success. You are doing a great job!
Ich bedanke mich bei Dr. Victoria Wagner und Angelina Kinast für die unglaublich schöne Zusammenarbeit in den letzten Jahren. Das UGL Team hat tolle Erfolge erzielt, die ohne euch sicherlich nicht passiert wären. Danke, dass ihr mich oft aufgebaut habt und meine Arbeit Korrektur gelesen habt. Ihr seid nicht nur gute Kollegen sondern auch sehr gute Freunde für mich.
I would like to thank Dr. Luca Pattavina for his support over the years, especially in the last months at TUM! Thanks for proofreading my thesis and for your comments.
I would like to thank Dr. Federica Petricca for your great support, especially at the end of my thesis. Thank you very much for clarifying my view of my near future! It is a pleasure for me to be part of your group.
Weiter danke ich unserem Sekretariat mit Dr. Paola Mucciarelli und Sabine Wenzel für eure stetige Unterstützung und die vielen angenehmen und offenen Gespräche.
Auch ein großer Dank geht an Norbert Gärtner für die große Unterstützung in allen elektronischen und vakuumtechnischen Belangen.
Ich bedanke mich bei meinem Mentor Dr. Michael Willers für die großartige Unterstützung, gerade in der Anfangszeit meiner Arbeit. Von dir konnte ich

sehr viel lernen. Es war eine tolle Zeit mit dir. Vielen Dank!!!!
Ich bedanke mich bei Dr. Martin Stahlberg für deine große Hilfe bei der Analyse. Oft hast du nachts noch Anpassungen in CAT für mich vorgenommen damit ich meine Analyse machen kann. Ohne dich wäre die Analyse so nicht möglich gewessen.
Weiter möchte ich mich bei der Simulationsgruppe in Wien, besonders bei Dr. Alexander Fuss, Dr. Holger Kluck und Leonie Einfalt, bedanken. Vielen Dank für eure Hilfe!
I would like to thank Margarita Kaznacheeva for her support and help with the timing parameter.
Ich möchte mich bei unserer Werkstatt bedanken für die Umsetzung aller, manchmal auch wirren, Ideen. Ihr macht einen tollen Job!
Ich bedanke mich beim gesamten E15 und all seinen Mitarbeitern und Kollegen. Es war eine wunderbare Zeit mit euch.
I would like to thank the complete MPP CRESST group. You are all amazing.
Ich möchte mich bei all meinen Freunden bedanken, besonders aber bei dir, Chris. Auch ihr musstet oft auch mich verzichten. Vielen Dank für eure Unterstützung!
Zu guter letzt möchte ich mich bei meiner Familie bedanken. Zunächst bei meinen Großeltern in München und Hamburg sowie meiner Schwiegerfamilie für euer Interesse und Zuspruch über all die Jahre. Dann bei meinen Geschwistern. Ihr habt immer an mich geglaubt und mich unterstützt wo es euch möglich war. Ich bin stolz euer großer Bruder sein zu dürfen. Und natürlich bei meinen Eltern, meiner Frau und meiner kleinen Tochter. Ihr habt mich auf diesem langen Weg stets begleitet, ohne wenn und aber. Sowohl finanziell als auch seelisch wart ihr immer für mich da wenn ich euch brauchte. Ihr habt immer an mich geglaubt und mich wieder aufgebaut. Ihr musstet viele Monate auf mich verzichten und meine "kurze Zündschnur" aushalten. Dank euch konnte ich meine Träume erfüllen. Das werde ich euch nie vergessen. Danke das ihr alle diesen Weg mit mir gegangen seid. Ihr seids der Wahnsinn.
Meiner Familie widme ich diese Arbeit!